

SAINT-PETERSBURG UNIVERSITY

Manuscript

Travkin Vladimir Stanislavovich

**FEATURES OF MESOSCALE EDDY DYNAMICS IN VARIOUS PARTS
OF THE GLOBAL OCEAN**

Scientific specialty 1.6.17. Oceanology

DISSERTATION

Dissertation is submitted for the degree of the candidate of geographical
sciences

Translation from Russian

Supervisor:

D.Sc. in Geographical Sciences,

Belonenko T.V.

Saint Petersburg

2025

TABLE OF CONTENTS

INTRODUCTION	3
CHAPTER 1. THE NORWEGIAN SEA	38
1.1. Data	38
1.2. Methods	40
1.3. Seasonal variability of mesoscale eddies of the Lofoten Basin	46
1.4. Quasi-permanent dipole of the Lofoten Basin	54
1.5 Kinetic and potential energy of mesoscale eddies of the Norwegian Sea	73
1.6 Influence of topography on the formation of the quasi-permanent Lofoten Vortex	83
CHAPTER 2. NORTHWESTERN AND SOUTH PACIFIC	102
2.1. Data	102
2.2 Methods	102
2.3 Topographic waves of the Kuril trench	103
2.4. Variability of mesoscale eddies of the South Pacific	115
CHAPTER 3. BALTIC SEA	126
3.1. Data	126
3.2. Methods	126
3.3. Seasonal and interannual variability of mesoscale eddies of the Baltic Sea	127
CONCLUSION	140
REFERENCES	145

INTRODUCTION

The relevance of the research topic and the degree of its elaboration

Mesoscale eddies are rotating nonlinear structures with horizontal dimensions exceeding the baroclinic Rossby deformation radius. They can be divided into two classes – monopole eddies and dipole structures, also called "mushroom flows" (Ginzburg and Fedorov, 1984a; 1984b). A monopole eddy consists of a eddy core rotating like a solid body and a mass of water trapped around the core, rotating in the same direction as the core (Zhmur, 2010). Dipole structures have two multidirectional regions (so-called a "cap") and a narrow elongated jet ("stem") at its base (Ginzburg and Fedorov, 1984b). Mesoscale eddies have a significant impact on the dynamics of the ocean, its hydrochemical and optical properties. Eddies are one of the main mechanisms of horizontal mixing, as well as the transport of heat, salt, energy, sea ice and biogenic substances of the Global Ocean (Monin et al., 1974; Zhmur, 2010; Mikaelyan et al., 2020; Belonenko et al., 2024). The main reason for the formation of eddies is the baroclinic and barotropic instability of currents, as a result of which areas of eddy activity are confined to areas of large-scale currents (Stammer and Wunsch, 1999; Belonenko et al., 2020b). Mesoscale eddies form everywhere in the world's oceans, simultaneously occupying about 1/3 of its area (Chelton et al., 2011a; Gaube et al., 2019). They can exist for several months or even years, while moving hundreds or thousands of kilometers, thereby reducing the contrast between the thermohaline characteristics of tropical and polar latitudes (Chelton et al., 2011a; Belonenko and Sandalyuk, 2018; Malysheva et al., 2022). The active study of mesoscale eddies began in the middle of the 20th century with the help of field observations (experiments Polygon 1967, MODE 1973, Mesopolygon 1985, etc.). The development of computing power, as well as the emergence of permanent satellite information about the sea surface at the end of the 20th century, ushered in a new era of active study of the vortex structures of the oceans (Chelton et al., 2007).

Thus, eddies in the ocean represent an inexhaustible source of information that can be obtained using satellite observations, in situ data, and model calculations. Studies of these eddies make it possible to understand many factors affecting their generation, variability, and characteristics. The analysis of the mesoscale variability of oceanological fields in different regions of the world reveals the unique features and diversity of eddy processes occurring in the ocean. These studies are important for understanding both global and regional circulation processes, as well as for assessing their impact on climate and ecological systems. In this study, three regions with completely different hydrological conditions were selected, in each of which the mesoscale eddy dynamics has a number of specific features.

The first area under consideration is the Norwegian Sea, which belongs to the oceanic marginal seas of the Arctic Ocean. It is a unique research area that has a significant impact on the climate of Europe, as it interacts between warm and salty Atlantic waters and cold and desalinated waters of the Arctic basin (Figure 1). In the north, the Norwegian Sea is bounded by Medvezhy Island and the North Cape, and in the east by the Scandinavian Peninsula. From the West and south, the sea is bounded by O. Iceland, the Faroe Islands and the Shetland Islands. The area of the Norwegian Sea is 1,340 thousand. The maximum depth exceeds 4000 m (Zalogin and Kosarev, 1999; Belonenko et al., 2021a). The deep-water part of the Norwegian Sea consists of two large basins (Zalogin and Kosarev, 1999; Akhtyamova and Travkin, 2023). The central part of the Norwegian Sea is occupied by the Norwegian Basin with depths of 2900-3500 m, and the northeastern part of the sea is occupied by the Lofoten Basin with depths of 2800-3200 m. The relief of the Norwegian basin is characterized by strong depth fluctuations and many seamounts, while the Lofoten Basin is a flat abyssal plain with the greatest depth in the central part. The basins are separated by the Helgeland Ridge and the Voring Plateau. It is worth noting that the Norwegian and Lofoten Basins are significantly limited in topographic terms.: From the west and north, the basins are bounded by the Jan Mayen and Mona ridges, and from the south and east by the Norwegian continental slope and the Voring Plateau (Belonenko et al., 2020b), which suggests that the basins are geographically

isolated and have specific features of large-scale water circulation (Ivanov and Korablev, 1995a).

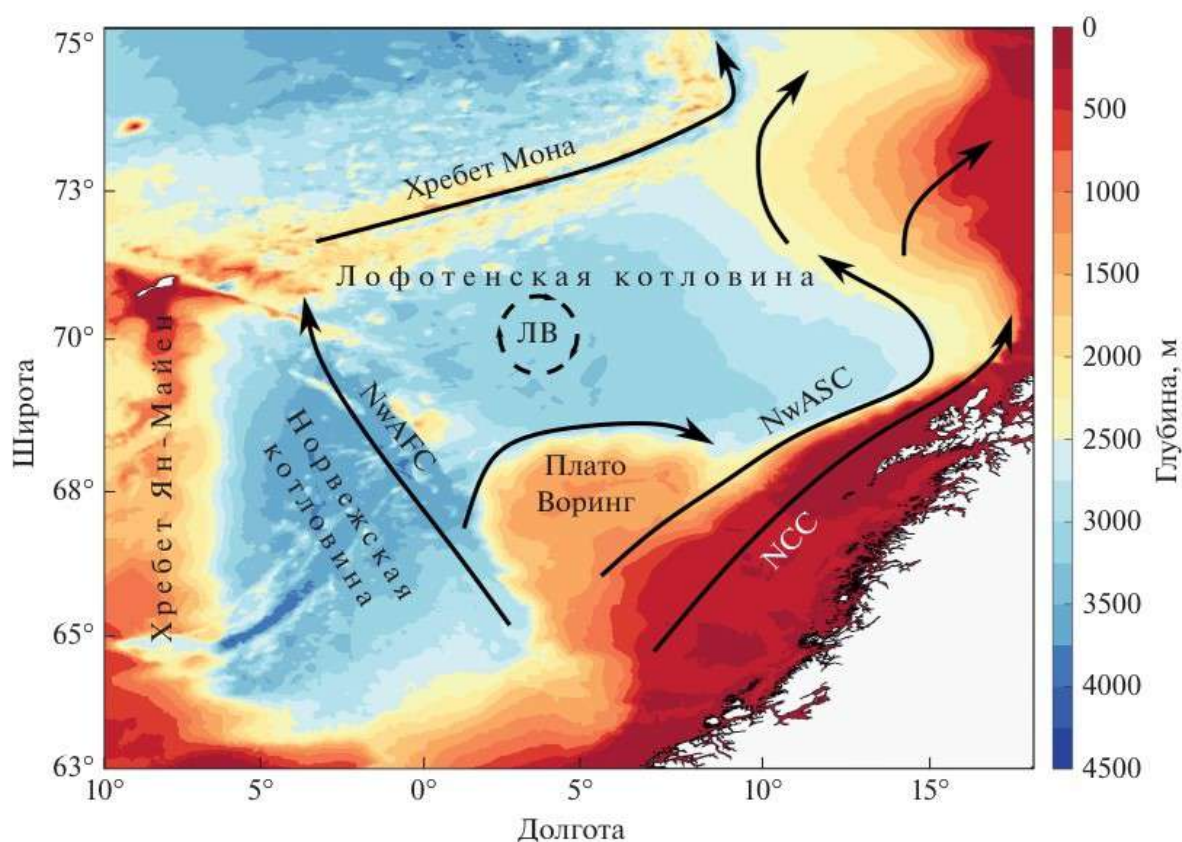


Figure. 1 Research area. The position of the anticyclonic Lofoten vortex (LV) is shown by a circle. The color shows the topography of the seabed (m), the black arrows show the branches of the Norwegian current: NwASC – Norwegian slope current, NCC – Norwegian coastal current, NwAFC – Norwegian frontal current (Travkin and Belonenko, 2020).

Atmospheric processes over the Norwegian Sea are formed under the influence of the Icelandic minimum, the Azores Maximum, and the Polar High Pressure Region (Zalogin and Kosarev, 1999). The Norwegian Sea circulation is represented by three major branches of the Norwegian Current: the Norwegian Atlantic Slope Current (NwASC), the Norwegian Atlantic Frontal Current (NwAFC), and the Norwegian Coastal Current (NCC) (Drange et al., 2005; Köhl, 2007; Belonenko et al., 2020b). The first two branches carry warm and salty Atlantic waters to the north, skirting the Lofoten Basin from the east and west, respectively

(Figure 1). The Norwegian coastal current extends northward along the Norwegian continental slope, transferring cold and desalinated waters to the Arctic Basin (Belonenko et al., 2021a).

The Norwegian Sea is characterized by the presence of three distinct water masses. The upper 100-meter layer is represented by cold and desalinated waters of Arctic origin with a salinity of less than 34.85 psu (psu – practical salinity unit) (Drange et al., 2005). Further in the layer from 100 to 250 m, a maximum salinity (more than 34.95 psu) is observed, associated with the spread of warm and salty Atlantic waters. Below these waters are cold (from -0.5°C to 0.5°C) waters of Arctic origin (Kohl, 2007). In the western part of the Norwegian Sea, due to the interaction of warm and salty Atlantic waters with cold and freshened waters of the Arctic basin, an area of elevated gradients of thermohaline characteristics is observed, called the Arctic (Polar) Front (Mork and Blindheim, 2000; Akhtyamova and Travkin, 2023).

A key feature of the Norwegian Sea is the quasi-permanent anticyclonic mesoscale Lofoten vortex (LV) located in the central part of the Lofoten Basin, which is currently a natural laboratory for studying marine mesoscale vortices (Raj et al., 2016; Fer et al., 2018; Belonenko et al., 2021a). LV is an intrapycnoclinic lens filled with warm and salty Atlantic waters (Bashmachnikov et al., 2018; Belonenko et al., 2020b). The area of the LV location is characterized by locally elevated values of sea surface height and vortex kinetic energy (Raj et al., 2016). The anticyclonic nature of the LV rotation is related to the slope of the sea surface height and near-surface isopycnae in the basin (Belonenko et al., 2017). It is known that in the area of the vortex location, isotherms shift closer to the surface is observed, as a result of which it is clearly visible in the summer and autumn period on satellite images as the "cold spot" of the Lofoten Basin (Travkin et al., 2022b). The average radius of the LV, determined by the maximum velocity of the orbital motion, varies from 20 to 50 km, which corresponds to 1.6-4.2 local values of the Rossby baroclinic deformation radius (Ivanov and Korablev, 1995a; Belonenko et al., 2014; Raj et al., 2016; Bashmachnikov et al., 2018; Fer et al., 2018). The results of field observations and model experiments demonstrate that the maximum orbital velocity is 50-80 cm/s

and is located at a distance of 17-20 km from the center of the LV, while the vertical velocity increases with increasing depth and reaches a maximum in the 500-1000 m layer (Ivanov and Korablev, 1995a, b; Søliland et al., 2016; Yu et al., 2017; Bashmachnikov et al., 2018). The dynamic LV signal can be traced from the surface to depths of more than 3000 m (Belonenko et al., 2018a; 2018c). The peak of the relative turbulence of the LV core varies from -0.2 to $-0.3 \times 10^{-4} \text{ s}^{-1}$ according to model data and up to $-0.8 \times 10^{-4} \text{ s}^{-1}$ according to field measurements (Volkov et al., 2015; Bashmachnikov et al., 2017a; Yu et al., 2017). It has been established that the LV moves within the Lofoten Basin along a quasi-cyclonic trajectory with a distance of about 130 km between the most distant points, which is several times smaller than the horizontal scales of the basin (Ivanov and Korablev, 1995b; Belonenko et al., 2014). Most of the time, the LV is located in the central part of the basin (69.8° N , 4° E), without leaving its limits. Thus, 70% of the time the LV center is located at a distance of less than one radius of the vortex from its average location, 90% of the time – at a distance of no more than 1.5-2 radii (Bashmachnikov et al., 2018). Deep winter convection is a necessary condition for the existence of LV, creating favorable conditions for its annual regeneration (Bloskhina and Ivanov, 2016). Another mechanism that makes it possible to maintain the constant existence of a vortex in the central part of the Lofoten Basin is the fusion of LV with mesoscale vortices entering the basin after separation from the Norwegian slope current (Gordeeva et al., 2021). Thus, due to the dynamic instability of the Norwegian slope current, mesoscale eddies extract heat and salt from the Norwegian current and move it to the central part of the Lofoten Basin.

As a result of winter convection, fresh surface waters enter the LV core, which are warmer and saltier than the underlying layers (Alexeev et al., 2016). Further, during the spring-summer warming, a seasonal pycnocline is formed and the LV loses contact with surface waters, acquiring a lenticular shape (Ivanov and Korablev, 1995a). The subsequent evolution of LV is determined by internal dynamics, mainly related to multidirectional vertical movements at the lens boundary (Koldunov and Belonenko, 2020). The absence of new surface water supply leads to a decrease in

horizontal density gradients at the lens boundaries in the summer and autumn period, which contributes to a reduction in the azimuthal velocity of the vortex, its vertical compression and horizontal stretching due to viscous relaxation (Shapiro, 1985; Ivanov and Korablev, 1995a). In early autumn, there is a decrease in the intake of solar radiation to the sea surface, as well as an intensification of wind action, which leads to the development of convection and the disappearance of seasonal pycnocline (Nilsen and Falck, 2006). All this leads to the establishment of a density stratification close to neutral, in which the Brunt–Väisälä frequency is negligibly low ($1.7 \times 10^{-4} \text{ s}^{-1}$), which favorably affects the renewal of vortex waters during the next winter convection, capable of reaching depths of more than 1000 m (Bloshkina and Ivanov, 2016; Fedorov et al., 2019). Reaching its greatest intensity by the end of winter, convection contributes to an increase in the horizontal gradients of thermohaline characteristics in LV and the orbital velocity of motion (Bloshkina and Ivanov, 2016).

The second area of study is the North and South Pacific. The North Pacific includes the western part of the Bering Sea, the Sea of Okhotsk, the Sea of Japan, the Yellow Sea, and the East China Sea, as well as adjacent areas of the open Pacific Ocean (Sauskan, 2006). A key feature of this region is the fact that the North Pacific is one of the most important fishing areas of the Global Ocean, which produces about 60% of the total annual Russian catch and 24% of the total output of marine industrial fisheries (FAO, 2022). This high bio–productivity is mainly due to the powerful currents of this area - the warm Kuroshio and the cold Oyashio (Sauskan, 2006).

The Kuroshio originates from a branch of the North Equatorial Current and then moves northward along the western border of the Pacific Ocean, eventually reaching the southeastern coast of Japan (Wang et al., 2022). It transports significant amounts of water, heat, and salt from tropical regions to northern latitudes, thereby smoothing the meridional gradients of thermohaline characteristics and having a significant impact on the climate and hydrological regime of the marginal seas of East Asia and the North Pacific (Nitani, 1972; Wu and Hsin, 2012; Nan et al., 2013).

The Oyashio current begins from the Bussol Strait separating the islands of Simushir and Urup and is part of the subarctic cyclonic cycle (Budyansky et al., 2024). The cold and desalinated waters of the Sea of Okhotsk, as well as the relatively warm and salty waters of the East Kamchatka Current, play a key role in the formation of the Oyasio (Prants et al., 2018). The Oyasio current system has the greatest impact on the hydrological regime of the South Kuril region. The South Kuril region is one of the most promising fishing regions of the Russian Federation (Budyansky et al., 2024). For decades, the region has been actively fishing for saury, sardines, mackerel, flounder and other marine biota (FAO, 2022).

The confluence of the Kuroshio and Oyashio waters east of Japan is the key to understanding the planet's climate change (Yasuda, 2003). Thus, in this area there is an active heat exchange between the ocean and the atmosphere, the intensity of which affects the climate of the entire planet (Deser et al., 1999). The Kuroshio-Oyashio frontal region is a wide area of confluence of two western boundary currents, in which subtropical and subarctic waters mix, resulting in the active formation of mesoscale vortices (Yasuda, 2003; Prants et al., 2018). These eddies are based on the waters of Kuroshio, Oyashio, the warm Sangara current, and the Sea of Okhotsk (Kitano, 1975). Depending on the type of water mass in the core, Kuroshio rings are usually divided into rings with warm ("warm-core rings") and cold ("cold-core rings") waters in the core, which are most common west of 155°E (Kawai, 1972; Yasuda et al., 1992). Some of these rings may exist for more than one year and reach high latitudes (Lobanov et al., 1991). Many studies have been devoted to these structures, since their periphery is an excellent place for catching pelagic fish species such as mackerel and saury (Prants et al., 2014a).

Rossby topographic waves are confined to areas with significant changes in the topography of the seabed. Such waves belong to the type of trapped waves, the energy of which is localized (captured) in areas of large-scale topography variability, and sharply decays outside them. In the world's oceans at low frequencies, these waves can manifest themselves as moving mesoscale vortices with a spatial size of several tens to the first hundreds of kilometers and with a period of several days to

several years. Currently, satellite observations, field measurements, as well as data from oceanic models and reanalysis are actively used to study them. It is known that topographic waves have a significant impact on the energy and mass transfer of the Global Ocean, upwelling and the bioproductivity of shelf areas (LeBlond and Mysak, 1981; Efimov et al., 1985). Due to the unique dynamic conditions, the South Kuril region is characterized by increased activity of mesoscale vortices (Travkin et al., 2022a). So, in this region there is a complex interaction of the cold and desalinated waters of Oyashio with the warm waters of Kuroshio. In the Kuril Ridge region, the movement of mesoscale vortices can be represented as several systems of low-frequency topographic waves. The first system consists of shelf waves and propagates along the Kuril shelf in a southwesterly direction (Efimov et al., 1985; Belonenko, 2012). In turn, the other two systems are represented by waves propagating along the slopes of the Kuril Trench, as well as along topographic inhomogeneities to the southeast of the trench. It is known that the waves of the Kuril Trench are trough waves that move in a northeasterly direction along the trough, exerting a significant influence on the formation of synoptic fluctuations and diurnal tides in the area. Using satellite information, it was found that trough waves form a stable system of mesoscale vortices moving in a northeasterly direction along the trough at a speed of about 2-6 cm/s (Bulatov and Lobanov, 1983). It is noted that these vortices are formed as a result of the dynamic effect of the atmosphere on the sea surface and have a resonant nature (Lappo, 1979; Efimov et al., 1985). According to Prants, these vortices are formed due to the barotropic and baroclinic instability of Oyasio during the cold season, when it intensifies and actively meanders (Prants, 2021). All of the above indicates that the generation of mesoscale vortices in the South Kuril region may be related to various factors.

The South Pacific is one of the most highly productive areas of the Global Ocean, playing the role of an important fishing area (Malinin and Gordeeva, 2009; Borodin et al., 2014; Travkin et al., 2024c). Thus, in the 1990s, the catch of horse mackerel in this area by all countries reached 4-4.5 million tons per year (Malinin and Gordeeva, 2009). The Peruvian jack mackerel, whose stocks have increased

recently and have been at the same level for several years, is considered one of the most promising resources for Russian fishing in open and conventional areas (Anikeyev and Gerber, 2018; Glubokov et al., 2018). At the same time, it was found that the most productive Russian fishing for Peruvian jack mackerel is carried out in the center or on the periphery of mesoscale vortices (Gordeeva and Zharova, 2016; Dubishchuk, 2021). It is known that, depending on the polarity of a mesoscale vortex, multidirectional vertical movements occur in its central part, as well as on its periphery, which significantly affect the depth of the thermo- and halocline, turbidity, and the amount of biogenic elements in the upper ocean layer (Belonenko et al., 2017; Koldunov and Belonenko, 2020). Since there is an active vertical movement of biogens in vortices, they are a favorable environment for aquatic organisms. At the same time, eddies can form at the boundary of the frontal zones, i.e. areas with strong gradients of thermohaline characteristics, in which intensive mixing of various properties of water masses occurs. Such frontal zones create favorable conditions for the formation of commercial fish aggregations, since in such areas there is a large amount of plankton, which is the main food source for many fish species (Mikaelyan et al., 2020; Mikaelyan et al., 2023). On the other hand, the topography of the seabed, which determines the location, intensity, and evolution of mesoscale eddies, has a significant impact on ocean circulation and vortex dynamics. Due to the unique dynamic conditions, areas of the Global Ocean with significant sea floor slopes are characterized by increased synoptic activity of eddies. Thus, V.N. Zyryanov was one of the first to draw attention to the fact that, as a result of the formation of topographic vortices, bioproductivity in seamount areas can exceed the surrounding background by more than an order of magnitude. This is the reason for the formation of localized clusters of commercial importance over some mountains in the open ocean (Zyryanov, 1995). As a result, the mechanisms of generation of mesoscale cyclones and anticyclones are also associated with climatic phenomena such as El Nino, which is an abnormal increase in surface water temperature in the central and eastern Pacific Ocean. The difference between the surface water temperature in El Nino regions and the colder surrounding

waters, as well as a change in its phases, can contribute to the formation of mesoscale vortex structures (Wang, 2005; Seiki et al., 2009; Yu et al., 2011). In this regard, the study of the effect of mesoscale eddies on marine ecosystems continues to be an urgent and important area of scientific research. However, the features of mesoscale eddy dynamics have not been considered in detail before.

The relief of the seabed is represented by a rather narrow (usually several tens of kilometers) strip of the continental shelf of South America, turning into a steep continental slope (Fig. 2). At the foot of the continental slope are the Peru-Chile Trench (maximum depth 8064 m, respectively). In turn, the seabed of the Pacific Ocean has a very complex relief, since large uplifts, as well as mountain ranges, divide it into a number of relatively flat areas with depths of about 3-4 km. The largest morphological province of the area is the meridionally elongated East Pacific Rise, lying west of 110° W.

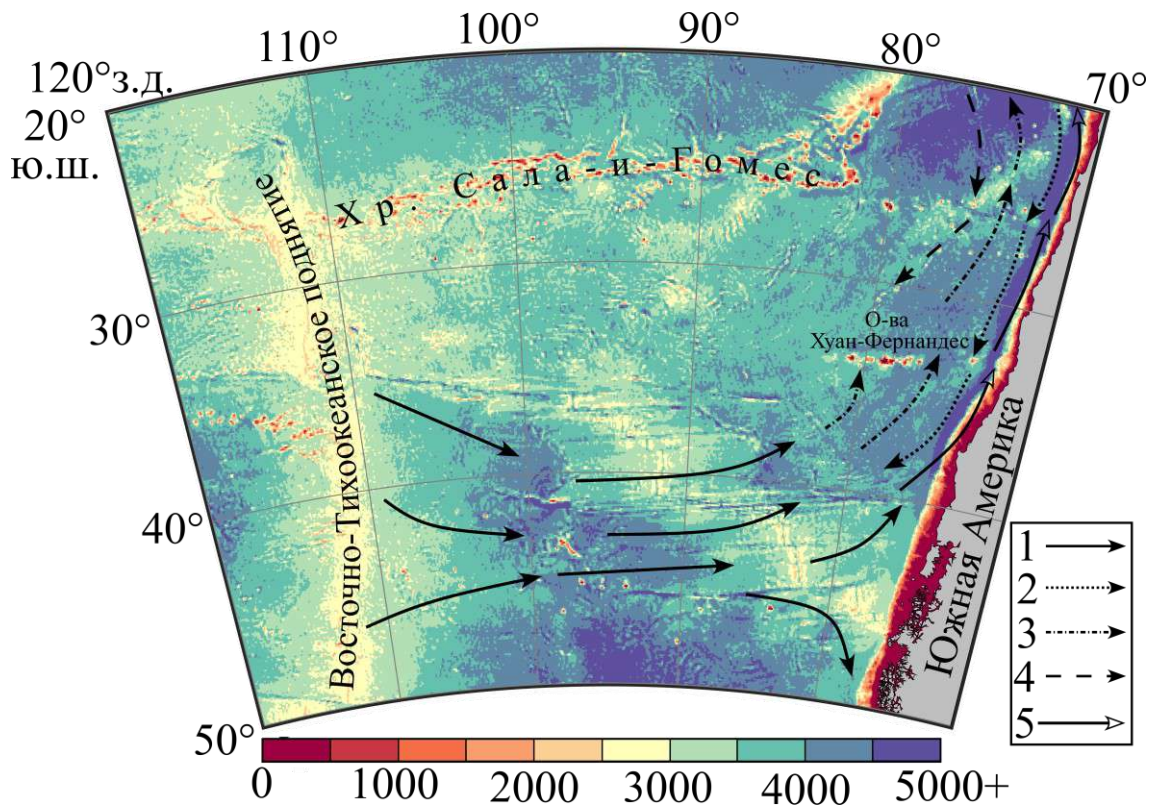


Figure. 2. Topography of the study area (m). The arrows indicate the main currents: 1 – South Pacific Current, 2 – Peru-Chilean Current, 3 – Peru Oceanic Current, 4 – Peru Counterflow, 5 – Peru Coastal Current.

The general circulation is represented by a subtropical anticyclonic gyre with a system of boundary currents, as well as a continuation of the Antarctic Circumpolar Current (ACC) (Fig. 2). Boundary currents are located in the southern, eastern, and northeastern parts of the gyre, while background water rise is observed in the eastern and southern parts of this cycle (Malinin and Gordeeva, 2009). It is known that there is a thermal frontal zone in the South – the southern subtropical front corresponding to the isotherm of 15°C and being a barrier between subtropical and subantarctic surface water masses (Fig. 3). It can be noted that the isolines of thermohaline characteristics in the study area are located zonally with increasing values in the north-westerly direction.

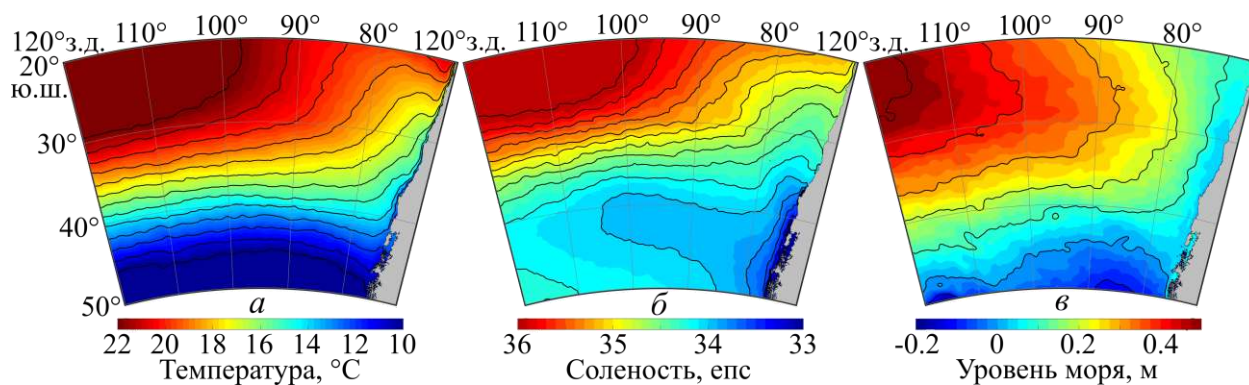


Figure 3. Average values of surface water temperature (a), salinity (b), and sea surface height (c) calculated from GLORYS12V1 data for 2010-2020.

The third area under study is the Baltic Sea, which is an intracontinental and substantially enclosed marine basin characterized by a rather complex coastline, as well as limited water exchange with the North Sea (Fig. 4). The area of the Baltic Sea is 419000 km², while the sea lies entirely within the shelf. The circulation of the Baltic Sea is significantly influenced by the direction and strength of the wind, as well as the configuration of the shores and the seabed (Zhurbas et al., 2019). The Baltic Sea is characterized by a significant rise in sea level, the growth rate of which exceeds the average estimates for the Global Ocean (Tikhonova et al., 2024). The water masses of the Baltic Sea are characterized by pronounced seasonal variability, while the water masses of different areas are not identical in their properties (Zalogin and Kosarev, 1999; Radtke et al., 2020; Lehmann et al., 2022). In most areas of the Baltic Sea, the presence of surface and deep water masses separated by a cold intermediate layer can be traced (Zalogin and Kosarev, 1999; Lehmann et al., 2022). This intermediate layer forms annually and manifests itself as a temperature minimum between the thermocline and the permanent halocline from spring to autumn (Lehmann et al., 2022). In summer and autumn, marine heatwaves are often observed in the Baltic Sea, which have a significant negative impact on the bio-productivity and condition of marine ecosystems (Travkin et al., 2024d). The baroclinic Rossby deformation radius, which is of fundamental importance for the

vortex dynamics of the Baltic Sea, varies from 1 km in coastal areas to 9 km in deep-sea areas, with maximum values recorded in summer (Kurkin et al., 2020).

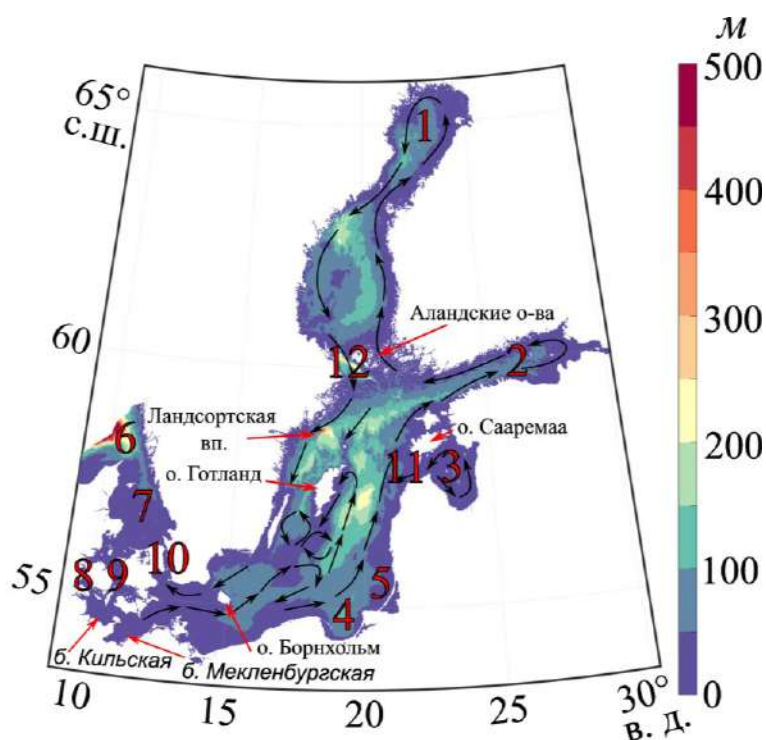


Figure. 4. Bathymetric map of the Baltic Sea. The arrows show the main currents (Zalogin and Kosarev, 1999). The numbers in the figure are: 1 – Bothnian Bay., 2 – Gulf of Finland, 3 – Gulf of Riga, 4 – Gdansk Bay, 5 – Curonian Lagoon, 6 – Skaggeerrak, 7 – Kattegat, 8-10 – Danish straits, 11 – Irbe strait, 12 – South Kvarken.

Mesoscale eddies of the Baltic Sea (often referred to as "beddies") as a rule, they are studied using field observations, radar, optical and IR images (Lass and Mohrholz, 2003; Reißmann et al., 2009; Gurova and Ivanov, 2011). The formation of mesoscale eddies in the Baltic Sea is associated with general circulation, wind action, and bottom topography (Zhurbas et al., 2019). Two widespread mechanisms of vortex formation are observed in the shelf areas of the Baltic Sea (Elkin and Zatsepin, 2013). The first mechanism is associated with barotropic and baroclinic instability of the coastal current, while barotropic instability plays a major role in the formation of shelf vortices. Another mechanism is related to the processes of

upwelling near the coast, with most vortices forming after the culmination of upwelling, when the wind begins to subside (Väli et al., 2017). Upwelling is also capable of forming a baroclinic front near the coast, contributing to baroclinic instability and active formation of mesoscale vortices (Zhurbas et al., 2019).

It is known that mesoscale eddies significantly contribute to the vertical and horizontal redistribution of salt in the Baltic Sea, and also contribute to the vertical (mainly diapycnic) mixing of constant halocline due to two mechanisms (Reißmann et al., 2009). The first mechanism is associated with the vertical displacement of isopycnals in eddies due to their rotation and geostrophic equilibrium, resulting in the rise or fall of isopycnals inside the eddy structures. Thus, in forming cyclones, vertical rising of waters from the eddy core is observed, resulting in a decrease in the mixed-layer depth, as well as seasonal and permanent pycnocline (McGillicuddy Jr, 2016). On the other hand, the opposite pattern is observed in anticyclones, which contributes to the convergence of waters on the surface in the center of the eddy (Mikaelyan et al., 2020). In lenticular vortices, rise of isopycnal is observed closer to the surface. This type of vortex is characterized by the divergence and horizontal clockwise rotation of waters on the surface (Mikaelyan et al., 2020). When a mesoscale eddy collapses, the direction of its vertical movements changes to the opposite of the original one (McGillicuddy Jr., 2016). The second mechanism is related to the destruction of mesoscale eddies. Regardless of the cause of their destruction, this contributes to active water exchange with surrounding waters, generation of internal waves, and increased vertical mixing (Reißmann et al., 2009).

It is known that eddies of the Baltic Sea can be traced at different depths, while most of them are observed in the region of constant halocline, although some are recorded throughout the water column (Reißmann et al., 2009; Lehnmann et al., 2022). For example, in the work (Lass and Mohrholz, 2003), the authors investigate cyclonic mesoscale vortices with a radius equal to the first Rossby baroclinic radius (about 6.3 km) based on field measurements. The authors note that the eddies clearly manifest themselves as lenses of salt water, spreading all the way to the bottom. Other studies indicate that the diameters of vortices in the Baltic Sea range from 10

to 20 km, with their minimum thickness being only a few meters (Reißmann et al., 2009; Lehmann et al., 2022). Such vortices are in geostrophic equilibrium, their orbital velocities are 20-30 cm/s, and the drift velocity is close to the first cm/s. At the moment, the relationship between the formation of mesoscale vortices in the Baltic Sea and saltwater outflows through the Danish Straits remains poorly understood. In addition, there is no information about time fluctuations in the intensity of mixing induced by mesoscale cyclones and anticyclones. It is noted that the proportion of volume occupied by mesoscale vortices in the four deep-water regions of the Baltic Sea (the Arkona, Bornholm, Gotland basins and the Slup Trench) is constant, and amounts to about 12% of the volume of the corresponding water areas, regardless of the type of stratification of waters in these regions (Reißmann, 2005). Seasonal variability of the total available potential energy is also recorded. Thus, in winter it is significantly higher than in summer (Reißmann, 2002).

The main goal and tasks of the study

The goal of this study is to identify the features of mesoscale eddy dynamics in the Global Ocean using satellite and model data. To achieve this goal, eddy dynamics is being studied in various parts of the Global Ocean, which makes it possible to identify not only general patterns and mechanisms, but also to identify regional features of vortex processes. The use of model data makes it possible to conduct numerical experiments that reveal the influence of local factors on the conditions of formation and characteristics of eddies. The dissertation research is aimed at a comprehensive study of mesoscale eddy dynamics using advanced methods and technologies, which will ultimately improve our understanding of oceanic processes and their role in the oceans.

To achieve this goal, the following **tasks were solved**:

1. Analysis of the influence of the seabed topography on the eddy mesoscale dynamics of the Norwegian Sea and the process of deep convection using a series of numerical experiments.

2. Analysis of seasonal and interannual variability of kinetic and available potential energy of a quasi-permanent anticyclonic Lofoten Vortex. Estimation of the barotropic and baroclinic rates of energy conversion in the Lofoten Basin.
3. Analysis of the evolution and spatial structure of the mushroom-shaped dipole of the Lofoten Basin, study of the mechanisms of its formation.
4. Assessment of the role of topography, the beta effect, the meridional gradient of the zonal flow velocity shift, and the combined effect of flow and topography on the propagation of mesoscale eddies.
5. Assessment of the spatial distribution, as well as seasonal and interannual variability of mesoscale vortex parameters in the Norwegian and Baltic Seas, as well as in the North and South Pacific.

Scientific novelty

The **scientific novelty** of the obtained results is as follows:

1. For the first time, numerical topographic experiments based on the MITgcm model have established the key role of the seabed relief in the mesoscale eddy dynamics of the Norwegian Sea; it is shown that the topographic isolation of the Lofoten Basin and the smooth nature of the seabed relief are necessary conditions for the formation of a quasi-stationary anticyclonic vortex in the center of the basin.
2. Estimates of the interannual and seasonal variability of the kinetic and potential energy of the Lofoten Vortex, as well as the rates of baroclinic and barotropic energy conversion in the Lofoten Basin, have been obtained for the first time. Estimates of kinetic and potential energy, as well as the Burger number, are given for the layer from 0 to 1000 m.
3. For the first time, using Lagrangian maps and reanalysis data, a comprehensive analysis of the dipole structures of the Lofoten Basin of the Norwegian Sea was performed; it was shown that a quasi-permanent mushroom-shaped dipole is located in the eastern part of the Lofoten Basin, which manifests itself in an averaged velocity field. The poorly studied features of the evolution, as well as the horizontal and vertical structures of dipole vortices are considered.

4. For the first time, the trajectories and basic parameters of mesoscale vortices in the Kuril region are considered in detail. It is shown that mesoscale eddies form four systems of topographic waves, with the number of cyclones twice as high as the number of anticyclones. Estimates of the components of the effective beta effect are given; it is established that the contribution of the topographic component to the propagation of vortices as topographic waves exceeds the contribution of other factors.

5. Based on the Mesoscale Eddy Trajectories Atlas and reanalysis data, estimates of the seasonal and spatial variability of the parameters of mesoscale cyclones and anticyclones of the Norwegian and Baltic Seas, as well as the South Pacific, are given for the first time. Estimates of the seasonal variability of thermohaline characteristics of eddy cores are given for the Lofoten Basin of the Norwegian Sea; it is shown that the greatest differences in thermohaline characteristics of eddies in the Lofoten Basin are manifested in temperature anomalies.

Theoretical and practical significance of the work

The theoretical significance of the results obtained consists in obtaining a modern and comprehensive understanding of the mesoscale eddy dynamics of various parts of the Global Ocean based on the analysis of a wide range of satellite and model data. The practical significance of the results obtained lies in a more accurate understanding of the contribution that mesoscale eddy structures have on the transport of heat, salt, energy, and the bioproductivity of parts of the world's oceans. The work performed from a new perspective allows us to evaluate the influence of topography on the propagation of both monopole and dipole mesoscale eddy structures.

An assessment of the credibility of the results

The reliability of the results obtained is determined by the representativeness of the data used: reanalysis data, as well as model data. The validity of the scientific statements submitted for defense, conclusions, and recommendations of the

dissertation research is ensured by a proven methodology and the use of modern and relevant methods of data processing and analysis. The results of the work have been published, among other things, in leading journals for this specialty (at the Q1 and Q2 levels), as well as presented at national and international conferences. Individual research results have been awarded at conferences and scientific paper competitions.

The research carried out in the framework of this work was supported by grants:

- RFBR No. 20-05-00066: "Characteristics of Rossby waves in jet streams using remote sensing data";
- Russian Science Foundation No. 22-27-00004: "Investigation of the dynamics of isolated vortices in the ocean using remote sensing, in situ, and model data."

Publication and approbation of research results

21 articles have been published on the research topic (15 in Russian, 6 in English). All articles have been published in periodicals: 20 articles in periodicals included in the Web of Sciences/Scopus list. List of published papers on the research topic:

1. **Travkin V.S.**, Belonenko T.V. Seasonal variability of mesoscale eddies of the Lofoten Basin using satellite and model data. Russian Journal of Earth Sciences. 2019, V. 19, ES5004, doi:10.2205/2019ES000676. (RISC, HAC, WoS, Scopus).
2. **Travkin V.S.**, Belonenko T.V. Assessment of the depth of winter convection in the Lofoten Basin of the Norwegian Sea and methods for its assessment. *Gidrometeorologiya i ekologiya*. 2020, № 59, C. 67–83, doi: 10.33933/2074-2762-2020-59-67-83 (RISC).
3. Belonenko T.V., **V.S. Travkin**, A.V. Koldunov, D.L. Volkov Topographic experiments over dynamical processes in the Norwegian Sea. 2021. *Russ. J. Earth. Sci.* 21. ES1006, doi:10.2205/2020ES000747. (RISC, HAC, WoS, Scopus).
4. **Travkin V.S.**, Belonenko T.V. Study of the Mechanisms of Vortex Variability in the Lofoten Basin Based on Energy Analysis, *Physical Oceanography*, 2021, V. 28, I. 3, P. 294–308. DOI: 10.22449/1573-160X-2021-3-294-308 (RISC, HAC, WoS, Scopus).

5. **Travkin V.**, Belonenko T., Budyansky M., et al. Quasi-Permanent Mushroom-like Dipole in the Lofoten Basin. *Pure and Applied Geophysics*, 2022, 179(6), P. 465–482. DOI: 10.1007/s00024-021-02922-9. (RISC, HAC, WoS, Scopus).
6. **Travkin V.S.**, Belonenko T.V., Kochnev A.V. Topographic waves in the Kuril region, *Sovremennyye problemy distantsionnogo zondirovaniya Zemli iz kosmosa*. 2022. T. 19. №5. C. 222–234, DOI: 10.21046/2070-7401-2022-19-5-222-234. (RISC, HAC, Scopus).
7. **Travkin V.S.**, Belonenko T.V., Kubryakov A.A. Cold Spot over the Lofoten Vortex, *Izv. Atmos. Ocean. Phys.*, 2022, 58, P. 1458–1469. <https://doi.org/10.1134/S0001433822120246> (RISC, HAC, Scopus).
8. **Travkin V.S.**, Zhmur V.V., Belonenko T.V. Contribution of mesoscale eddies to energy of the Lofoten Basin, *Russ. J. Earth. Sci.*, 2022, V. 22, ES4002, DOI: 10.2205/2022ES000802. (RISC, HAC, WoS, Scopus).
9. Zhmur, V.V., **Travkin, V.S.**, Belonenko, T.V. and Arutyunyan, D.A. Transformation of Kinetic and Potential Energy during Elongation of a Mesoscale Vortex. *Physical Oceanography*, 2022, 29(5), P. 449–462. doi:10.22449/1573-160X-2022-5-449-462 (RISC, HAC, WoS, Scopus).
10. Akhtyamova, A.F., **Travkin V.S.** Investigation of Frontal Zones in the Norwegian Sea. *Physical Oceanography*, 2023, 30(1), P. 62–77. doi:10.29039/1573-160X-2023-1-62-77 (RISC, HAC, WoS, Scopus).
11. Gnevyshev V.G., **Travkin V.S.**, Belonenko T.V. Topographic Factor and Limit Transitions in the Equations for Subinertial Waves. *Fundamental and Applied Hydrophysics*. 2023, 16, 1, P. 8–23. doi:10.48612/fpg/92rg-6t7h-m4a2 (RISC, HAC, Scopus).
12. Zhmur V.V., Belonenko T.V., **Travkin V.S.**, Novoselova E.V., Harutyunyan D.A., Raj R.P. Changes in the Available Potential and Kinetic Energy of Mesoscale Vortices When They Are Stretched into Filaments. *J. Mar. Sci. Eng.*, 2023, 11, 1131. <https://doi.org/10.3390/jmse11061131>. (RISC, HAC, WoS, Scopus).

13. **Travkin V.S.**, Akhtyamova A.F. Spatial Variability of the Frontal Zones and its Eddies Generated in the Norwegian Sea. *Russian Journal of Earth Sciences*. 2023, No. 3. P. 1–14. DOI: <https://doi.org/10.2205/2023es000844>. (RISC, HAC, WoS, Scopus).
14. Khudyakova S.P., **Travkin V.S.**, Belonenko T.V. Mesoscale eddies of the Aleutian Trench. *Sovremennye problemy distantsionnogo zondirovaniya Zemli iz kosmosa*, 2023, Vol. 20, No. 6, P. 211–221. DOI: 10.21046/2070-7401-2023-20-6-211-221 (HAC, WoS, Scopus).
15. Gnevyshev V.G., **Travkin V.S.**, Belonenko T.V. Group Velocity and Dispersion of Buchwald and Adams Shelf Waves. A New Analytical Approach. *Fundamental and Applied Hydrophysics*. 2023, 16, 2, P. 8–20. doi:10.59887/2073–6673.2023.16(2)-1 (RISC, HAC, Scopus).
16. **Travkin V.S.**, Belonenko T.V., Kochnev A.V., Feoktistova V.N. Mesoscale eddies in the South Pacific Ocean. *Sovremennye problemy distantsionnogo zondirovaniya Zemli iz kosmosa*, 2024, V. 21, № 1, P. 286–298. DOI: 10.21046/2070-7401-2024-21-1-286-298. (RISC, HAC, Scopus).
17. Belonenko T.V., **Travkin V.S.**, Kochnev A.V. Review of studies on the distribution of Antarctic krill accumulations in the Scotia Sea and analysis of mesoscale dynamics of its habitat. *Vestnik of Saint Petersburg University. Earth Sciences*, 2024, 69 (1), P. 108–127. <https://doi.org/10.21638/spbu07.2024.106> (RISC, HAC, WoS, Scopus).
18. Gnevyshev V.G., **Travkin V.S.**, Belonenko T.V. Mixed Topographic-Planetary Waves in a Stratified Ocean on a Background Flow. *Pure Appl. Geophys.* 2024, V. 181, P. 2359–2371. <https://doi.org/10.1007/s00024-024-03527-8> (WoS, Scopus).
19. **Travkin V.S.**, Gnevyshev V.G., Belonenko T.V. Mesoscale eddies on the continental slope of the New Zealand Plateau based on altimetry data. *Sovremennye problemy distantsionnogo zondirovaniya Zemli iz kosmosa*, 2024, V. 21, №3, P. 221–233, DOI: 10.21046/2070-7401-2024-21-3-221-233 (RISC, HAC, Scopus).

20. Novoselova E.V., **Travkin V.S.**, Lebedeva M.A., Udalov A.A., Budyansky M.V., Belonenko T.V. Features of the vortex structures in the fields of Eulerian and Lagrangian hydrological characteristics for the Northwest Pacific. Vestnik of Saint Petersburg University. Earth Sciences, 2024, 69 (2), P. 372–388. <https://doi.org/10.21638/spbu07.2024.209> (RISC, HAC, Scopus)
21. **Travkin V.S.**, N.A. Tikhonova, E.A. Zakharchuk Mesoscale Eddies of the Baltic Sea according to the Physical Reanalysis // Russian Meteorology and Hydrology. 2024. V. 49. P. 784–794. <https://doi.org/10.3103/S1068373924090048> (RISC, HAC, Scopus).

The results of this study have been presented at the following international and national conferences:

- 1) **Travkin V.S.**, Belonenko T.V., Seasonal and interannual variability of characteristics of mesoscale vortices of the Lofoten Basin according to satellite data, XVII All-Russian Open Conference Modern Problems of Remote sensing of the Earth from space, Moscow, ICI RAS, November 11-15, 2019, <http://conf.rse.cosmos.ru/files/books/2019/7536.htm>
- 2) **Travkin V.S.** Seasonal and interannual variability of vortices of the Lofoten Basin, Proceedings of the international scientific and practical conference of students, postgraduates and young scientists "Theory and practice of modern geographical research", dedicated to the 180th anniversary of the Russian traveler and naturalist, researcher of Central Asia N. M. Przhevalsky in the framework of the XV Great Geographical Festival.: The Calligrapher Publishing House, 2019. pp. 123-125, ISBN 978-5-90363-273-2
- 3) **Travkin V.S.**, Belonenko T.V. Seasonal and interannual variability of mesoscale vortex characteristics in the Lofoten Basin based on satellite and field data, Proceedings of the III All-Russian Conference "Hydrometeorology and Ecology: Achievements and Development Prospects". Saint Petersburg: KHIMIZDAT, 2019, p. 841, ISBN 978-5-93808-336-3

- 4) **Travkin V.S.**, Mamajanyan A.G., Features of the distribution of water temperature in the Keret Bay in the summer of 2018, Belomorskaya Student Scientific session of St. Petersburg State University — 2019. Abstracts of reports. — Saint Petersburg: Svo Publishing House, 2019, pp. 69-70, ISBN 978-5-4386-1678-8
- 5) **V.S. Travkin**, A.M. Fedorov, T.V. Belonenko Features of winter thermohaline characteristics according to reanalysis ARMOR 3D in the Labrador Sea, Marine sciences and modern technologies for sustainable development: abstracts of the 26th International Conference of the Pacific Congress of Marine Sciences and Technologies (PACON-2019), July 16-19, 2019 Vladivostok, Russia. Vladivostok: TOI FEB RAS, 2019, p. 59, ISBN 978-5-6043211-0-2
- 6) **V.S. Travkin**, T.V. Belonenko, Study of seasonal variability of amount and thermohaline features of mesoscale eddies in the Lofoten Basin, Marine sciences and modern technologies for sustainable development: abstracts of the 26th International Conference of the Pacific Congress of Marine Sciences and Technologies (PACON-2019), July 16-19, 2019, Vladivostok, Russia. Vladivostok: TOI FEB RAS, 2019, p. 60, ISBN 978-5-6043211-0-2
- 7) **Travkin V.S.**, The influence of topography and deep convection on the Lofoten vortex based on satellite and model data, Materials of participants of the XVI Great Geographical Festival dedicated to the 200th anniversary of the discovery of Antarctica by the Russian expedition led by Thaddeus Bellingshausen and Mikhail Lazarev, St. Petersburg: Svo publishing House, 2020, p. 210, [Electronic edition], ISBN 978-5-4386-1902-4
- 8) **Travkin V.S.** The influence of deep convection and topography on the Lofoten vortex based on satellite and model data. Materials of the International Youth Scientific Forum "LOMONOSOV 2020", 2020. https://lomonosov-msu.ru/archive/Lomonosov_2020/index.htm
- 9) **Travkin V.S.**, Belonenko T.V. Interannual and seasonal variability of the characteristics of mesoscale vortices of the Lofoten Basin according to remote sensing data, Proceedings of the V All-Russian Scientific Conference of Young

Scientists, Kaliningrad, May 18-22, 2020 [Electronic resource]. Kaliningrad: JSC IO RAS, p. 179, ISBN 978-5-9906839-1-4

10) Ivanov K.D., **Travkin V.S.** Mushroom-shaped currents of the Lofoten Basin according to satellite data // Proceedings of the 18th All-Russian Open Conference "Modern problems of remote sensing of the Earth from space". Moscow: IKI RAS, 2020. P. 151. DOI 10.21046/18DZZconf-2020a <http://conf.rse.geosmis.ru/files/books/2020/8270.htm>

11) **Travkin V.S.**, Belonenko T.V. Kinetic and potential energy of vortices of the Lofoten Basin from satellite and field data // Proceedings of the 18th All-Russian Open Conference "Modern problems of remote sensing of the Earth from space". Moscow: IKI RAS, 2020. P. 182. DOI 10.21046/18DZZconf-2020a <http://conf.rse.geosmis.ru/files/books/2020/8237.htm>

12) **Travkin V.S.**, Belonenko T.V. Kinetic and potential energy of the Lofoten Basin based on satellite data, Proceedings of the IV All-Russian Conference "Hydrometeorology and Ecology: Achievements and development Prospects"/L. N. Karlin MGO 2020. Saint Petersburg: KHIMIZDAT, 2020. pp. 350-352, ISBN 978-5-93808-367-7

13) Ivanov K.D., **Travkin V.S.** Mushroom-shaped currents of the Lofoten Basin according to the GLORYS12V1 reanalysis, Proceedings of the IV All-Russian Conference "Hydrometeorology and Ecology: Achievements and development Prospects"/L. N. Karlin MGO 2020. St. Petersburg: KHIMIZDAT, 2020. PP. 179-180, ISBN 978-5-93808-367-7

14) **Travkin V.S.** Variability of kinetic and potential energy of the Lofoten Basin based on satellite data, Collection of materials by participants of the XVII Great Geographical Festival dedicated to the 195th anniversary of the Russian circumnavigation of the world by F.P. Litke (1826-1829). 2021. pp. 198-200.

15) **Travkin V.S.**, Belonenko T.V. Investigation of the potential and kinetic energy of the Lofoten Basin based on GLORYS12V1 reanalysis data, Abstracts of the All-Russian Scientific Conference of the Seas of Russia: The Year of Science and

Technology in the Russian Federation – The United Nations Decade of Ocean Sciences, 2021, pp. 325-326.

16) **Travkin V.S.**, Belonenko T.V. Study of a mushroom-shaped dipole in the Lofoten Basin based on GLORYS12V1 reanalysis data // Proceedings of the 19th International Conference "Modern Problems of Remote Sensing of the Earth from Space". Moscow: IKI RAS, 2021. C. 206. DOI 10.21046/19DZZconf-2021a <http://conf.rse.geosmis.ru/files/books/2021/8714.htm>

17) Akhtyamova A. F., **Travkin V.S.** Study of the frontal zones of the Norwegian Sea, Abstracts of the All-Russian scientific conference seas of Russia: Challenges of Russian Science, 2022. pp. 57-59.

18) **Travkin V.S.**, Belonenko T.V. Topographic Rossby waves and Kelvin double waves of the Kuril-Kamchatka trench, Abstracts of the All-Russian Scientific Conference Seas of Russia: Challenges of Russian Science, 2022, pp. 153-154.

19) **Travkin V.S.**, Zhmur V.V., Belonenko T.V. Contribution of mesoscale vortices to the energy of the Lofoten Basin, Abstracts of the All-Russian Scientific Conference Seas of Russia: Challenges of Russian Science, 2022, pp. 154-155.

20) **Travkin V.S.**, Zhmur V.V., Belonenko T.V. The contribution of mesoscale vortex energy to the energy of the Lofoten Basin // Proceedings of the 20th International Conference "Modern Problems of Remote Sensing of the Earth from Space". Moscow: IKI RAS, 2022. P. 222. DOI 10.21046/20DZZconf-2022a <http://conf.rse.cosmos.ru/files/books/2022/9103.htm>

21) **Travkin V.S.**, Belonenko T.V. Topographic waves of the Kuril-Kamchatka trench, Proceedings of the VII All-Russian Scientific Conference of Young Scientists "INTEGRATED STUDIES of the WORLD OCEAN" (KIMO-2023), 2023, pp. 186-188.

22) **Travkin V.S.**, Zhmur V.V., Belonenko T.V. Spatial and temporal evolution of the energy of mesoscale vortices of the Lofoten Basin, Proceedings of the VII All-Russian Scientific Conference of Young Scientists "INTEGRATED STUDIES of the WORLD OCEAN" (KIMO-2023), 2023, pp. 184-186.

23) **Travkin V.S.**, Tikhonova N.A., Zakharchuk E.A. Marine heat waves in the Baltic Sea, International Scientific and Practical Conference of Students, Postgraduates and Young Scientists, XX Great Geographical Festival, 2024.

The results obtained in the framework of this work have been awarded:

1. Diploma for the best report at the section "Exploration of the seas and shelf zones" of the International Scientific and Practical Conference of Students, postgraduates and young Scientists "Theory and practice of modern Geographical research" within the framework of the XV Great Geographical Festival. 2019. Topic of the report: "Seasonal and interannual variability of vortices of the Lofoten Basin".
2. Diploma of the III degree for the III place in the Competition of scientific papers of students and postgraduates of St. Petersburg in the field of oceanology. 2020. Topic of the paper: "Energy of the Lofoten Basin of the Norwegian Sea.
- " 3. Diploma of the winner of the 2020 Contest of term papers, theses and scientific papers dedicated to the 200th anniversary of the discovery of Antarctica by Russian navigators. 2021
4. Diploma of the winner of the International Olympiad of Students and young specialists of the Metropolitan Science (Re)Search in the field of Earth Science. 2022.
5. Diploma of the II degree for the II place in the Competition of scientific papers of students and postgraduates of St. Petersburg in the field of oceanology, 2022. The topic of the work: "Rossby topographic waves in the Kuril Trench area.
6. Diploma of the II degree for the II place in the Competition of scientific papers of students and postgraduates of St. Petersburg in the field of oceanology, 2023 The topic of the paper is "Mesoscale vortices of the Baltic Sea according to regional reanalysis data".
7. Diploma for the best oral presentation at the VIII All-Russian Conference of Young Scientists on Integrated Ocean Research (KIMO-2024). The topic of the work is "Marine heat waves of the Baltic Sea".

Author's personal contribution

The author's personal contribution to the dissertation is expressed in an in-depth analysis and development of new approaches to the study of mesoscale vortices, which has both theoretical and practical significance for Earth science.

The author independently proposed the implementation of new mathematical models that describe the interaction of mesoscale vortices with large-scale processes in the ocean. These models allow us to more accurately account for the effect of vortices on the general circulation of the ocean. In particular, the author conducted a detailed analysis of the influence of the bottom topography of the Lofoten Basin on the generation of the quasi-permanent Lofoten Vortex. As a result, a connection was established between the shape of the basin and the dynamics of the vortex, which confirms the hypothesis that topographic features play a crucial role in the formation of vortex structures.

The author has developed a methodology for estimating the available potential energy of the Lofoten Vortex, which exceeds its kinetic energy by an order of magnitude. This study included an analysis of trends and seasonal changes, which allowed us to identify significant dependencies and confirm the hypothesis about the influence of barotropic instability on the dynamics of the eddy.

In the course of the work, the author studied the graphs of the rate of transformation of barotropic instability, revealing multidirectional flows in the eddy zone. He also described a dipole structure in winter and a tripole structure in summer, which deepens the understanding of the seasonal variability of vortex processes.

The author established the existence of a quasi-permanent mushroom-shaped dipole in the Lofoten Basin, explaining its formation by the interaction of circulation with the bottom. This discovery has important implications for understanding the dynamics of ocean currents and their relationship to topography.

The author also investigated mesoscale eddies in the Kuril region, identifying four systems of topographic waves. This study showed how anticyclones and cyclones manifest themselves in the form of shelf and trough waves, which contributes to a deeper understanding of the structure of ocean currents.

In addition, the author actively participated in writing articles and publications on the research topic, which contributed to the dissemination of knowledge about mesoscale vortices among both Russian and international scientists. His work became an important contribution to the development of oceanographic science.

The structure of the thesis

The thesis consists of an introduction and 3 chapters, contains 164 pages and includes 47 illustrations and 7 tables in the main text, as well as a list of references from 179 works by authors.

The Introduction presents the goals and objectives of the dissertation, provides the main provisions submitted for defense, the relevance and novelty of the scientific work, as well as its theoretical and practical significance. A physical and geographical description of the Norwegian and Baltic Seas, as well as the North and South Pacific is given. A list of publications and conferences on the research topic is also provided.

Chapter 1 describes the data and methods used. The monopole and dipole eddies of the Lofoten Basin are studied in detail, the energy of the Lofoten Basin and, in particular, the Lofoten Vortex are considered. The role of topography in the eddy mesoscale dynamics of the Norwegian Sea is analyzed.

Chapter 2 describes the data and methods used. The trajectories of mesoscale cyclones and anticyclones are studied in detail, and estimates of the main characteristics of eddies are given. Estimates of the contribution of topography, the beta effect, and other factors to the propagation of mesoscale vortices have been obtained.

Chapter 3 describes the methods and data used. The trajectories, as well as seasonal and interannual variability of the main characteristics of mesoscale eddies, are analyzed in detail using the method of automatic identification of eddies. Statistical estimates are provided for the parameters of cyclones and anticyclones.

In conclusion, the completed research is briefly summarized. The main conclusions of the thesis are given.

Acknowledgments

The author sincerely thanks his colleagues and co-authors for their support and collaboration. I would like to express my special gratitude to my supervisor, Dr. Sci. (Geogr.), Professor Tatiana Vasilievna Belonenko for her invaluable contribution to scientific development and assistance in working on her dissertation. The author expresses his gratitude to all the teachers of the Department of Oceanology of St. Petersburg State University for the knowledge and skills gained during their studies at the department.

Main scientific results

1. For mesoscale cyclones and anticyclones of the Lofoten Basin, the seasonal variability of their number, orbital velocity, amplitude, lifespan, radius, and thermohaline characteristics is estimated. A spatial distribution of cyclones and anticyclones is obtained for each season. It is shown that the number of anticyclones in the winter-spring period significantly exceeds the number of cyclones. The largest number of eddies of both types is recorded in the central and eastern parts of the Lofoten Basin of the Norwegian Sea (Travkin and Belonenko, 2019, p. 4, the degree of author's participation in obtaining this result is 80%).
2. Using the Kara and Montegut methods, estimates of the depth of winter convection in the Lofoten Basin were obtained. In March, the greatest mixed-layer depth, exceeding 400-500 meters, is observed in the area of the quasi-permanent anticyclonic Lofoten Vortex. Significant negative linear trends in the MLD were found for January and February, while significant positive linear trends were found for March and April (Travkin and Belonenko, 2020, pp. 75, 78, the degree of the author's participation in obtaining this result is 75%).
3. Using numerical experiments using the MITgcm model, it was found that the smooth shape of the Lofoten Basin with a decrease in the central part is a necessary factor for the formation of a quasi-permanent anticyclonic Lofoten Vortex. The Lofoten Vortex is located in the central part of the basin only when it is

topographically isolated from all sides. The greatest values of the MLD, as well as the eddy kinetic energy, are recorded in the area of the Lofoten Vortex and on the continental slope of Norway. A change in the topography of the seabed leads to a significant change in the intensity of winter convection and eddy kinetic energy. (Belonenko et al., 2021a, pp. 10–11, the degree of the author's participation in obtaining this result is 80%).

4. Estimates of the mean and eddy kinetic energy of the Lofoten Basin, as well as the Burger eddy number, and the available potential and kinetic energy of the Lofoten Vortex are obtained. At all the depths studied, the eddy kinetic energy exceeds the mean, and both types of energy are characterized by intensification in winter. A significant positive linear trend of $0.23 \cdot 10^{15}$ J/year was recorded for the available potential energy of the Lofoten Vortex. The layer from 0 to 300 m makes the greatest contribution to kinetic energy, and the layer from 600 to 900 m makes the greatest contribution to potential energy. The maximum barotropic energy conversion is observed in the area of the Lofoten Vortex and the Norwegian continental slope, with a dipole structure in the eddy area in winter and a tripole structure in summer. In winter, due to intense convection, there is a sharp increase in the rate of baroclinic energy conversion in the Lofoten basin (Travkin and Belonenko, 2021, pp. 300–303, the degree of the author's participation in obtaining this result is 65%).

5. Using Eulerian and Lagrangian maps, the structure and evolution of a mushroom-shaped dipole in the Lofoten Basin is analyzed in detail. In total, 48 mushroom-shaped dipoles with a life span of 19 to 45 days were found in the Lofoten Basin in 2013-2016. The dipole in question has a length of about 150 km, consists of a jet (about 40-60 km wide) and a "cap" of a cyclone and an anticyclone (about 170 km wide). Vertically, the dipole is clearly distinguished by temperature and salinity anomalies, and its dynamic signal can be traced from the surface to the very bottom. Due to the topography features, a mushroom-shaped dipole is constantly forming and then dissipating in the eastern part of the Lofoten Basin, which is

reflected on the mean current maps (Travkin et al., 2022c, pp. 472, 474, 478, the degree of the author's participation in obtaining this result is 70%).

6. Using the META3.2 DT it was found that cyclones and anticyclones in the Kuril-Kamchatka trench region manifest themselves as four systems of topographic waves, which are shelf and trench waves. The number of cyclones is twice as high as the number of anticyclonic eddies. Anticyclones propagate along the shelf in the form of shelf waves and along the seaward part of the trench, cyclones – along the inner side of the trench and along the topographic uplift. It was found that the contribution of topography to the propagation of the waves under consideration exceeds by several orders of magnitude the contribution of the other components of the effective beta effect (Travkin et al., 2022a, pp. 226-228, the degree of the author's participation in obtaining this result is 80%).

7. Using satellite images and reanalysis data, the formation of a "spot" of cold waters in the area of the Lofoten Vortex is considered. It was found that in the summer and autumn period, the outer dome of the lens of the Lofoten Vortex compresses isopycnets, lifting them up and destroying the surface heated layer, as a result of which a "spot" of cold water forms on the surface. Such cooling is accompanied by a decrease in the MLD, reaching 30 m by November. Cooling is also recorded according to the ERA5 atmospheric reanalysis, which indicates a decrease in the heat flow from the ocean to the atmosphere during the formation of the cold spot. It was found that the cold spot is displaced relative to the anomalies of the sea surface height, in half of the cases the displacement does not exceed 10 km (Travkin et al., 2022b, pp. 29, 33, the degree of the author's participation in obtaining this result is 65%).

8. Using the method of automatic eddy identification and GLORYS12V1 reanalysis, the components of kinetic and potential energy in the Lofoten Basin were analyzed. It is found that the potential energy is 2-3 times higher than the eddy kinetic energy. In winter, there is an intensification of both kinetic and potential energy, compared with the summer period. The highest values of total kinetic energy are recorded in the central part of the Lofoten Basin, potential energy – in the area

of the Lofoten Vortex, as well as on the periphery of the Lofoten Basin. The kinetic energy of the eddies is 7%, and the potential energy of the eddies is 8% of the total energy of the basin, respectively (Travkin et al., 2022d, pp. 6-7, the degree of the author's participation in obtaining this result is 75%).

9. The paper analyzes the energy transformation of an elongating mesoscale eddy. It was found that despite a 4-fold increase in the longitudinal scale of the eddy, its effective radius varies slightly. An increase in the eddy oblateness parameter of the analyzed eddy is associated with an increase in the frequency of buoyancy. The potential energy of the eddy is 1.5 times higher than its kinetic energy, and during the transformation of the eddy, its kinetic energy decreases by 3 times, and its potential energy by 1.7 times (Zhmur et al., 2022, pp. 473-475, the degree of the author's participation in obtaining this result is 80%).

10. Using GLORYS12V1 reanalysis, spatial characteristics of the frontal zones of the Norwegian Sea were obtained. For the first time, estimates of their probability, as well as seasonal and interannual variability are given. The correlation coefficients of the frontal zones with the NAO and AO indices are calculated. It was found that the frontal zones can be traced at depths from 0 to 600 m. In the area of the Lofoten Vortex, the Mohn Ridge, and the Norwegian slope, significant recurrence (more than 50%) of frontal zones with significant gradients was found. In the intermediate layer in the central part of the Lofoten Basin, the existence of the frontal zone of the Lofoten Vortex was recorded (Akhtyamova and Travkin, 2023, pp. 75-77, the degree of the author's participation in obtaining this result is 65%).

11. The paper considers topographic subinertial waves propagating on the shelf and ocean trench. Two classes of localized solutions have been constructed for offshore and trench waves. It is established that for trench waves, the transverse wavenumber is a function of the longitudinal wavenumber. The stitching of trench and shelf waves was performed for the first time. It has been found that waves of both types can propagate as eddies along the shelf both to the southwest (longer waves) and to the northeast (shorter waves) (Gnevyshev et al., 2023a, p. 15-16, 20, the degree of the author's participation in obtaining this result is 70%).

12. The paper considers aspects of the interaction of mesoscale eddies with the barotropic flow. It was found that in 22 days the eddy transforms into a filament, while its total energy decreases by 2.3 times. It is established that the stretching of the eddy leads to a loss of energy, as well as to its redistribution from the mesoscale to the submesoscale. The lost part of the energy is returned to the flow and contributes to the formation of the phenomenon of a reverse cascade of energy (Zhmur et al., 2023, pp. 4-5, 7, 9, 11, the degree of the author's participation in obtaining this result is 60%).

13. Using the META3.2 DT and GLORYS12V1 reanalysis consider the spatial variability of the frontal zones of the Norwegian Sea, as well as the eddies forming in them. The largest volume of frontal zones was recorded in the autumn-winter period, while the average thickness of the thermal frontal zones can exceed 600 m, and of the haline zones – 200 m. Eddies of both types are generated in the frontal zones of the Norwegian Sea and then travel hundreds of km, dissipating in the Lofoten and Norwegian basins. Long-lived mesoscale eddies more often leave the boundaries of the frontal zones. In the winter and spring period, there is an increase in the number of eddies. A significant linear positive linear trend was found for the number of anticyclones and cyclones (Travkin and Akhtyamova, 2023, pp. 5, 8-10, the degree of the author's participation in obtaining this result is 90%).

14. It has been established that anticyclones spread along the shelf zone of the Aleutian Islands, and cyclones along the Aleutian Trench with depths of 5-7 km. The largest number of anticyclones was recorded south of the Near and Rat islands. The predominance of the topographic factor among the terms of the dispersion equation for Rossby barotropic topographic waves is found in most of the study area. It was found that the separation of eddies from the trough occurs under the influence of a current in the region of 171-176°E (Khudyakova et al., 2023, pp. 215-217, the degree of the author's participation in obtaining this result is 70%).

15. The analysis of the propagation of shelf waves for the exponential convex profile of the shelf is carried out. New analytical expressions for group velocity and dispersion are found. It is confirmed that shelf waves propagating along the coast

manifest themselves as chains of moving coherent eddies of different polarities, while leaving the coast on the right. Graphs of topographic flow profiles for the first three modes have been obtained, and self-similarity has been established for the extreme velocity of shelf currents from the curvature of topography (Gnevyshev et al., 2023b, p. 9, 15, 17, the degree of the author's participation in obtaining this result is 65%).

16. It was found that the maximum number of mesoscale eddies in the South Pacific is formed in the coastal region, as well as on the slopes of the Peruvian and Chilean trenches. The number of anticyclones per cell is maximum in the coastal strip at 38-48° S, for cyclones, similar values are typical for the entire coastal region. The Antarctic Circumpolar Current contributes to the formation of eddies, especially mesoscale cyclones. An anticyclone with a life span of more than 1600 days and a distance of more than 4500 km has been detected. Most eddies have a radius of 25-75 km, an amplitude of more than 5 cm, an orbital velocity of 5-15 cm/s, and a lifetime of no more than 50 days (Travkin et al., 2024a, pp. 289-290, 292, 294, the degree of the author's participation in obtaining this result is 80%).

17. Using the META3.2 DT, areas of localization of mesoscale eddies in the Scotia Sea were detected, with significantly more cyclones being generated than anticyclones. A predominantly eastern direction of eddy propagation has been detected. The increased values of eddy dynamics in the Scotia Sea are confirmed by the reconstructed altimetric data. Cyclones and anticyclones are characterized by topographic mapping (Belonenko et al., 2024, pp. 118-120, 122, the degree of the author's participation in obtaining this result is 75%).

18. For minor topography changes (for both positive and negative slopes), the asymptotics of the dispersion relation for the surface mode are obtained. It was found that the influence of topography on baroclinic waves is most significant in the long-wavelength part of the spectrum. It is established that the frequency and the western component of the phase velocity of the topographically modified first baroclinic mode can increase (with decreasing depth to the north) or decrease (with increasing depth to the north) depending on the nature of the slope of the continental slope. The

influence of topography on the western transmission of Rossby waves is analyzed (Gnevyshev et al., 2024, pp. 2366-2367, 2369, the degree of the author's participation in obtaining this result is 75%).

19. The existence of two mesoscale eddy systems has been discovered on the southeastern slope of the New Zealand Plateau, where anticyclones move along the upper slope boundary and cyclones along the lower one. Estimates of the kinematic and dynamic parameters of cyclones and anticyclones propagating over the New Zealand Plateau have been obtained. The topographical character of the origin of mesoscale eddies of the New Zealand Plateau is shown. The spectral problem of natural oscillations has been calculated for an exponential model of topography (Travkin et al., 2024c, pp. 224-225, 227, the degree of the author's participation in obtaining this result is 80%).

20. Using the Eulerian and Lagrangian approaches, the variability of the oceanological fields of the Northwestern Pacific is analyzed. Eddy structures and elements of large-scale circulation were detected on the Λ - and S-maps. Increased values of kinetic and available potential energy were found in the area of a large anticyclone near the Kuril Trench and in the area of the Kuroshio jet and its anticyclonic rings. Large anticyclones in the field of relative vorticity are characterized by a shielding effect (Novoselova et al., 2024, p. 376-377, 379, 382, the degree of the author's participation in obtaining this result is 60%).

21. Using the method of automatic identification of eddies in the Baltic Sea, the spatial distribution of mesoscale cyclones and anticyclones, as well as seasonal and interannual variability of their amplitude, life span, radius and number were obtained. Most cyclones and anticyclones have an amplitude of 0.05–0.25 m, a radius of 5-10 km, and a lifespan of about 2-3 days. The largest number of eddies was recorded in the Kattegat, the Gulf of Riga and the Gulf of Gdansk, as well as in some parts of the Gulf of Finland and the Gulf of Bothnia. The average ratio of the large and small semi-axes of eddies in the Baltic Sea is 1.58, which indicates a significant influence on the vortices of the background current (Travkin et al., 2024b, pp. 787-789, the degree of the author's participation in obtaining this result is 90%).

Key points of the defense:

1. The main factor in the generation of the quasi-permanent Lofoten Vortex is the topographic isolation of the Lofoten Basin, the bottom topography of which has the form of a bowl, as well as the system of currents in the region.
2. The available potential energy of the Lofoten vortex is an order of magnitude higher than the kinetic energy. The increase in available potential energy is confirmed by a significant positive trend and a decrease in the number of Burghers. The graphs of the rate of transformation of barotropic instability reflect multidirectional flows in the vortex zone, with a dipole structure observed in winter and a tripole structure in summer.
3. The existence of a quasi-permanent mushroom-shaped dipole in the Lofoten Basin is due to the interaction of circulation with the topography of the bottom.
4. In the Kuril region, mesoscale vortices form four systems of topographic waves, as a result of which anticyclones and cyclones manifest themselves as shelf and trough waves.
5. Mesoscale vortex structures of the Baltic Sea simultaneously occupy 2% of the sea area in winter and 4% in summer and horizontally represent elongated ellipses with a ratio of major and minor semiaxes equal to 1.58.

CHAPTER 1. THE NORWEGIAN SEA

1.1. Data

The following data sets are used to study the eddy dynamics of the Norwegian Sea:

1. Data from the Mesoscale Eddy Trajectory Atlas Product, freely available on the AVISO+ portal (<https://www.aviso.altimetry.fr/>). This data is based on information about the surface of the Global Ocean obtained from satellite altimeters for the period 1993-2017, which is later used to detect and track mesoscale cyclones and anticyclones (Chelton et al., 2011a). The algorithm determines anticyclones based on a set of criteria as areas of closed positive (negative) sea level anomalies on daily maps of the sea surface height with a spatial resolution of 0.25° in latitude and longitude. The algorithm tracks the evolution of the detected eddy structures up to the moment of their dissipation with a discreteness of one day. The Atlas of mesoscale eddies contains information about the following parameters:

- the amplitude (cm) is defined as the difference between the largest anomaly in the sea surface height inside the eddy and a similar value at its boundary;
- radius (km) is defined as the radius of a eddy, the boundary of which is limited by the maximum values of the orbital velocity;
- The orbital velocity (m/s) is calculated as the value of the average geostrophic velocity inside the closed area of the eddy;
- Life span (days) is defined as the number of days during which the eddy was traced in the level field.

2. GLORYS12V1 global ocean reanalysis data available on the Copernicus Marine Environment Monitoring Services (CMEMS) portal. The GLORYS12V1 contains information on temperature, salinity, u and v components of current velocities, sea surface height, and mixed-layer depth (MLD) of the Global Ocean for the period from 1993 to 2019. The spatial and temporal resolution of GLORYS12V1 is $1/12^\circ$ and one day, respectively, which makes it possible to use

this reanalysis to study the mesoscale eddy dynamics of various regions of the Global Ocean. The basis of the GLORYS12V1 is the NEMO model, atmospheric forcing is set using ECMWF ERA-Interim. Field measurements, data from altimeters, satellite information on sea surface temperature and sea ice concentration, as well as observations from ARGO buoys and marine gliders are assimilated into the reanalysis using a low-order Kalman filter. Vertically, the array contains information on 50 horizons from the surface to 5500 m.

3. The paper uses the results of numerical experiments of a regional hydrodynamic model based on the global atmospheric and ocean circulation model of the Massachusetts Institute of Technology (MITgcm). The spatial resolution of the data is 4 km, and the vertical array contains 50 levels in increments from 10 m near the surface to 456 m at the bottom. The bathymetry of the model is set using the GEBCO model with a spatial resolution of 1'. Oceanic boundary conditions are set using the optimal implementation of the global ECCO2 model, the initial conditions are from the World Ocean Atlas 2009 database. Atmospheric forcing is determined using JRA55 reanalysis. The time discreteness of the data is one day. To conduct the experiments, the work uses 4 variants with different topography of the Norwegian Sea: TOPO1, TOPO2, TOPO3 and TOPO4 (Fig. 1.1). TOPO1 represents a real topography. In the TOPO2 experiment, the periphery of the Norwegian and Lofoten Basins, as well as the continental slope of Norway, were made level with a depth of 3,000 m. The topography in the TOPO3 experiment is close to TOPO2, but the relief of the Norwegian basin is leveled, and the Lofoten Basin is removed. The TOPO4 experiment uses real topography, but instead of the Lofoten Basin, there is a flat surface with a depth of 2500 m (Fig. 1.1).

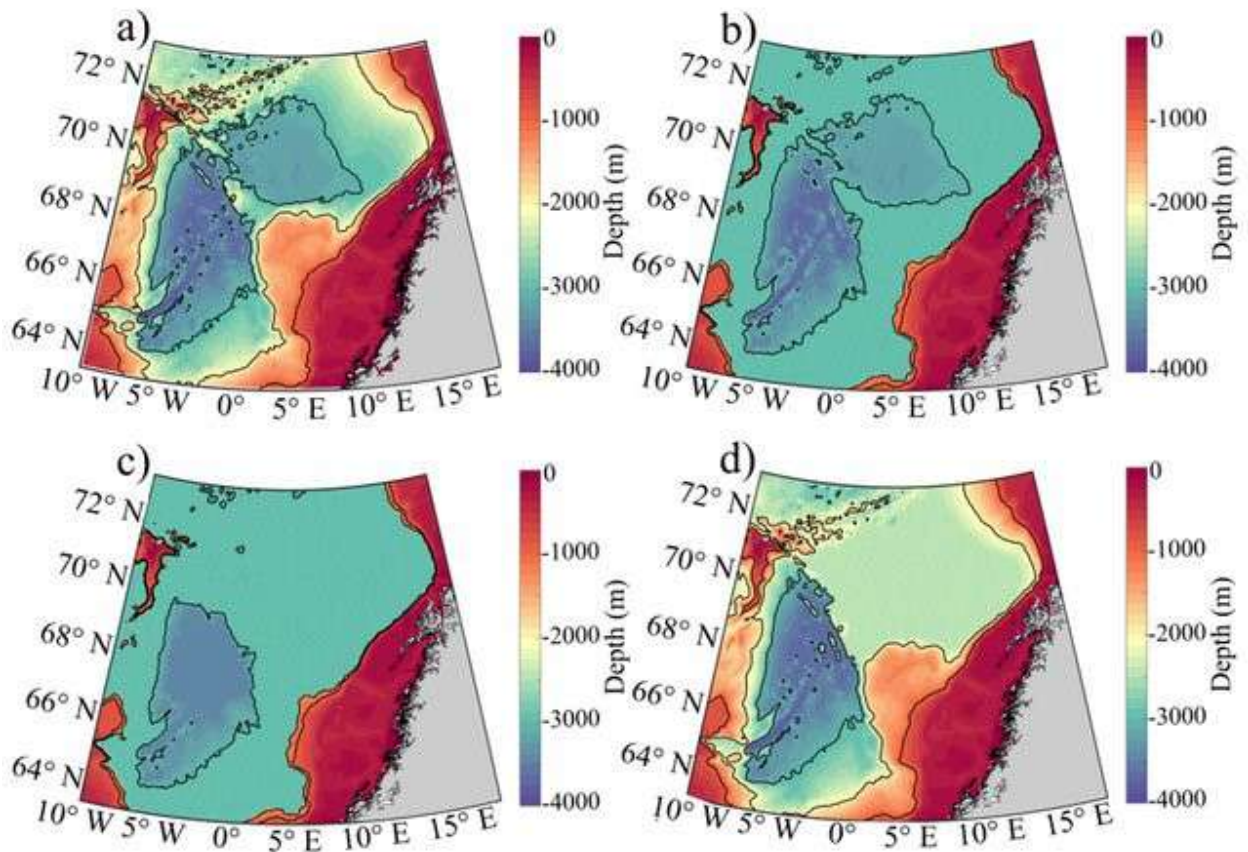


Figure 1.1. The topography of the seabed (m) during the TOPO1-TOPO4 experiments. Isobates are carried out every 1000 m.

4. ETOPO1 is a global bathymetric-topographic digital model of the earth's surface with a spatial resolution of 1' in latitude and longitude. The seabed bathymetry is based on field observations from the Japan Ocean Data Center (JODC), the Mediterranean Scientific Commission (CIESM), the National Geophysical Data Center (NGDC), and the Caspian Environmental Program (CEP).

1.2. Methods

Calculation of the mixed-layer depth (MLD)

Currently, there are several ways to calculate the MLD, among which it is customary to distinguish two main methods that are based on the density gradient and are later used to calculate the MLD in the Lofoten Basin. The first method includes the Montegut method, which allows determining the MLD as the value of the depth for

which the density gradient exceeds the value for a given density (Montegut et al., 2004):

$$\frac{\Delta\sigma_t}{\Delta z} = \left(\frac{\partial\sigma_t}{\partial z} \right)_c,$$

where $\Delta\sigma_t$ - different of the potential density $\sigma_t=(\rho-1000)$ $\text{kg}\cdot\text{m}^{-3}$ at a vertical distance Δz , ρ – sea water density, $\left(\frac{\partial\sigma_t}{\partial z} \right)_c$ – a predefined gradient of conditional density. This method is recommended for profiles with high vertical data resolution. The second method of determining the MLD is the Kara method, in which the MLD is defined as the depth at which the water temperature has changed for the first time by a certain value compared to the temperature of the sea surface (Kara et al., 2000). The empirical criterion of water density is found as the difference between the density of water on the sea surface $\sigma(T_r, S_r)$, where T_r and S_r – sea surface temperature and salinity, and $\sigma(T_h, S_h)$ – the density of water with the same salinity, but at a temperature lower by a certain amount of the criterion:

$$\Delta\sigma=\sigma(T_r, S_r)-\sigma(T_h, S_h),$$

where $T_h=(T_r-0.1)$ - The water temperature at the studied horizon, 0.1°C is the selected criterion value.

Thus, the first horizon on which the density difference with the selected horizon will exceed $\Delta\sigma$ and it will be considered MLD. This method teaches the nonlinear effect of the seawater composition equation, so the significance criteria depend on both salinity and seawater temperature (Nilsen and Falck, 2006). Based on the analysis of multiple vertical profiles, this author's method shows that the highest optimal criterion for most areas of the Global Ocean is 0.8°C . It is also worth noting that when selecting criteria for determining the MLD, one should always study the hydrological conditions of the area under study (Kara et al., 2000).

Calculation of kinetic and potential energy of the Lofoten Basin

The following formulas are used to calculate Mean Kinetic Energy (MKE) and Eddy Kinetic Energy (EKE), as well as eddy Available Potential Energy (APE) (Volkov et al., 2015; Martínez-Moreno et al., 2019):

$$\text{MKE} = 0.5 \left(\overline{u^2} + \overline{v^2} \right),$$

$$\text{EKE} = 0.5 \left(\overline{u'^2} + \overline{v'^2} \right),$$

where \bar{u} and \bar{v} – time-averaged velocity components; u' и v' – anomalies of the velocity components calculated for each grid point and then averaged over the period 2010-2018:

$$u' = u - \bar{u},$$

$$v' = v - \bar{v}.$$

For the region of the Lofoten vortex, limited by a radius of $R = 80$ km, the volume values of the Available Potential Energy (APE_V) and eddy Kinetic Energy (KE) were calculated using the volume integral (Hebert, 1988; Fernández-Castro et al., 2020):

$$\text{APE}_V = \pi \int_0^R \int_{-H}^0 g z [\rho_{\text{ref}}(z) - \rho(r, z)] r dr dz,$$

$$\text{KE} = 0.5 \pi \int_0^R \int_{-H}^0 \rho(r, z) U(r, z)^2 r dr dz,$$

where H – maximum depth (calculated as 1000 m); ρ_{ref} – average potential density profile outside the Lofoten vortex ($r > 80$ km).

The paper also calculated the Burger vortex number using the formula (D'Asaro, 1988; Fernández-Castro et al., 2020):

$$\text{Bu}_E = \text{KE} / \text{APE}_V.$$

To study the contribution of various sources to vortex energy, baroclinic (BC) and barotropic (BT) energy conversion rates are used. BC is responsible for the rate of MPE to APE conversion, which is one of the sources of mesoscale eddy formation, while BT demonstrates the rate of MKE to EKE conversion. Thus, BT is

the coefficient of barotropic transformation, the positive sign of which indicates the transfer of energy from average horizontal shifts to the vortex field. In turn, BC is the baroclinic conversion coefficient, the positive sign of which indicates the redistribution of energy from MPE (i.e., horizontal density gradients) into the eddy field. In other words, the source of the EKE is the baroclinic instability of the streams, during which EKE generation occurs at the expense of MPE (MPE → APE → EKE) and barotropic transformation (MKE → EKE) (Xu et al., 2020). We used the following formulas to calculate BC and BT (Eden and Böning, 2002; Zhan et al., 2016; Xu et al., 2020):

$$BC = -\frac{g^2}{N^2 \rho_0} \left(\overline{u' \rho'} \frac{\partial \overline{\rho}}{\partial x} + \overline{v' \rho'} \frac{\partial \overline{\rho}}{\partial y} \right),$$

$$BT = -\rho_0 \left(\overline{u'^2} \frac{\partial \overline{u}}{\partial x} + \overline{v'^2} \frac{\partial \overline{v}}{\partial y} + \overline{u' v'} \left[\frac{\partial \overline{v}}{\partial x} + \frac{\partial \overline{u}}{\partial y} \right] \right),$$

where g – gravitational acceleration, ρ_0 – background density of seawater, N – frequency of buoyancy.

Modelling of Lagrangian particles

To study the evolution of eddy structures, the Lagrangian method is used, the essence of which is to seed the studied area with tens of thousands of markers and then track them in the GLORYS12V1 reanalysis velocity field. For this, advection equations are used for a set of passive tracers on the Earth's sphere.:

$$\frac{d\lambda}{dt} = u(\lambda, \varphi, t), \quad \frac{d\varphi}{dt} = v(\lambda, \varphi, t),$$

where u and v – angular zonal and meridional velocity, φ and λ – latitude and longitude.

In addition to Lagrangian particles, Lagrangian characteristics (so-called "Lagrangian maps") were calculated and analyzed, which contain information not only about the hydrophysical conditions at the present time, but also about the history of the origin of waters and their subsequent evolution (Prants et al., 2011a, b). The angular velocity is related to the linear velocity by the ratio

$U = u \left(\frac{0.864}{1.853} \right) \left(\frac{1}{\cos \varphi} \right)$, $V = v \left(\frac{0.864}{1.853} \right)$, where U and V given in angular minutes per day, and u and v in cm/sec. The use of angular velocities makes it possible to apply the equations of motion in the simplest form.

Passive particles are tracked on the surface and at a horizon of 541 m. This horizon was chosen because in most cases the core of eddy structures is located at this depth. (Sandalyuk et al., 2020). Study area (67.0-71.5°N, 2.0-11.5°E) In the initial time period, a field of 500×500 passive particles was filled, after which their subsequent evolution was monitored.

To find the centers of eddies, elliptical points (stable stationary points in the velocity field) are calculated, while areas of instability at the boundaries of eddies are associated with hyperbolic points (unstable stationary points) (Prants et al., 2017). Elliptical points in the centers of cyclones and anticyclones are marked with blue and red triangles, and correspond to areas where rotation prevails over deformation. At hyperbolic points (crosses on maps), deformation prevails over rotation. On each map, the particle trajectories were calculated for 15 days in the opposite direction, starting from the date indicated on the corresponding map. After that, the length of the trajectories (S-maps) and the Lyapunov exponent (Λ -maps) were calculated using the following formulas (Prants et al., 2011a):

$$S = \int_0^T \sqrt{(\lambda'(t))^2 \cos^2 \varphi(t) + (\varphi'(t))^2} dt,$$

$$\Lambda(t, t_0) = \frac{\ln \sigma(t, t_0)}{t - t_0},$$

where $\varphi'(t)$ and $\lambda'(t)$ calculated as time derivatives between the initial and final position of the particle, $\sigma(t, t_0)$ – the maximum singular value of the matrix, $t - t_0$ – the integration period.

Thus, S-maps show the distance traveled by the particles over a specific time period. The darker the color on the S-map, the longer the trajectory of the corresponding particle. The boundaries between light and dark regions roughly coincide with the peripheries of mesoscale vortices and the location of Lagrangian

fronts (Prants et al., 2014b). The values on the Λ -maps quantify the rate of divergence of neighboring particles over a certain period of time. Areas with maximum values on Λ -maps usually correspond to areas with high values on S-maps (frontal zones). This is explained by the fact that both parameters are associated with unstable invariant manifolds of hyperbolic points (Prants et al., 2017). The so-called "ridges" represent areas where strong stretching of spots with passive particles has been observed in the recent past. In other words, if you place a spot of particles across the ridge, the particles on both sides of the ridge will move significantly faster than the particles in the central part crossing the ridge.

The method of automatic identification of eddy structures

Currently, there is an active development of methods for the automatic identification of eddy structures of the Global Ocean. They allow us to study in detail the evolution of eddies in both space and time (Chelton et al., 2011a; Faghmous et al., 2015; Raj et al., 2016; Yu et al., 2017; Travkin and Belonenko, 2019; Travkin et al., 2022b; Aguiar et al., 2022). Existing algorithms can be divided into two main groups. The first group is based on the physical properties and analysis of dynamic fields: in this group, eddies are defined as closed contours limited by a threshold value. As a rule, the parameters for identifying vortices are anomalies in the sea surface height, relative vorticity, or the Okubo-Weiss parameter. The second group includes geometric methods that use the shape or curvature of the flow to identify eddies. So, this method can be based on the use of streamlines.

To detect eddy structures in the Norwegian Sea, an algorithm is used that belongs to the first group, available at (<https://github.com/jfaghm/OceanEddies>) and is described in detail in the work (Faghmous et al., 2015). To detect eddies, this algorithm uses daily information about the sea surface height, defining eddies as closed contours with positive (negative) anomalies of the sea surface height in anticyclones (cyclones). Eddy detection begins by finding an extreme in the field of level anomalies, with one extreme corresponding to one anticyclone or cyclone. The

extremum is defined as the cell with the largest modulo value of the level anomaly in the 5×5 grid cell field. Next, the algorithm detects the contour of each eddy, while the eddy cannot have more than one extremum. The eddy trajectories are tracked as follows: an eddy detected at time t is then searched for at time $t+1$ based on the assumption that the eddy velocity is close to the propagation velocity of a long Rossby baroclinic wave. Next, the sizes of the eddies are compared at time points t and $t+1$ in order to make sure that the eddies are physically similar. In this algorithm, it is possible to create a so-called "false eddy", which allows you to track the trajectory of the eddy even if there are errors or omissions in the data. The algorithm used has a number of disadvantages, however, it demonstrates good accuracy, making it possible to successfully identify about 96% of mesoscale cyclones and anticyclones (Faghmous et al., 2015). The algorithm has been successfully applied in works (Zinchenko et al., 2019; Gordeeva et al., 2021; Travkin et al., 2022d; Travkin et al., 2024b).

1.3. Seasonal variability of mesoscale eddies of the Lofoten Basin

It is known that mesoscale eddies are observed throughout the Lofoten Basin at all times of the year. They have a significant impact on the redistribution of heat, salt, and nutrients (Faghmous et al., 2015; Belonenko et al., 2017). On the other hand, seasonal variability significantly affects their number and thermohaline characteristics, while seasonal variability of cyclones and anticyclones remains poorly understood. Over a 25-year period (from 1993 to 2017), 1079 anticyclones and 1026 cyclones were detected in the Lofoten Basin. Table 1.1 shows the seasonal variability of their main characteristics. The number of anticyclones in winter and spring is higher than the number of cyclones, while in the summer and autumn their number is close. This may indicate hydrophysical conditions that contribute to the formation of more anticyclones than cyclones. Another important feature is the fact that the average orbital velocities and amplitudes of anticyclones in the summer and autumn period are significantly higher than those of cyclones, whereas in other

seasons the difference is barely noticeable (Table 1.1). The lifespan and average radius of eddies do not have any noticeable seasonal changes.

Table 1.1. Seasonal variability of the average characteristics of cyclones (C) and anticyclones (AC) in the Lofoten Basin for the period 1993-2017

Season	Winter	Winter	Spring	Spring	Summer	Summer	Autumn	Autumn
Parameters	C	AC	C	AC	C	AC	C	AC
Number (units)	238	269	232	262	279	275	277	273
Orbital velocity (cm/s)	10.4	10.6	10.9	11.1	8.5	10.4	8.7	9.6
Amplitude (cm)	4.8	4.9	5.0	5.4	3.8	5.1	3.9	4.7
Life span (days)	26.6	24.3	26.2	27.9	27.0	30.4	27.1	27.6
Radius (km)	56.8	54.5	53.1	54.8	54.6	53.9	56.0	55.8

Figure 1.2 shows the distribution of the number of cyclones and anticyclones in the Lofoten Basin by 1° grid cells in latitude and longitude, performed for the seasons for the period 1993-2017. It can be noted that a significant number of eddies of both types are observed in the central part of the basin, as well as on the continental slope of Norway. In winter, the maximum (more than 30) number of cyclones can be traced in the eastern part of the Lofoten Basin. This can be explained by the significant baroclinic instability of the NwASC, whose velocities increase in winter by up to 20 cm/s (Jakobsen et al., 2003). On the other hand, the western and northwestern parts of the Lofoten Basin are characterized by significantly fewer eddies (less than 15 cyclones and anticyclones per season per cell). Such a significant spatial variability in the number of eddies is associated with the topography of the Lofoten Basin, as a result of which eddies breaking away from the NwASC drift into its central part (Ivanov and Korablev, 1995b, Kohl, 2007; Volkov et al., 2015). In autumn, 20-25 cyclones are observed in the area of the NwASC, while in the summer and spring their number is significantly reduced (Fig. 1.2). In the summer and

autumn period, the largest number of cyclones was found in the central part of the basin (70-71° N, 3-5° E). This feature is explained by the fact that these cyclones surround the quasi-permanent Lofoten Vortex, forming a more stable so-called "shielded vortex" when interacting with it) (Carton, 1992; Tóth and HÁzi, 2010). The number of anticyclones, largely related to the intensity of rainfall, varies significantly by season. Their greatest number is observed in the summer and autumn period, the least - in the spring period (Fig. 1.2b). An increased number of anticyclones was recorded in the summer (27 eddies per cell) and autumn (23 eddies per cell) periods in the eastern part of the basin, where the NwASC turns to the northeast. The seasonal features considered are obviously related to the properties of the Norwegian current branches, since most of the eddies are formed on topographic inhomogeneities near the Norwegian continental shelf.

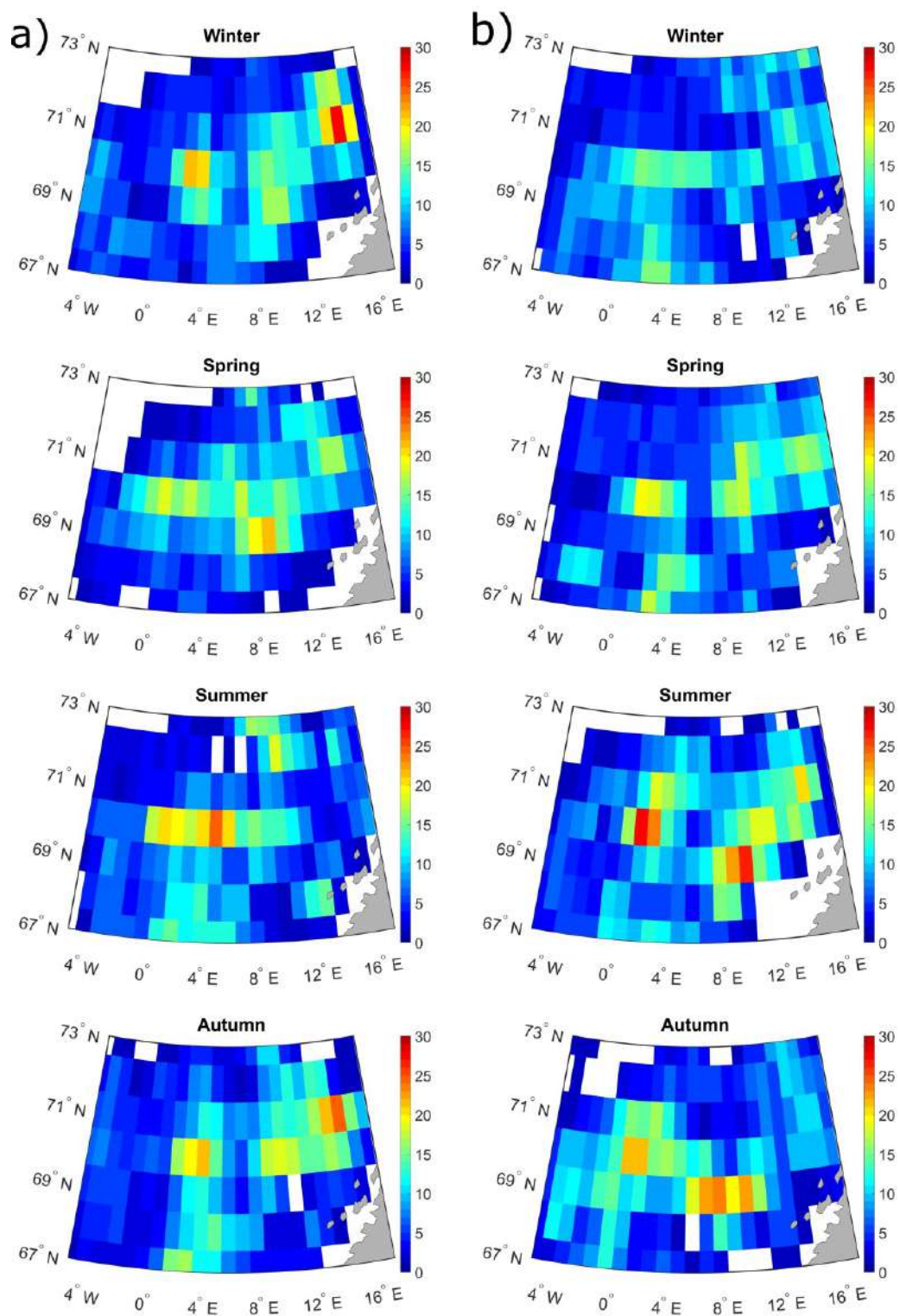


Figure. 1.2. The number of cyclones (a) and anticyclones (b) per grid cell (1° in latitude and longitude) in the Lofoten Basin by season for the period 1993-2017.

Mesoscale eddies in the Lofoten basin can manifest themselves in anomalies of thermohaline characteristics. Since eddies have a strong barotropic component, and their cores are located at a depth of 300-600 m, a horizon of 450 m was chosen

to study the seasonal variability of the spatial distribution of thermohaline characteristics (Fer et al., 2018; Zinchenko et al., 2019). Table 1.2 shows the seasonal variability of the thermohaline eddy characteristics averaged over 1993-2017 for the 450 m horizon, obtained using GLORYS12V1 data. It is noticeable that the greatest difference between cyclones and anticyclones is manifested in anomalies in water temperature, while the difference in salinity and density is small (Table 1.2). This indicates the exceptional importance of the thermal component in eddy formation. Another explanation may be related to convective processes, for which temperature plays a major role. The highest temperature values are typical for eddies in autumn, while the minimum temperature of cyclones and anticyclones is observed in winter and partly in spring, during which the process of convection actively occurs (Fedorov et al., 2019).

Table 1.2. Seasonal variability of thermohaline characteristics of cyclones (C) and anticyclones (AC) averaged over the period 1993-2017 for the 450 m horizon according to GLORYS12V1 data

Parameters	Winter	Winter	Spring	Spring	Summer	Summer	Autumn	Autumn
	C	AC	C	AC	C	AC	C	AC
Temperature (°C)	3.56	3.98	3.58	4.08	3.77	4.20	4.17	4.30
Salinity (psu)	35.06	35.07	35.05	35.08	35.06	35.08	35.08	35.09
Potential density (kg/m ³)	27.75	27.71	27.74	27.71	27.73	27.70	27.70	27.69

It is known that quasi-permanent LV is also characterized by significant seasonal fluctuations in thermohaline properties. In their work (Ivanov and Korablev, 1995a), the authors note that in the upper layer, temperature, salinity, and density change more intensively than in the lower part of the LV. Thus, the standard

deviation of temperature in the layer between the surface and the core of the eddy is significantly higher than similar values in the layer between the core and the seabed. Ivanov and Korablev (1995a) suggested that the very existence of LV is closely related to its annual thermal regeneration in winter. To analyze the seasonal variability of the eddy thermohaline structure in the area of the LV location, a transverse section was constructed along 69.8°N passing through its core center (Fig. 1.3). In winter, due to weakened density stratification, deep convection occurs in the center of the Lofoten Basin, reaching its maximum in March (Fedorov et al., 2019). Figure 1.3 shows the predominance of vertical gradients of thermohaline characteristics in the upper part of the LV. In winter, at a depth of less than 50 m, there is a surface layer of water that is colder and saltier than the underlying layers. Due to this, maximum positive anomalies of water density and, consequently, negative buoyancy are observed in the upper layer, contributing to the immersion of waters and the subsequent renewal of the LV core. Atlantic waters are observed at depths of 200-800 m in the eastern part of the Lofoten Basin, characterized by positive temperature and salinity anomalies, as well as lower potential densities compared to the underlying layers (Fig. 1.3).

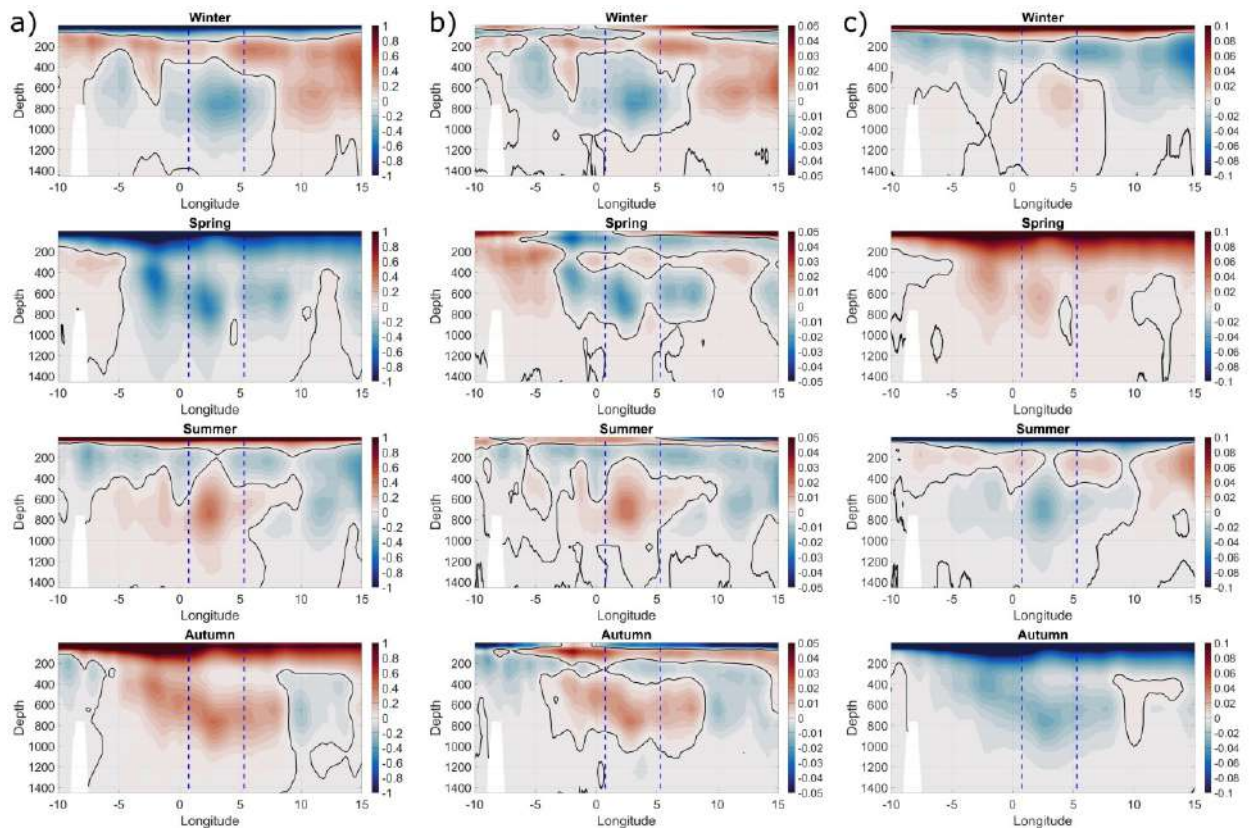


Figure. 1.3. Zonal vertical section through 69.8° N anomalies of temperature (a, $^{\circ}\text{C}$), salinity (b, psu) and potential density (c, kg/m^3) by seasons for 1993-2017. The black lines show values equal to zero. The blue lines show the location of the Lofoten Vortex.

In winter, negative anomalies of water temperature with values up to -0.5°C can be traced in the LV core. Due to the penetration of fresh water during convection, strong desalination is observed in the LV core in winter up to -0.02 psu. The presence of cold desalinated waters in the LV core in winter leads to positive density anomalies of the order of 0.025 - 0.050 kg/m^3 (Fig. 1.3). In spring, maximum thermal anomalies are observed, reaching -0.8°C in the LV core, which indicates the active development of convection during this period. Figure 1.3b shows a decrease in salinity in the region of the LV core to -0.03 psu. All this leads to the formation of positive density anomalies throughout the layer from the surface up to 1500 m. Also, the presence of similar anomalies of thermohaline characteristics near the LV at depths of 200 - 800 m confirms the existence of secondary convection foci in the

spring period with a depth of about 400-500 m, previously described by Ivanov and Korablev (1995a; 1995b). During the summer warm-up, the upper part of the LV is "cut off" from the surface by the seasonal thermocline, as a result of which the eddy acquires a characteristic lenticular shape (Fig. 1.3). In summer and autumn, the temperature in the LV core exceeds the average values by 0.6-0.9 °C, while the temperature in the surface layer up to 100 m is 1.5-2.5 °C higher than the annual average. Ultimately, this leads to the formation of a stable vertical stratification that prevents the penetration of water from the surface. During this period, positive salinity anomalies (up to 0.03 psu) are observed, however, an increase in temperature leads to negative density anomalies up to -0.06 kg/m^3 . It is worth noting that in the field of temperature and density, the deflection and exit to the surface of isotherms and isopycnae above the LV core is clearly noticeable (Fig. 1.3). In the summer and autumn period, viscous relaxation of LV occurs due to transverse eddy circulation and turbulent diffusion (Fedorov, 1983; Bloshkina and Ivanov, 2016; Fer et al., 2018).

To summarize, it can be noted that the seasonal variability of the mesoscale eddies of the Lofoten Basin manifests itself both in the seasonal change in the number of eddies and in the corresponding change in their thermohaline characteristics. The number of anticyclones in the winter-spring period is greater than the number of cyclones, whereas in the summer-autumn period the difference is insignificant. In summer and autumn, the average orbital velocity and amplitude of eddies are slightly lower for cyclones than for anticyclones. The largest number of eddies of both types was detected in the central and eastern parts of the Lofoten Basin throughout the year. In winter, the NwASC is more unstable than in other seasons. The largest number of anticyclones is observed in summer and autumn in the southeastern part of the basin, where the NwASC turns to the northeast. The results indicate that the greatest differences in the characteristics of eddies are manifested in temperature anomalies and much less in salinity and density. The largest temperature anomalies in the eddy cores are observed in winter, the smallest

in autumn. In the upper part of the eddy, thermohaline gradients are significantly higher than in the lower part of the eddy.

1.4. Quasi-permanent dipole of the Lofoten Basin

Recently, dipole (mushroom-shaped) structures have been discovered using satellite images in many areas of the Global Ocean (Hughes and Miller, 2017). Many such structures have been detected using altimetric fields in the Northwestern Pacific (Prants, 2014; Prants et al., 2014b). It is known that dynamically active areas of the Global Ocean, such as the Lofoten Basin of the Norwegian Sea, are characterized by intense eddy formation, including mushroom-shaped structures (Volkov et al., 2013; Belonenko et al., 2014; Fedorov and Belonenko, 2020; Travkin et al., 2022c). Currently, there is a large number of works devoted to mesoscale structures of the Norwegian Sea, while the vast majority of them are devoted specifically to monopole eddy structures (Fer et al., 2018; Raj et al., 2016; Travkin and Belonenko, 2019; Sandalyuk et al., 2020; Sandalyuk and Belonenko, 2021). Despite this, little attention has been paid to another type of mesoscale variability in the oceans, mushroom currents (Ginzburg and Fedorov, 1984b). Using numerical experiments, the authors of Manucharyan and Timmermans (2013) found that dipoles can be generated in the Lofoten Basin. Although most of the formed dipoles recirculated back to the front due to the curved trajectories of their movement and the increase in the width of the front, in some cases the dipoles could move away from the generation site for quite a long time. It is known that in the Lofoten Basin, dipoles can be generated both in the LV region and in the frontal zones of the main currents (Belonenko et al., 2021b). Analyzing mushroom-shaped dipoles in the visible, infrared, and radio ranges, Ginzburg and Fedorov (1984b) suggested that dipoles can form when a narrowly localized jet stream slows down under the influence of viscous drag or a locally applied pulse. Thus, they correlated the mushroom-shaped dipoles with the "thin upper layer of the ocean." This work demonstrates that dipoles can exist not only on the surface, but also in the underlying layers of the Global Ocean.

A significant number of long-lived mushroom-shaped dipoles are formed in the Lofoten Basin of the Norwegian Sea, but they have not yet been studied in detail. Thus, the purpose of this part of the study is to identify and describe in detail the structure and evolution of the mushroom dipole in the Lofoten Basin. We want to give a detailed description of this phenomenon, including studying possible mechanisms of dipole formation. To achieve this goal, Lagrangian maps are used to identify the structure at selected horizons and trace its subsequent evolution in detail.

Previous studies of dipole structures

Dipole structures are characterized by the presence of closed current lines located around the centers of both monopolar vortices and the dipole itself (Stern, 1975). The existence of dipoles in the Global Ocean was theoretically confirmed by analyzing the solution of the barotropic equation of a potential vortex in the quasi-geostrophic approximation. In these studies, dipole structures are sometimes referred to as two-dimensional isolated Rossby waves, the existence of which is associated with the combined effect of nonlinearity and the beta effect (Larichev and Reznik, 1976). The term "modon" was introduced to denote a special case of a barotropic dipole on the beta plane (Stern, 1975; Larichev and Reznik, 1976). Currently, this term is used for a more general case: a barotropic or baroclinic pair of vortices on an f - or β -plane and a rotating sphere (Khvoles et al., 2007). It is established that in modes the Rossby number $Ro = |\zeta/f|$ (ζ is the relative vorticity, f is the Coriolis parameter) It is 0.1-0.3, and the orbital velocity is 10-20 cm/s. Although the vertical scale of the modon is very difficult to determine, they have a Burger number $Bu_E \approx 0.015-0.070$ (Lahaye et al., 2020). The dimensionless Burger number $Bu_E = \left(\frac{NH}{\Omega L}\right)^2 = \left(\frac{Ro}{Fr}\right)^2 = \left(\frac{R_d}{L}\right)^2$ shows the relationship between the vertical density stratification and horizontal rotation of the Earth. Here, N is the Weisel-Brent frequency, Ω is the angular velocity of the Earth's rotation, H is the depth, Ro is the Rossby number, Fr is the Froude number, R_d is the Rossby deformation radius, and L is the characteristic scale of the flow. The values of $Bu_E \ll 1$ indicate that

stratification plays a lesser role than rotation for vertical and horizontal movements in a liquid (Cushman-Roisin, 1994). Often, after the destruction of the modon, the eddies can exist independently of each other as separate structures. In this case, the velocity of propagation of monopolar eddies is significantly less than the initial velocity of the modon, but still higher than the velocity of the Rossby waves. In addition, these monopole eddies can move in an easterly direction like a modon before it breaks up.

The variability of water temperature on the surface of the modon can be traced throughout its existence. Temperature anomalies can be interpreted as a combination of eddy advection with mixing with the temperature of background waters (Hughes and Miller, 2017). After the destruction of the modon, the temperature anomalies decrease, but remain noticeable for up to several months. Both classical and modern theories describing modons are barotropic and consider temperature as a passive tracer that either moves along with the modon along its trajectory or dissipates due to small-scale instability of the convective type, thereby affecting its stability (Lahaye et al., 2020). On a sphere or β -plane, stable propagation of modons is possible only in the zonal direction, since movement in the meridional direction leads to a change in planetary vorticity (Hughes and Miller, 2017).

Detecting a dipole in the ocean using altimetry or field measurements is a difficult task, since the process of formation and evolution of dipoles has limited predictability and occurs in a short period of time. Due to this, there are very few actual observations of dipoles in the oceans. Hughes and Miller (2017) described 9 modons in the middle latitudes, 5 of which formed on the continental slope and moved eastward, and 4 formed in the open ocean and moved west and southwest. The authors propose two mechanisms for the formation of a dipole: the formation of a dipole as a result of the fusion of two monopolar eddies of different polarities (cyclone and anticyclone) and the mixing of an outer ring of vorticity around an eddy of opposite polarity with a neighboring region, turning a monopolar eddy into a dipole. The formation of eddy structures may also be associated with a special flow regime, the mechanisms of generation of which were not previously known and

deserve detailed study. Similar currents were detected on satellite images and were called "mushroom-shaped" currents (Ginzburg and Fedorov, 1984b). A "mushroom jet" is an unstable and narrow jet that ends in two eddies of different polarities combined into a single structure. In other words, the combination of a narrow jet and a pair of eddies of the opposite sign is a dipole resembling a mushroom in cross-section. In this work, such structures are referred to as "mushroom-shaped dipoles". Figure 1.4 shows the structure of a mushroom-shaped dipole - the jet (the so-called "stem") of the dipole plays an important role in its formation, ending in two eddies of different polarities (the so-called "cap"). Natural tracers, such as plankton or drifting ice, help to detect mushroom-like structures in the optical and infrared ranges (Ginzburg and Fedorov, 1984b). The size of mushroom-shaped dipoles can vary in a wide range from 12 to 160 km (Ginzburg and Fedorov, 1984b).

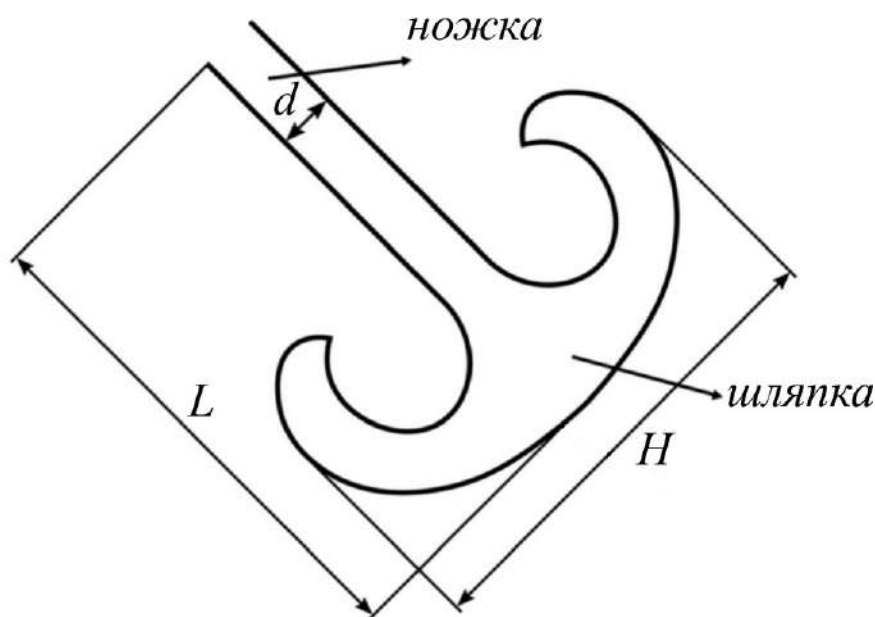


Figure. 1.4. The structure of the mushroom-shaped dipole: L is the length, H is the width of the "cap" and d is the width of the "stem" (according to Ginzburg and Fedorov, 1984b).

The shape of the "cap" of the dipole can be practically symmetrical or somewhat distorted, up to the presence of only one of its parts (for example, the

presence of only an anticyclone). Reflecting on the mechanism of formation of mushroom-shaped structures, Ginzburg and Fedorov (1984b) suggested that the formation of a dipole may be due to the influence of an intense local impulse on the flow in the surface layer of the ocean. Such an impulse can occur, for example, due to localized wind flow, pressure gradients at sea level, as well as instability of fronts and currents. In offshore and coastal areas, a dipole can be formed under the influence of river runoff and wind, due to the influence of topography, the general direction of coastal water circulation, or water exchange through straits associated with tidal or surge events (Ginzburg and Fedorov, 1984b). The asymmetry of eddies in a dipole is related to the degree of predominance of local angular momentum introduced from the outside (Stern, 1975). The properties of dipoles also depend on the shape of the basin and the interaction with other eddy structures. Thus, the loss of one of the eddies in the dipole can be compensated by the inclusion of an eddy of similar polarity in the dipole from the outside. The strengthening of the dipole when interacting with eddies of different polarities, as well as the weakening during the convergence of eddies of the same polarity, can change the initial trajectories of dipole structures. Dipoles can also form so-called "packages" of several structures, in addition, an eddy in the dipole can lead to the appearance of a new independent dipole. The evolution of the dipole leads to a slow elongation of each vortex, which is accompanied by a decrease in relative velocities to zero (Stern, 1975; Carton, 2001).

A series of Voropaev's works is devoted to experimental laboratory studies of mushroom-shaped dipoles, a summary of which can be found in the monograph (Voropaev and Afanasyev, 1994a), which discusses possible physical mechanisms of mushroom-shaped dipoles formation. The process of formation and subsequent evolution of mushroom-shaped structures over time can be divided into two parts: the initial ($t < T_N$) and the final one ($t > T_N$), where t is a time, T_N is the period of the first stage of the experiment. At the initial stage, the source generates an intense stream of current forming a vorticity front. In this case, immediately after switching on the pulse source, the pressure field is redistributed, which induces a dipole flow

in the entire volume of the surrounding liquid. Although the jet stream is turbulent, the vorticity in the frontal region has mainly an azimuthal component. At a moment in time $t < T_N$ vertical density stratification has little effect on the flow, and the vorticity front propagates at a speed about two times lower than the velocity of the liquid behind the front (Stern and Voropaev, 1984). As a result, the liquid behind the front enters the frontal region, transferring momentum, vorticity and mass due to mixing with the surrounding waters. If the source has been active for a long enough time, then at the time $t \approx T_N$ a three-dimensional jet stream is formed with an attached vorticity front. In these experiments, the characteristic values are T_N equal to hours. If a short period of time is selected $T_0 < T_N$, then all the vorticity and momentum will be concentrated in a localized three-dimensional region at a moment in time $t \approx T_0$ (Voropaev and Afanasyev, 1994a; 1994b). Thus, at the end of the initial stage $t \approx T_N$ in both cases ($T_0 \geq T_N$ and $T_0 < T_N$) a compact eddy region is formed and grows (due to the involvement of the surrounding fluid). This area can be localized ($T_0 < T_N$) or attached to the stream. For a long period of time $t > T_N$, the frontal area is stratified. Gravity affects the vertical component of velocity, as a result of which the capture of the surrounding liquid through the upper and lower surfaces becomes impossible. A further increase in the frontal region occurs mainly due to lateral involvement, and over time it turns into a flat mushroom-shaped dipole with two characteristic asymmetric spirals. Thus, despite the fact that external parameters determine all the characteristics of mushroom-shaped dipoles, in the absence of an external velocity shift, the length, width of the "cap", the thickness of the jet and their specific values do not affect the formation of dipole structures. Although there is no detailed understanding of how the vorticity component transforms into a predominantly vertical vorticity characteristic of dipole structures, it becomes clear from the above analysis that when a compact eddy region with a horizontal pulse is formed, stratification transforms it into a mushroom-shaped dipole after a while (Flor et al., 1995; Johan and Fang, 1997). Despite the fact that the characteristic time periods T_N and T_0 in the experiments are equal to hours, the

authors claim that this theory is applicable to the conditions of the Global Ocean (Voropaev et al., 1991).

The theoretical justification of these experiments is based on the assumption that all the vorticity in the mushroom-shaped dipole is concentrated in its "cap", and the flow outside the "cap" is potential. In the polar coordinate system (r, θ) centered in the "cap" of the dipole, the translational velocity of movement in the direction of $\theta = 0$ is $\bar{U} = \frac{d\bar{x}}{dt}$, where \bar{x} is displacement of the "cap" of the mushroom dipole. Here (x, y) are Cartesian coordinates - $x = r\cos\theta, y = r\sin\theta$. External Ψ_1 and internal Ψ_2 stream functions can be represented as (Voropaev and Afanasyev, 1994a; 1994b):

$$\begin{aligned}\Psi_1 &= -\bar{U}(r-R^2/r)\sin\theta, & r > R, \\ \Psi_2 &= -\frac{2\bar{U}J_1(ar/R)}{aJ_0(a)}\bar{U}\sin\theta, & r < R,\end{aligned}$$

where J_0, J_1 are the Bessel functions, $a = 3.83$ is the first zero J_1 , $R(t)$ this is the radius of the "cap", which increases with time. ($2R = H$). Stream function Ψ_1 describes the potential current around the "cap", a stream function Ψ_2 describes flow in the Lamb-Chaplygin dipole with a vorticity distribution $\omega = \frac{a}{R^2}\Psi_1$. It is possible to derive the equation of motion of the particles of a mushroom-shaped dipole in a normalized coordinate system $(\eta = r/R(t), \theta)$ (Voropaev and Afanasyev, 1994a; 1994b):

$$\begin{aligned}\frac{d\eta}{dt} &= -\frac{2}{3\alpha t} \left[\frac{\alpha}{2}\eta + \left(1 - \frac{1}{\eta^2}\right)\cos\theta \right], \text{ when } \eta > 1 \\ \frac{d\theta}{dt} &= \frac{2}{3\alpha t\eta} \left(1 + \frac{1}{\eta^2}\right)\sin\theta\end{aligned}$$

and

$$\begin{aligned}\frac{d\eta}{dt} &= -\frac{2}{3\alpha t} \left[\frac{\alpha}{2}\eta + \left(1 - \frac{2J_1}{J_0(a)\eta}\right)\cos\theta \right], \text{ when } \eta < 1 \\ \frac{d\theta}{dt} &= \frac{2}{3\alpha t\eta} \frac{2J_1}{J_0(a)\eta}\sin\theta\end{aligned}$$

where α is a constant. When $\eta = 1$, the coordinates are not defined, because with this value, the second derivatives in the current function have a discontinuity. The above system of equations describes the dynamics of particles in a mushroom-shaped dipole.

Results

In 2013-2016, 48 mushroom-shaped dipoles with a life span of 19 to 45 days were found in the study area. It should be noted that dipoles are often recorded in the area of the LV location and in the eastern part of the Lofoten Basin, which is also characterized by increased values of average and EKE, as well as SSH (Volkov et al., 2013; Belonenko et al., 2014; Travkin and Belonenko, 2021). Since the vertical scale of mesoscale eddies in the Lofoten basin is approximately 1000 m, we applied the Lagrangian method for the horizon of 541 m, which is the center of the eddy cores (Sandalyuk et al., 2020). Mushroom-shaped dipoles were examined both on the surface and at a depth of 541 m.

Lagrangian maps

The main focus is on the quasi-permanent mushroom-shaped dipole located in the eastern part of the Lofoten Basin. This dipole was identified on most Lagrangian maps for 2013-2016, regardless of the season.

Figure 1.5 shows the Lagrangian S- and Λ -maps for October 20, 2013. The color on the S-map indicates the distance traveled by the Lagrangian particles 15 days before the observation date. Figure 1.5 shows a mushroom-shaped dipole at a depth of 541 m in the region of 69.2° N, 10.0° E, pointing to the southeast. The dipole jet, which splits into two parts, forms the "cap" of the dipole. The "cap" is formed precisely from the jet (stem), as a result of which both multidirectional eddies are surrounded by an arc-shaped jet of another stream. The vectors of currents directed to the southeast are also found on this horizon and on the Λ -map (Fig. 1.5b).

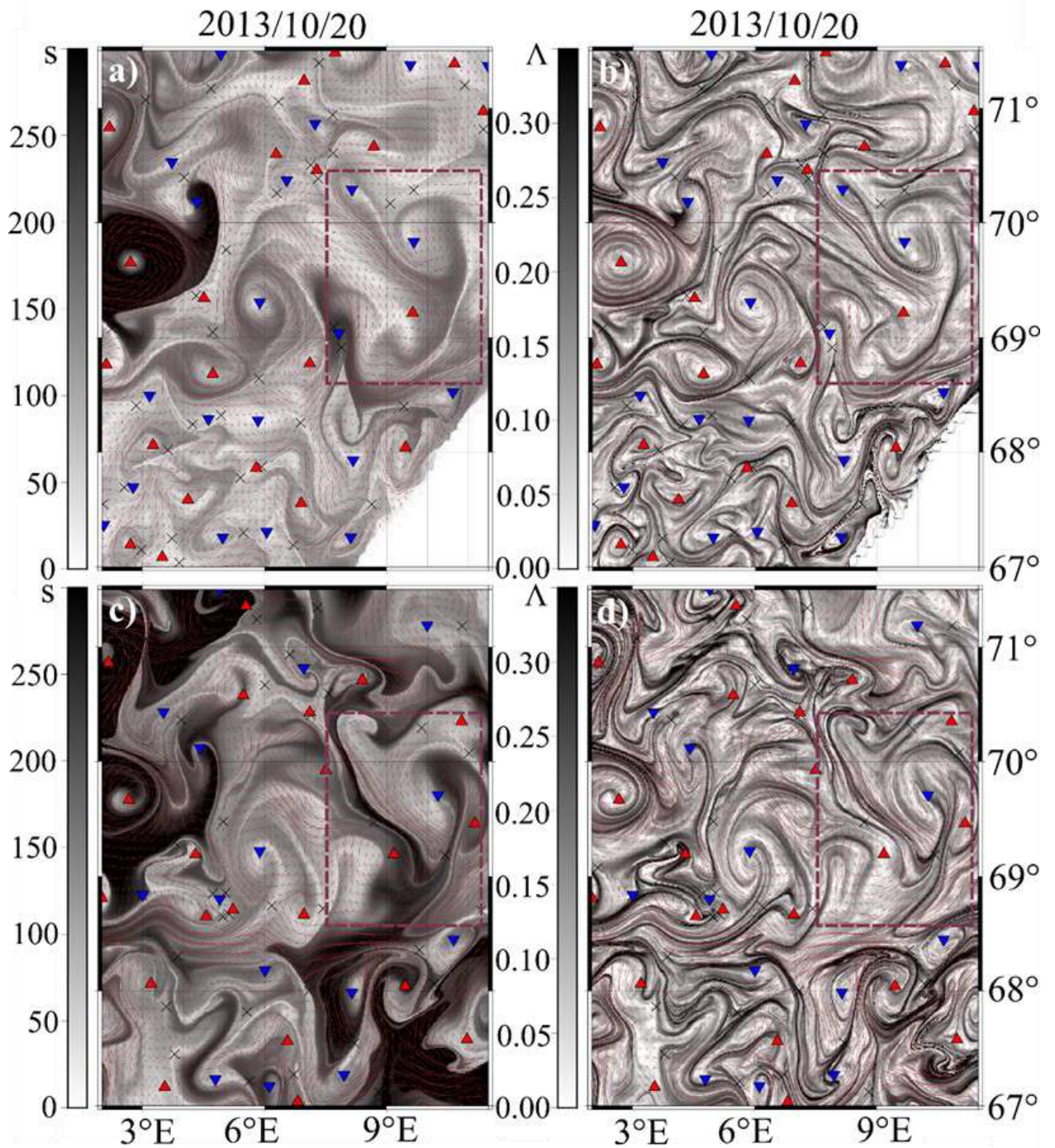


Figure. 1.5. Lagrangian maps of the study area for October 20, 2013: a) S- and b) Λ -maps for 541 m; c) S- and d) Λ -maps for the sea surface. Elliptical points connected to the centers of anticyclones and cyclones are shown with upward (red) and downward (blue) triangles, hyperbolic points are marked with crosses. The values on the S-maps are given in km, the values on the Λ -maps are given in 1/day.

The black curves (ridges) in Figures 1.5b and 1.5d correspond to "attractive Lagrangian coherent structures", which approximately show the location of the so-called unstable manifolds of the largest hyperbolic points of the region, indicated by crosses (see Prants et al., 2017). The ridges between the cyclone and the anticyclone of the dipole both on the surface and at a depth of 541 m are associated with hyperbolic points north of the dipole. They exist for quite a long period of time, which confirms the existence of a quasi-permanent dipole in this region. The role of such ridges between eddies is twofold. On the one hand, they outline the core of jet streams forming a dipole. They also outline the frontal axis between oppositely directed jet streams (Fig. 1.5). On the other hand, the ridges are peculiar "barriers" that facilitate the transfer of particles along them and significantly complicate them across.

In the centers of the vortices of the "cap", the values on the S-map reach 50 km, while in its front part the values are close to 220 km. This means that the velocities in different parts of the dipole can vary by more than 4 times. On average, the width of the "cap" of the dipole (H) is 170 km, the length (L) is 150 km, and the width of the jet (d) is about 40-60 km. This indicates that the size of the mushroom dipole elements significantly exceeds the local values of the Rossby baroclinic deformation radius (R_d), equal to 6-8 km and determined by the formula $R_d = \frac{NH}{n\pi f}$,

where $N = \sqrt{-\left(\frac{g}{\rho} \cdot \frac{\partial \rho}{\partial z}\right)}$ – Brunt–Väisälä frequency, H – depth, n – number of the baroclinic mode, $f = 2\Omega \sin\varphi$ – the Coriolis parameter, Ω – the angular velocity of the Earth's rotation around its axis (Novoselova et al., 2020). Thus, the Burger number of the analyzed dipole is ($Bu = \frac{R_d^2}{L^2}$) equal to 0,0016-0,0028. Comparing the discovered mushroom-shaped dipole with similar structures observed using satellite images, it can be noted that the dipole in the Lofoten Basin exceeds previously discovered structures in areas south of Iceland, east of Kamchatka, in the eastern part of the Black Sea, as well as in the Baltic and Japanese Seas (Ginzburg and Fedorov, 1984b). Most likely, the mechanism of formation of dipoles in the Lofoten

Basin is due to the combined influence of dynamic causes and topography. It is worth noting that the mushroom dipole is formed on the slope of a topographic depression, whereas the mushroom dipole jet is directed along an isobath of 3000 m perpendicular to the continental slope. This area is called the "Lofoten ledge" and is characterized by increased values of topography gradients: ≈ 2000 m per 30 km. It is in this place that the "cap" of the dipole is formed. The jet, as if "hitting" the continental slope, forms eddies of different polarities. However, on the surface, where the influence of topography is not so significant, the dipole structure is also present, although not so clearly (Fig. 1.5c, d). Another confirmation of the topographic nature of the analyzed mushroom-shaped dipole is the specific features of the selected area (Fig. 1.6-1.9).

The mean currents

In the field of average current velocities for 2011-2019, the mushroom-shaped dipole is clearly visible both on the surface and at a depth of 541 m (Fig. 1.6). The dipole jet is oriented to the southeast along the isobath of 3000 m and the areas of both positive and negative local extremes of the height of the sea surface correspond to the location of the dipole vortices. It is worth noting that on the map of surface averaged current velocities, the area of cyclonic vorticity on the left side of the dipole is more clearly visible, whereas on the horizon of 541 m, the right (anticyclonic) area of the dipole is more clearly visible (Fig. 1.6). A comparison of Figures 1.5 and 1.6 demonstrates that the mushroom-shaped dipole at a depth of 541 m is more developed than on the sea surface, where the current lines in the area of the "cap" are not closed. Since the dipole vortices are visible on the averaged velocity maps, this means that the observed mushroom-shaped structure is quite stable.

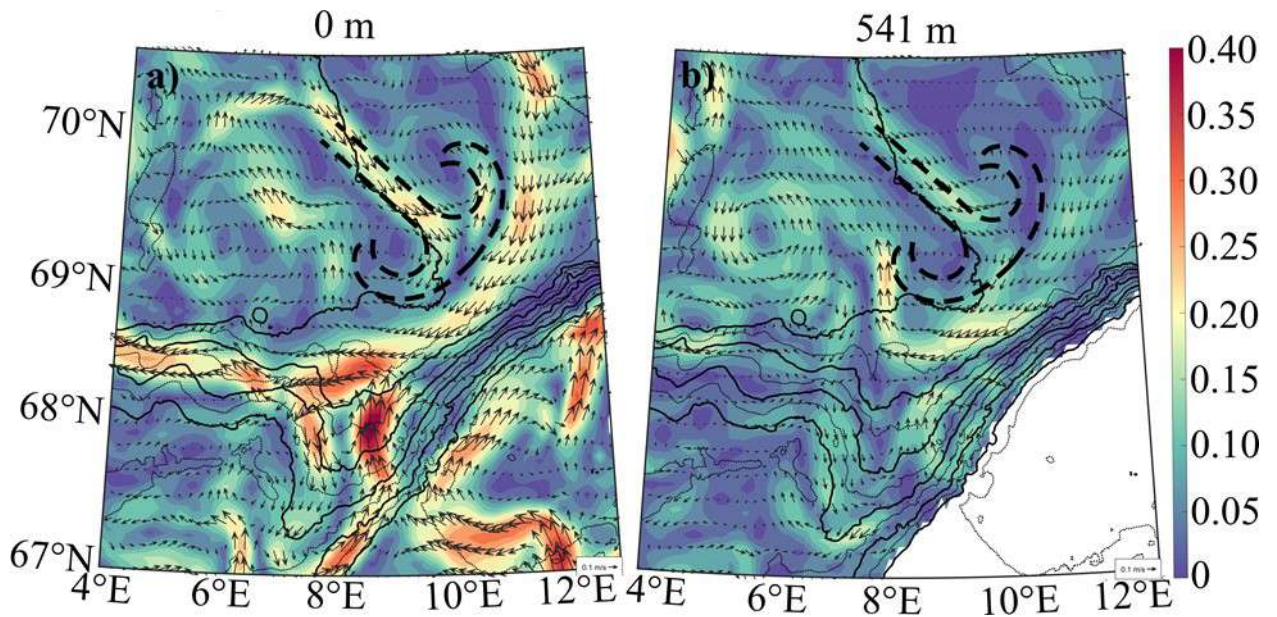


Figure. 1.6. The average current velocities (m/s) for 2011-2019 at the surface (a) and at a depth of 541 m (b).

The analysis of S- and Λ -maps for 2013-2016 demonstrates that they form quite frequently in the eastern part of the Lofoten Basin and show relative stability. So, on October 30, 2013, the studied dipole dissipated, but two weeks later a new dipole with approximately the same properties appeared in its place. The main characteristics of the dipole analyzed on the basis of Lagrangian maps are described below:

(1) Life expectancy—the mushroom-shaped dipole on the horizon of 541 m appeared on October 4, 2013 and was fairly stable from October 10 to October 30. On October 30, its rapid disintegration began.

(2) Horizontal displacement—a slight displacement of the cyclone center of the mushroom dipole was detected. Thus, the cyclone shifted eastward by about 38 km in 14 days (from October 10 to October 24, 2013). The speed of movement of the cyclone is 1.65 km/day (~ 2 cm/s).

(3) The distance between the centers of the eddies is that the anticyclone located to the south is localized and practically does not change its position. Coupled with the eastward movement of the cyclone, this leads to a slight shift of the mushroom dipole in a southerly direction. The distance between the centers of the

eddies increases from 77 to 94 km. The rate of this increase is insignificant and amounts to 0.7 km/day (0.8 cm/s).

(4) The size of the cyclone and the anticyclone of the dipole —from October 12 to October 24, 2013, a gradual increase in the scale of eddies was observed. Thus, the cyclone increased by about 18 km (from 37 to 55 km), and the anticyclone by 9 km (from 28 to 37 km).

Temperature, relative vorticity, and current function

Relative vorticity was calculated on the sea surface and horizon of 541 m: $\zeta = \frac{\partial v}{\partial x} - \frac{\partial u}{\partial y}$, normalized to the Coriolis parameter f ($f = 1.666 \cdot 10^{-4} \text{s}^{-1}$). In Figure 1.8, it is noticeable that the dipole is clearly visible on both horizons. The dipole jet is represented as a shear flow, whereas the dipole eddies are shown by eddies of different signs. Another component of the dipole is the "cap", which "closes" the dipole structure. This "cap" has a positive vorticity and also manifests itself as a jet almost perpendicular to the main jet of the dipole. Figure 1.7 also shows that the Rossby number $Ro = \frac{\zeta}{f} < 1$, this confirms the applicability of the quasi-geostrophic theory to the mushroom dipole.

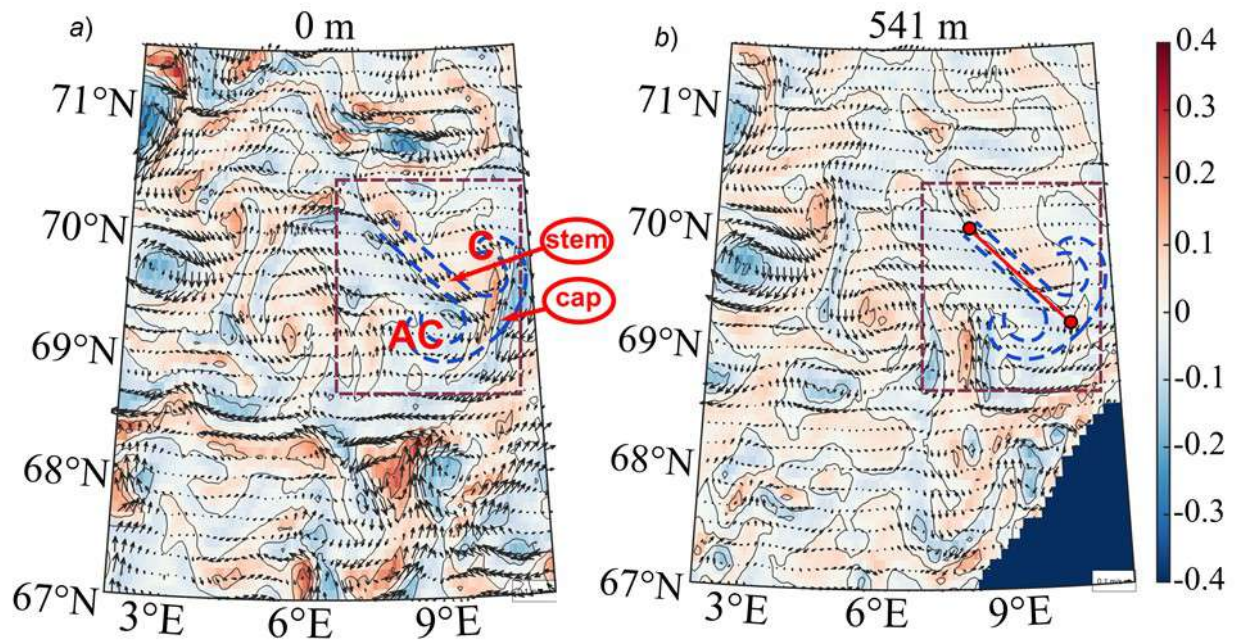


Figure 1.7. ζ/f : relative vorticity normalized to the Coriolis parameter f on the surface (a) and horizon of 541 m (b). The area of the mushroom-shaped dipole is marked with a red rectangle. AC and C denote an anticyclone and a dipole cyclone, respectively. The position of the cap and stem of the dipole are marked with red arrows. The red line along the dipole shows the area of the vertical profile for temperature and current velocity (Fig. 1.10).

The analyzed dipole is also clearly manifested in the field of the stream function. In Figure 1.8, it is noticeable that the isolines of the current function display both the "stem" and the "cap" of the dipole. The seawater density and stream function were calculated using the TEOS-10 thermodynamic equation and Cunningham's method (Cunningham, 2000; IOC, SCOR and IAPSO, 2010). The stream function makes it possible to identify a mushroom-shaped structure in the area under consideration, and the $1.25 \text{ m}^2\text{s}^{-1}$ isoline clearly outlines the shape of the dipole. Figure 1.8a clearly shows that in the area of the dipole jet, the values of the stream function are higher than -0.9, whereas in the "cap" of the dipole, the values range from -1.35 to -1. The maximum values of the stream function are observed in the cyclonic part of the dipole (Fig. 1.8a). From Figure 1.8b, it is clearly noticeable that the dipole is characterized by negative temperature anomalies with a local minimum

in the center of the cyclone (up to $-1.25\text{ }^{\circ}\text{C}$). While minor negative anomalies (less than $-0.5\text{ }^{\circ}\text{C}$ modulo) were recorded in the area of the anticyclonic eddy. The greatest positive temperature anomalies were found in the area of the dipole jet (more than $0.5\text{ }^{\circ}\text{C}$).

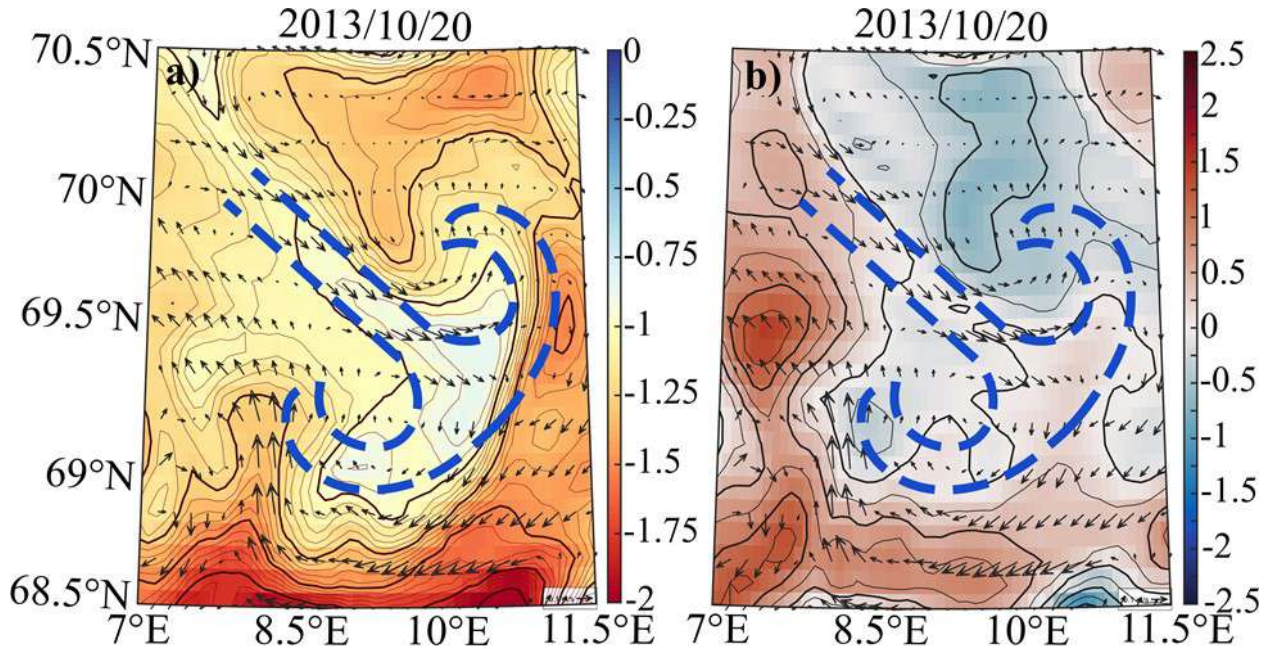


Figure 1.8. a) stream function (isolines are drawn every $0.05\text{ m}^2\text{s}^{-1}$); b) water temperature anomalies ($^{\circ}\text{C}$, isolines are drawn every $0.25\text{ }^{\circ}\text{C}$) at the horizon of 541 m.

Sea surface height and current velocity

The mushroom-like structure that appears on Lagrangian maps, stream function maps, and water temperature maps is also clearly visible in the values of sea surface height and current velocities. Figure 1.9 shows how the dipole jet follows an isobath of -0.55 m , while dividing the dipole into two parts – the region of the local maximum (up to -0.50 m) in the core of the anticyclonic eddy and the region of the local minimum in the area of the cyclone core (values less than -0.625 m). Subsequently, the dipole shows an increase in the SSH to a maximum value (about -0.45 m) in the core of the anticyclone, while the values in the cyclone change slightly. The area of the dipole jet is characterized by increased flow velocities (more than 0.15 m/s), whereas values from 0.05 to 0.10 m/s are observed in the "cap" of

the dipole with minimal values in the centers of multidirectional eddies. In the future, the region of maximum values shifts to the east, which corresponds to the direction of propagation of the dipole.

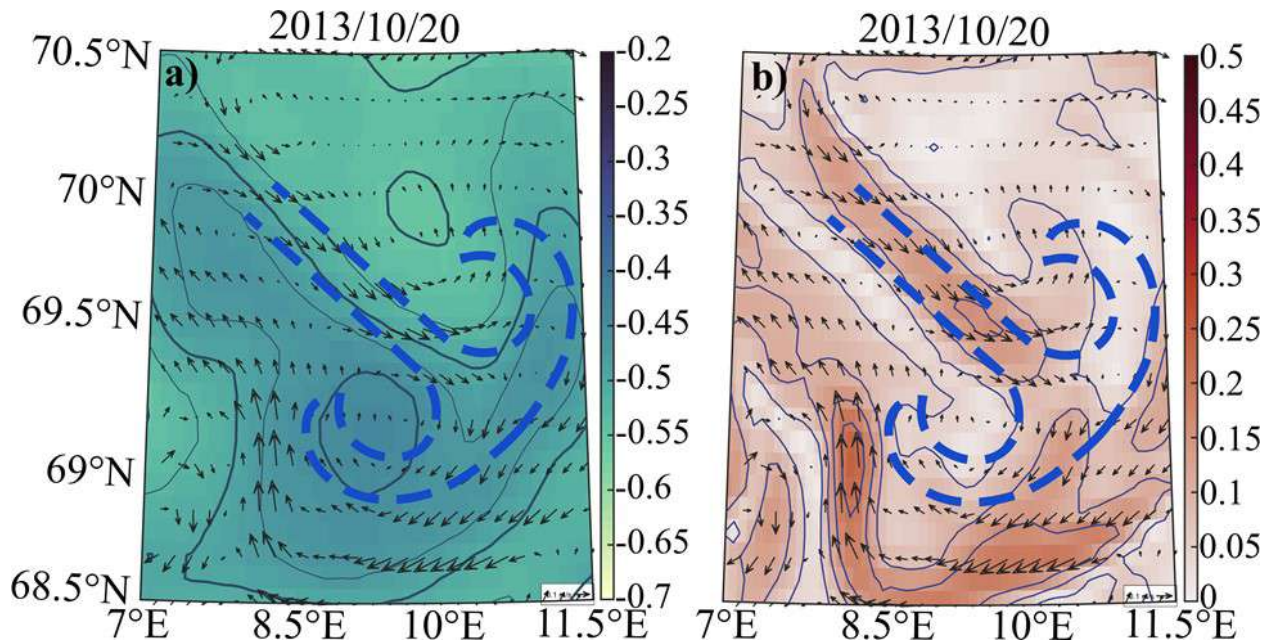


Figure. 1.9. a) the sea surface height (m, isolines are drawn every 0.1 m); b) current velocities (m/s, isolines are drawn every 0.1 m/s) at the horizon of 541 m.

Vertical dipole structure

The vertical structure of the mushroom-shaped dipole is manifested both in temperature anomalies and in current velocities. This can be traced in the layer from 0 to 800 m by anomalies in water temperature, and the dynamic signal of the dipole can be traced to the very bottom (Fig. 1.10). Thus, significant azimuthal flow velocities up to 1200 m are observed in the central part of the dipole jet (Fig. 1.10b). It can be noted that the temperature anomalies are negative in the 200-400 m layer along the mushroom dipole (Fig. 1.10). In the 400-600 m layer, negative values were observed in the "stem" of the dipole, while in the area of its "cap" (from 9.7° E to 10.5° E) the values are positive. Maximum velocities (up to 0.225 m/s) are observed in the front part of the dipole at a depth of 0-250 m, and the values decrease sharply towards its boundary. Below 600 m, the current velocity does not exceed 0.10 m/s (Fig. 1.10b).

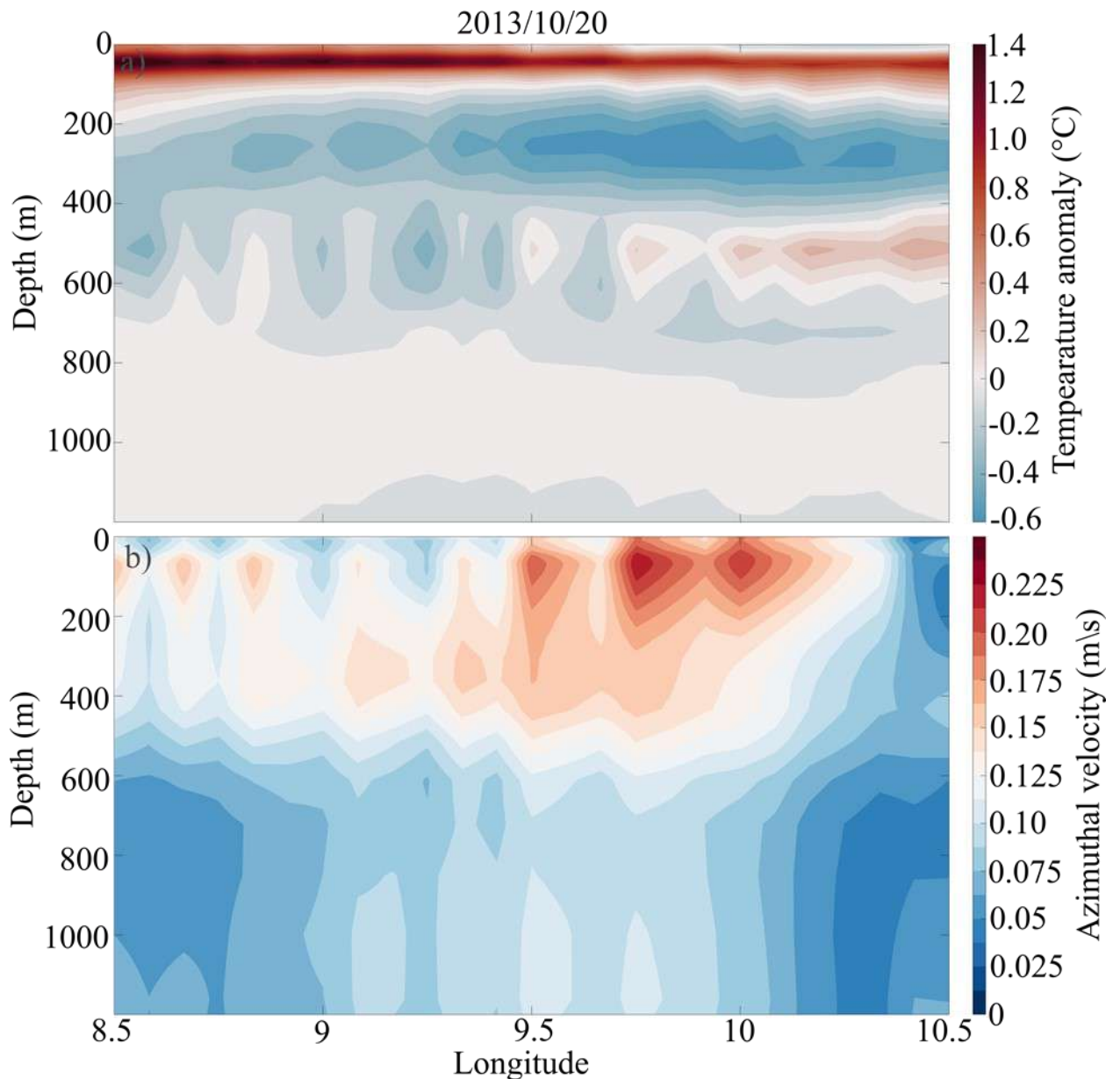


Figure 1.10. Vertical profiles through a mushroom-shaped dipole (see Figure 1.7): anomalies of water temperature (a, °C), azimuthal current velocity (b, m/s).

Discussion and conclusions

The Lofoten Basin is a dynamically active region with favorable conditions for the formation of mesoscale eddies. At the same time, monopole structures are considered in most works on Lofoten eddies, so the study of dipoles in this area is unique (Bosse et al., 2019; Travkin and Belonenko, 2019; Sandalyuk et al., 2020; Sandalyuk and Belonenko, 2021). From 2013 to 2016, 48 mushroom-shaped dipoles with a life span of 19 to 45 days were found. The evolution of one of them was

described in detail, and the appearance of the studied dipole is characteristic of the region under consideration (Fig. 1.5). Since there is little information about the dynamics of this type of mesoscale eddies, we have collected the most informative material on this topic from literary sources. This applies both to two theories about the generation and evolution of dipoles, as well as to model experiments and field observations (Stern, 1975; Larichev and Reznik, 1976; Voropaev and Afanasyev, 1994a; 1994b; Hughes and Miller, 2017; Lahaye et al., 2020).

For a detailed analysis, a mushroom-shaped dipole was selected in the eastern part of the Lofoten Basin, which existed for more than 3 weeks – from October 4 to November 5, 2013. It cannot be said that this dipole appeared simultaneously. The formation of this dipole is explained by topographic factors, and its distinctive features (cap and stem) were formed gradually. At this point, the dipole appears periodically (about once a season) and there is a fairly long period of time (about 45 days). During this period, the mushroom dipole goes through the main phases of existence: appearance, evolution and destruction. Lagrangian maps were analyzed, which make it possible to clearly describe the structure of the dipole. The width of the "cap" of the mushroom dipole is 170 km, its length is 150 km, and the width of the jet (stem) is 40-60 km. Like most mesoscale structures, this mushroom-shaped dipole has a limited period of existence and gradually disappears by the beginning of November 2013. However, we are inclined to believe that this dipole is quasi-permanent, since it constantly appears on the map of averaged current velocities for 2013-2016.

A comparison of Lagrangian maps for the surface and the horizon of 541 m showed that mushroom-shaped structures can have a barotropic component. Indeed, the Burger number values of 0.0016-0.0028 were obtained, which is an order of magnitude lower than the values obtained in the work of Lahaye et al. (2020). Perhaps this is due to the fact that in our work we consider a mushroom-shaped dipole. Such small values of the Burger number indicate that stratification affects the formation and evolution of the mushroom dipole to a lesser extent than other hydrodynamic factors determining its development. Despite the fact that the dipole

has a clear structure with a cap and a leg, they undergo minor changes on the surface: the anticyclone is less developed there, and the current lines in the front of the "cap" are not closed. Perhaps this is due to the fact that the formation of a dipole begins in the intermediate layer when the flow rests against the continental slope. The dipole under study is represented by a narrow elongated jet with a high velocity (more than 0.15 m/s) and a cap consisting of two multidirectional vortices with azimuthal velocities from 0.05 to 0.10 m/s. During the evolution of the mushroom dipole, its size changed: from October 12 to October 24, 2013, it increased, and after October 24, it decreased. The increase in vortex radii during this period was approximately 18 km (from 37 to 55 km) for the cyclone and 9 km (from 28 to 37 km) for the anticyclone.

It has been established that mushroom-shaped dipoles can form in the ocean without the involvement of wind, since they can be traced in the fields of average current velocities. We also assume that mushroom-shaped dipoles have a topographic nature in the Lofoten Basin, since they are mainly formed in areas of significant topography changes. So, the gradient of the topography is significant and is equal to $\frac{\partial H}{\partial l} = 2,5 \cdot 10^{-2}$, where l is perpendicular to the slope isobath and H is the depth.

Perhaps the mechanism of formation of such dipoles is related to the fact that the mushroom-shaped dipole rests against the wall of the Lofoten Basin. Thus, a barotropic or baroclinic flow encounters an obstacle in the form of a slope of the seabed and splits into two parts in the slope area, forming two multidirectional eddies. These eddies form a dipole bounded in front by the current spreading along the slope. Vertically, the dipole can be traced from 0 to 800 m by anomalies in water temperature and to the very bottom by current velocities. The vertical distribution of the current velocity in the dipole differs from the estimates obtained for the LV core (Bashmachnikov et al., 2017b; Fer et al., 2018). The velocities of the mushroom dipole are maximum in the jet and minimum in the front of the cap.

To summarize, in addition to monopole eddies, dipole structures also represent significant examples of mesoscale eddy dynamics of the Global Ocean and deserve close study. It can also be noted that the analysis of Lagrangian maps, coupled with traditional methods of studying oceanological fields, is a promising method for studying mushroom-shaped structures.

1.5 Kinetic and potential energy of mesoscale eddies of the Norwegian Sea

The energy in the world's oceans is divided into Mean and Eddy Kinetic Energy (MKE and EKE, respectively), as well as Mean and Available Potential Energy (MPE and APE, respectively). It is known that APE denotes the difference between the total potential energy of a liquid at a given time and the potential energy of a liquid of similar mass if it existed in the same basin after the transition to a stable reference state in which the isosteric and isobaric surfaces are located at the same level (Reid et al., 1981).

Thus, APE represents that part of the potential energy of the system that is capable of being converted into kinetic energy by reversible adiabatic processes. The kinetic energy of the Global Ocean is traditionally divided into MKE and EKE. As a rule, EKE is used to study the temporal and spatial mesoscale variability of the World Ocean (Kang and Curchitser, 2017; White and Heywood, 1995; Novoselova et al., 2024).

In the Lofoten Basin, there is an active transition from one type of energy to another (Zhmur et al., 2023). Thus, the operation of the buoyancy force contributes to an increase in the APE of large-scale circulation. In turn, APE can generate mesoscale eddies and thus increase Eddy Kinetic Energy (Gill et al., 1974). Ultimately, in dynamically active regions and in areas of large-scale flows, transients dominate and the Eddy Kinetic Energy exceeds the Mean Kinetic Energy by an order of magnitude (Gill et al., 1974; Chelton et al., 2011b). An analysis of the relationship between eddy activity and isopycn gradients has shown that the main part of the mesoscale eddies of the Lofoten Basin is generated by instability in the boundary currents and frontal zones of the Norwegian Sea (Trodahl and Isachsen, 2018;

Travkin and Akhtyamova, 2023). The potential energy of such eddies can be 1.5 times higher than their kinetic energy, while during the transformation of a eddy, its kinetic energy can decrease by 3 times, and its potential by 1.7 times (Zhmur et al., 2022). The results of field studies have shown that the values of APE and EKE in the LV core are $3.4 \cdot 10^{14}$ J and $5.9 \cdot 10^{14}$ J, respectively (Fer et al., 2018). In this case, the average Burger eddy number (Bu_E) is 1.75 (D'Asaro, 1988). These values are 10-20 times higher than the estimates obtained for the Lofoten Vortex and the anticyclonic eddy in the North Atlantic (Søiland et al., 2016; Fernández-Castro et al., 2020). It has been found that EKE and APE are almost unchanged below 1500 m, which is associated with weak density stratification gradients and low velocities (Bosse et al., 2019).

The purpose of this chapter is to evaluate the components of the total energy in the Lofoten Basin: Mean and Eddy Kinetic Energy, Available Potential and Kinetic Energy of the Lofoten Vortex, as well as to analyze their variability. Energy redistribution is considered during the period of the greatest intensity of deep convection (January – March) and in the summer period (June – August). A detailed study of these processes will clarify the understanding of the mesoscale dynamics of the Lofoten Basin and the importance of kinetic and potential energy in the regeneration of the Lofoten Vortex.

Results

Figure 1.11 shows the spatial distribution of kinetic energy components in the Lofoten Basin. It can be noted that the maximum EKE values are concentrated in the area of the LV core (up to $250 \text{ cm}^2 \cdot \text{s}^{-2}$) (Fig. 1.11a). Elevated values (up to $100\text{-}130 \text{ cm}^2 \cdot \text{s}^{-2}$) are also observed in the northwestern and eastern parts of the Lofoten Basin, as well as on the continental slope of Norway. In other parts of the basin, the EKE value does not exceed $50 \text{ cm}^2 \cdot \text{s}^{-2}$.

The MKE in the Lofoten Basin is characterized by lower values compared to the EKE (Fig. 1.11b). The highest values (up to $190 \text{ cm}^2 \cdot \text{s}^{-2}$) were also recorded in the LV area. It is worth noting that the EKE maxima correspond to the central part of the vortex (approximately 69.8° N , 4.8° E), while the MKE values in this area are

close to zero, and increased MKE values are observed at the periphery of the vortex. Increased MKE values are also recorded along the isobaths, following the topography of the basin (Fig. 1.11b). This feature is explained by the location of the main jets of the Norwegian slope and Norwegian frontal currents (Fig. 1). The difference between EKE and MKE is positive in most of the Lofoten Basin, with the maximum observed in the area of the LV core, and significant values in the central and eastern parts of the Lofoten Basin. On the other hand, the difference is negative on the periphery of the LV, and in the area of the Voring Plateau and in the western part of the Lofoten Basin it is close to zero.

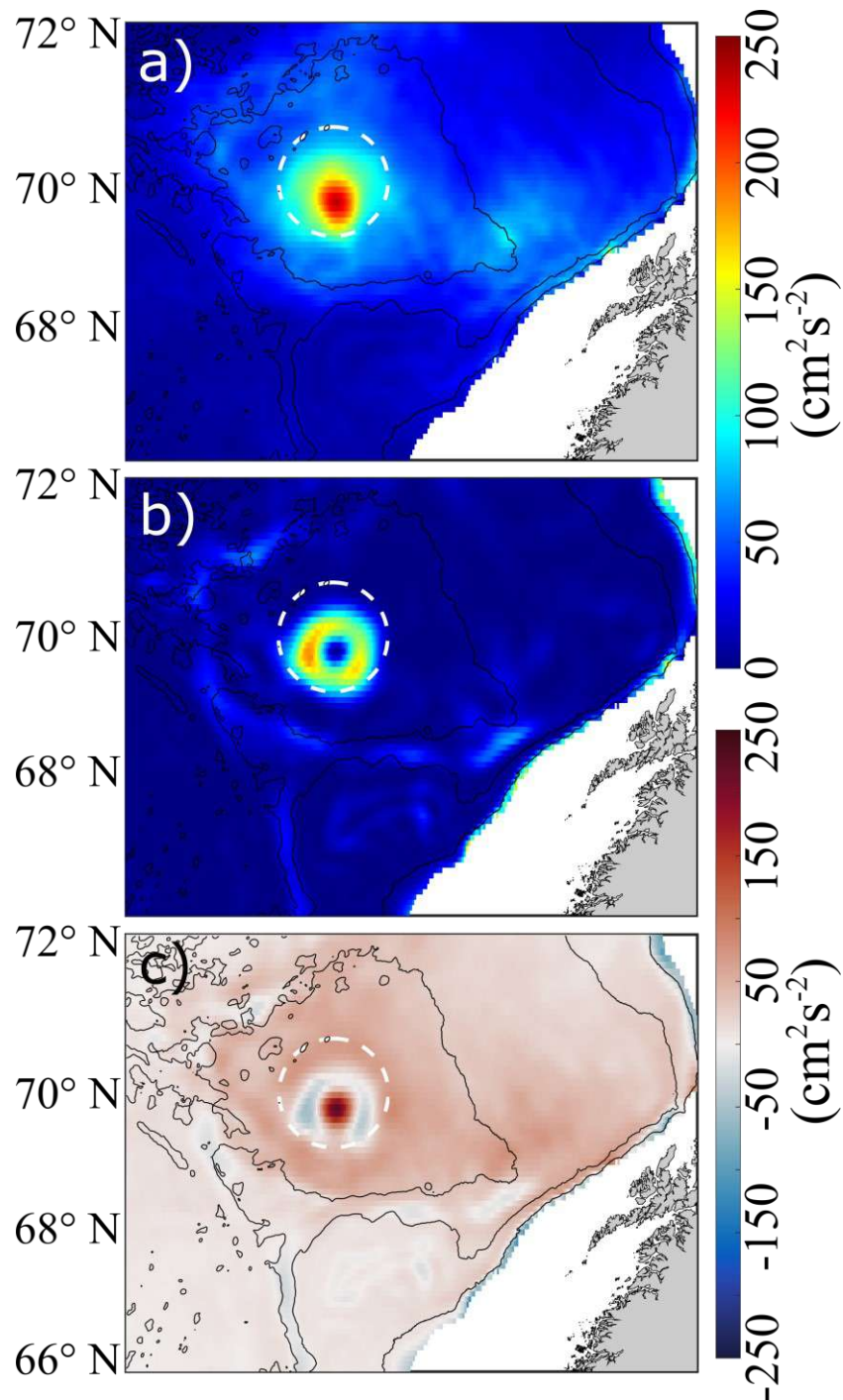


Figure 1.11. Spatial distribution on the 500 m horizon: a – EKE; b – MKE; c – difference between EKE and MKE. Averaging over the period 2010-2018. The black lines show isobaths of 1000, 2000 and 3000 m.

The vertical distribution of these characteristics is shown in Figure 1.12. For the winter period, average estimates were taken from January to March, for the summer period from June to August. It can be noted that at all horizons from 0 to

1000 m, EKE exceeds MKE. This is most pronounced in the layer from 100 to 500 m, where the difference is greatest. It is also worth noting the presence of pronounced seasonal variability, leading to an increase in both EKE and MKE in the winter season, compared with the summer period (Fig. 1.12).

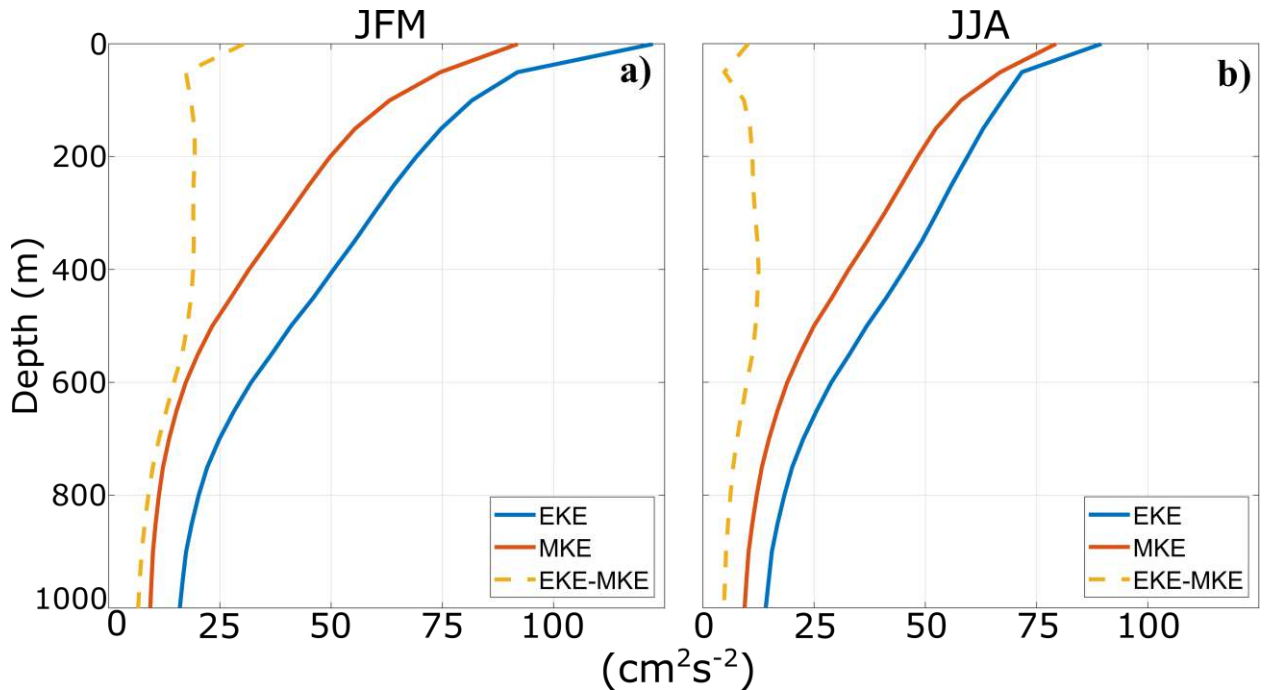


Figure 1.12. Vertical profiles of long-term values of EKE (blue line), MKE (red line) and their differences (EKE – MKE) (yellow line): a - January – March (JFM); b – June – August (JJA).

Figure 1.13 shows the evolution of the volume values of the available potential (APE_V) and kinetic energy (KE), as well as the Burger number for LV. It is noticeable that the evolution of APE_V is characterized by a positive significant trend, whereas there is no significant trend for KE. Such an increase in APE_V may be due to the deepening of isosteric surfaces in the Lofoten Basin due to ongoing climatic changes in the North Atlantic and the Arctic Basin (Novoselova and Belonenko, 2020). The obtained APE_V and KE estimates are generally close to the values from earlier studies (Søiland et al., 2016; Fernández-Castro et al., 2020). Thus, LV is characterized by the dominance of APE_V (from $0.1 \cdot 10^{15}$ to $5.5 \cdot 10^{15}$ J) over KE (from $0.2 \cdot 10^{14}$ to $3.0 \cdot 10^{14}$ J), which leads to a Bu_E value of the order of

0.02–0.13 (Fig. 1.13). Also, for APE_V , there is a significant positive trend equal to $0.23 \cdot 10^{15}$ J/year, leading to a decrease in the Burger eddy number (Fig. 1.13).

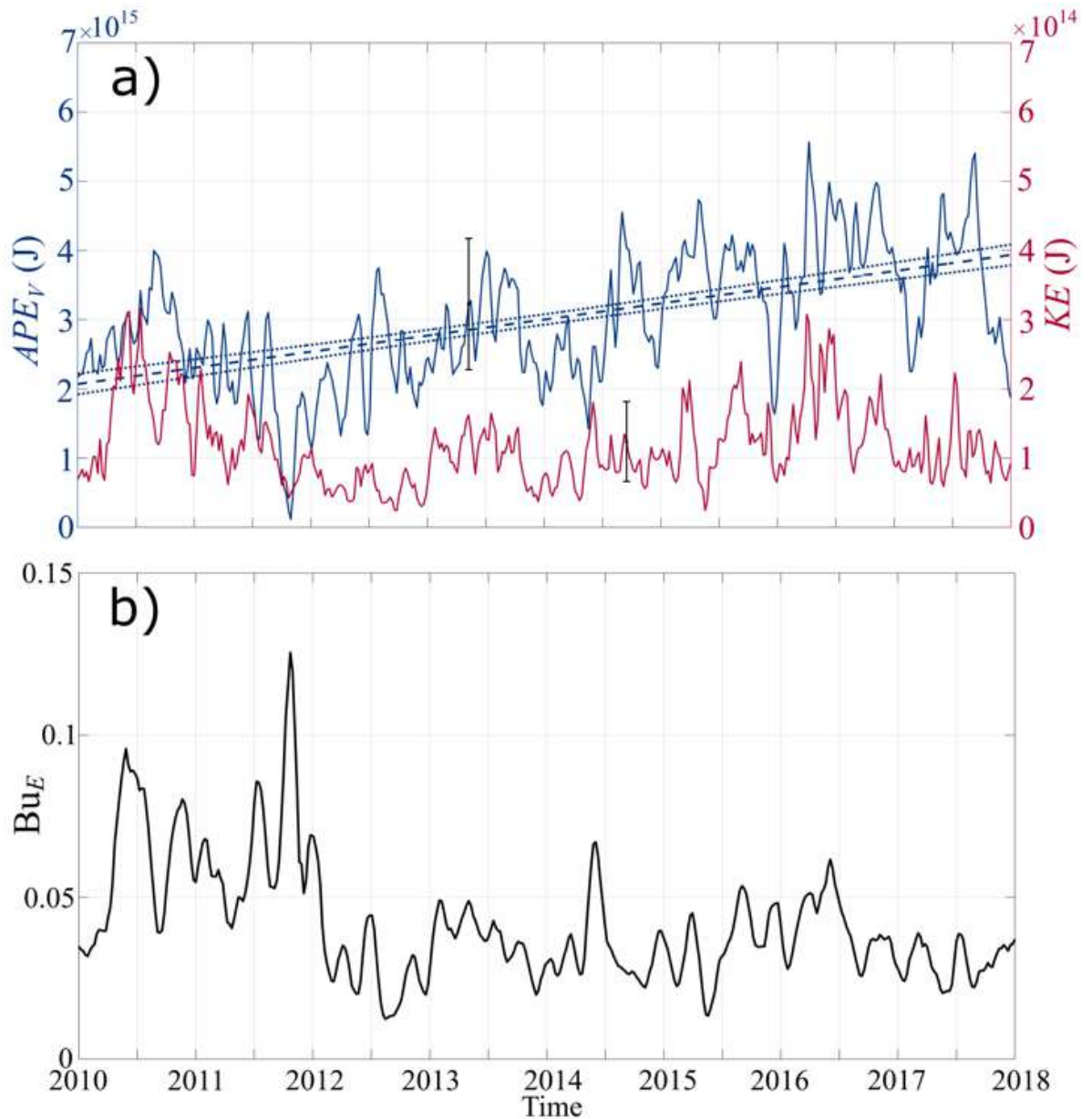


Figure 1.13. Time course of APE_V (blue curve) and KE (red curve) and linear trend of APE_V (blue dashed line) with confidence intervals (blue dotted lines) (a); evolution of the Burger eddy number (b)

Vertical profiles APE_V , KE and Bu_E , plotted with weekly averaging, as well as averaged for 2010-2018, are shown in Figure 1.14. It is noticeable that APE_V can have negative values in the layer from 0 to 400 m. This indicates a denser water mass

in the eddy compared to the waters surrounding the eddy. The fastest change in APE_V is recorded in the intermediate layer (200-800 m). At the same time, the maximum average APE_V value was recorded at a horizon of 700 m, which indicates significant density gradients due to the displacement of the isopycn. In general, the highest APE_V values are observed in the layer from 600 to 900 m. The KE values are positive and decrease gradually with depth (Fig. 1.14). The highest values are observed in the surface layer from 0 to 300 m. Subsequently, the KE values decrease, and most intensively in the layer from 750 to 1000 m. All of the above leads to the fact that the maximum values of the Burger number are fixed in the layer from 0 to 500 m, with individual values exceeding 1.75 modulo (Fig. 1.14). The maximum gradients of the Burger number are typical for the area of the LV core (300-400 m).

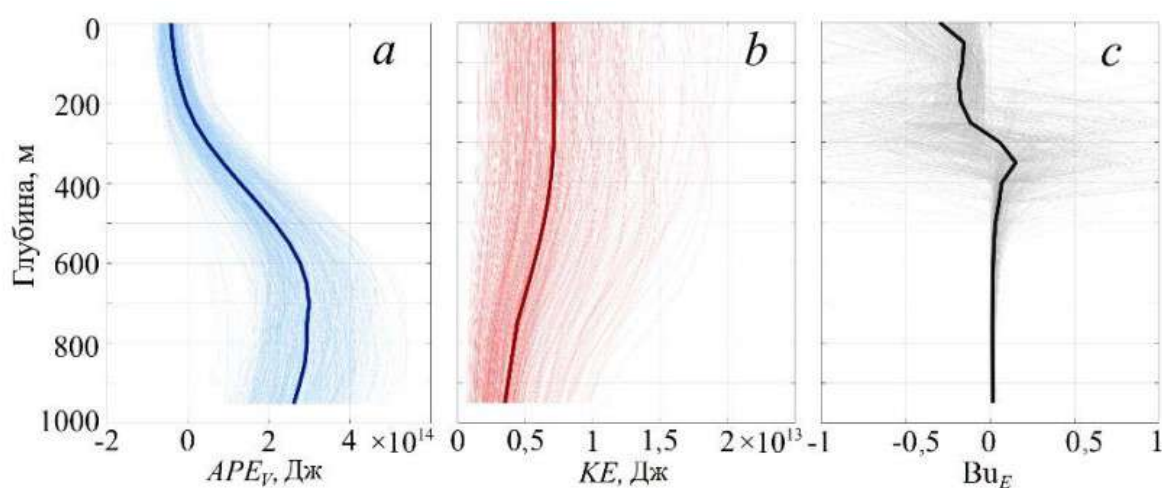


Figure 1.14. Vertical profiles (thin lines) of APE_V (a), KE(b), and Burger's eddy number Bu_E (c) in the Lofoten Vortex. The average value of each value is shown by a thick line.

Of greatest interest are the graphs of the rate of barotropic and baroclinic energy conversion, demonstrating the conversion of the components of total energy among themselves (Figures 1.15 and 1.16). In Figure 1.15, it is noticeable that the most active energy-active zones of the Lofoten Basin are the area of the LV location, as well as the core of the NwASC. It is worth noting that both positive and negative significant values are observed in various parts of LV. Such an alternation of red and

blue regions in the eddy zone indicates an active transition of the eddy kinetic energy to the average field, and vice versa. In winter, there is an area of negative values in the western part of LV, while in the central and southern parts there is an area of positive values. Thus, the LV core is characterized by the energy transition from the mean kinetic field (MKE) to EKE. Obviously, this feature indicates the stability of the LV and its permanent location in the area. During the summer period, areas of negative values are observed in the western and southeastern parts of the LV periphery, indicating the transformation of energy from EKE to MKE (Fig. 1.15). A similar alternation of areas with positive and negative vertical velocities in LV is analyzed in detail in the work of Koldunov and Belonenko (2020). The authors explain this feature by the influence of the NwASC. It is likely that the symmetrical arrangement of areas with positive and negative BT values is also due to the influence of the current.

The second energy-active area of the research area is the area of the NwASC. Thus, negative BT values are observed in the western part of the current, while positive values are observed in the eastern part (Figure 1.15). A detailed analysis of this phenomenon is presented in Raj et al., 2020. It is worth noting that in the summer period, energy conversion occurs more intensively both in the LV area and in the NwASC, compared with the winter period (Fig. 1.15).

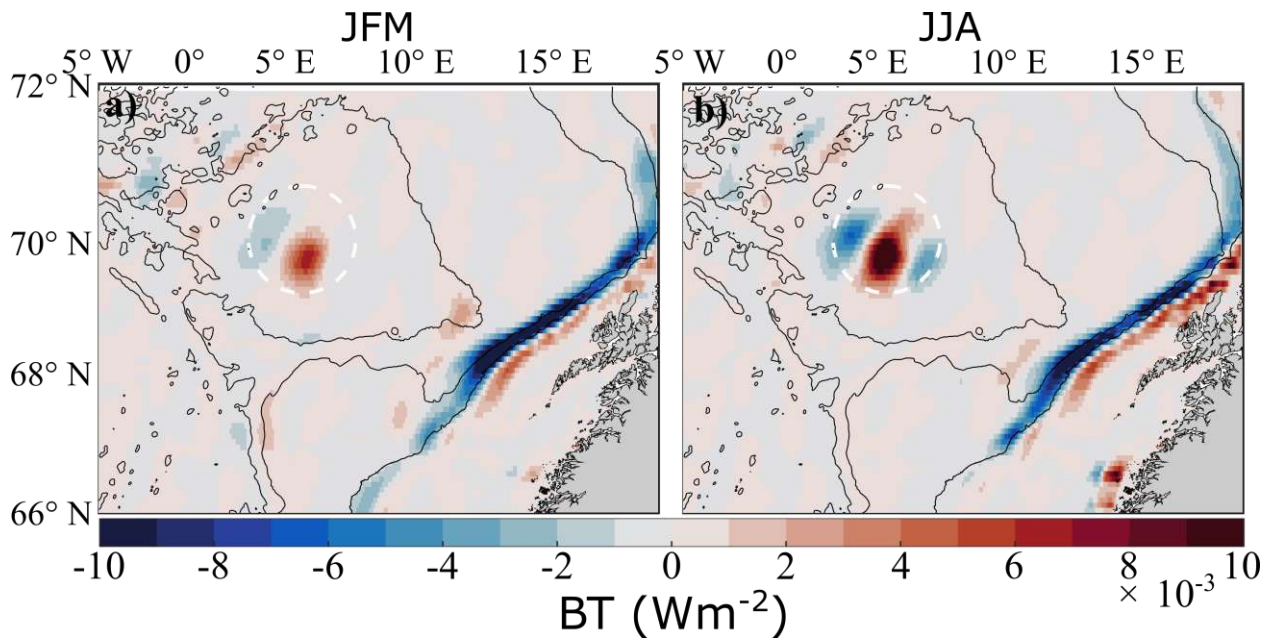


Figure 1.15. Spatial distribution of BT (conversion of MKE to EKE) integrated into the upper 500-meter sea for the period: a – January – March (JFM); b – June – August (JJA). The black lines show isobaths at 1000, 2000 and 3000 m.

The positive BC values in Figure 1.16 indicate the transition from Mean Potential Energy (MPE) to APE, while the negative values indicate a transition in the opposite direction. It can be noted that in winter, BC values exceed by more than 4 times the same values for the summer period. The reason for such a sharp intensification of BC in winter is the weak stratification of the upper layer, as well as the low values of the Brunt–Väisälä frequency as a result of the formation of a powerful mixed layer. The highest values are observed in the central and eastern parts of the Lofoten Basin, as well as over the continental slope of Norway. Surprisingly, BC values are not so significant in the surrounding area of the Norwegian Basin (Fig. 1.16). In winter, an area of negative values is formed in the area of the continental slope along the isobaths, whereas in summer, positive values are recorded in this area. In the LV area, there is an alternation of two regions in the summer period: negative in the central part of the vortex and positive in the eastern part of the LV.

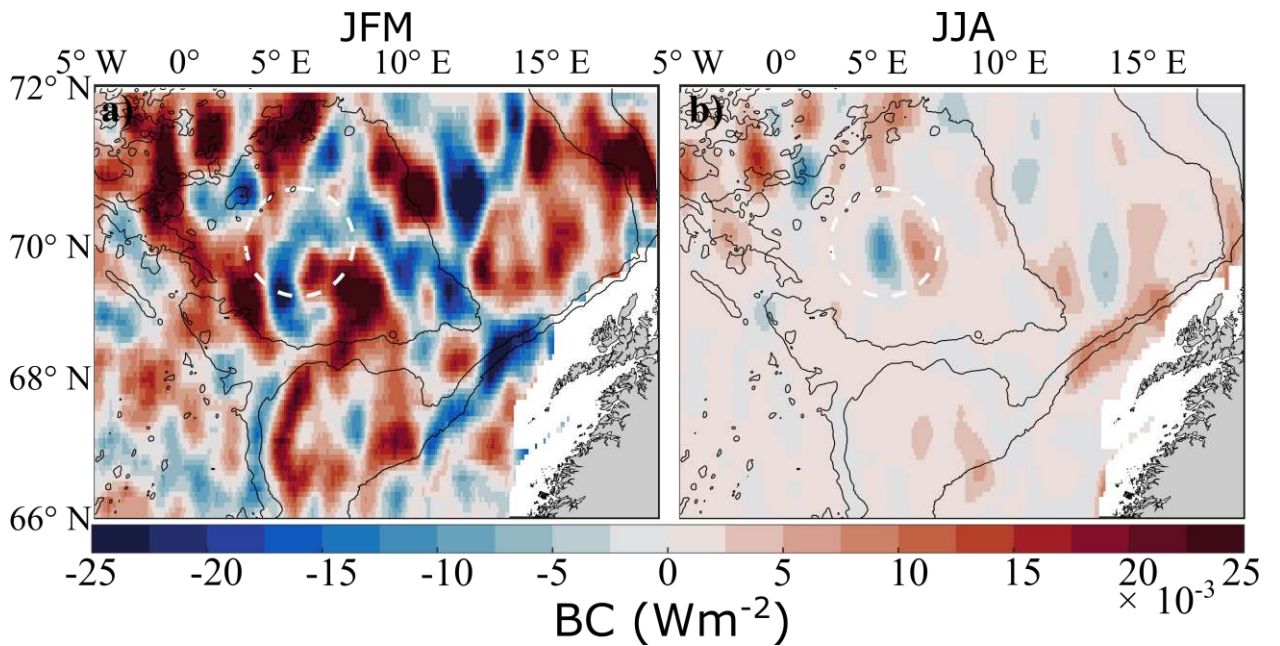


Figure 1.16. Spatial distribution of BC (MPE to APE conversion) integrated into the upper 500-meter sea for the period: a – January – March (JFM); b – June – August (JJA). The black lines show isobaths at 1000, 2000 and 3000 m.

Conclusions

It is shown that the EKE has significant values in the LV core, while the MKE values dominate at the periphery of the eddy. The analysis of vertical kinetic energy profiles indicates an increase in mesoscale eddy activity in winter, compared with summer, while the eddy component dominates at all studied horizons from 0 to 1000 m. It has been established that the available potential energy of LV exceeds the kinetic energy by an order of magnitude, and demonstrates a positive linear trend. The presence of a significant positive trend with a coefficient of $0.23 \cdot 10^{15}$ J/year indicates a deepening of the isopycnic surfaces, which, in turn, is associated with climatic changes in the North Atlantic and the Arctic basin. The increase in available potential energy helps to reduce the eddy Burger number in LV. Negative values of the available potential energy LV were detected in the surface layer from 0 to 300 m. The maximum values of the available potential energy in the eddy are fixed at the horizon of 700 m, while the greatest contribution to the potential energy is made by the layer of 600-900 m. The maximum kinetic energy values are observed in the

layer from 0 to 300 m. As the depth increases, the KE slowly decreases, accelerating the descent after 750 m. Thus, the layer 0-400 m makes the greatest contribution to the kinetic energy of the eddy. The Burger eddy number varies significantly in the layer from 0 to 400 m, with values for individual profiles reaching 1.75.

Graphs of the rate of barotropic energy conversion BT (MKE→EKE) demonstrate the presence of multidirectional flows in the eddy zone. Thus, a dipole structure is observed in winter, while a tripole structure is observed in summer, and fluxes are more significant in the LV region in summer. The NwASC area is characterized by negative BT values in the west and positive values in the east, both in summer and winter.

On the other hand, the rate of baroclinic energy conversion BC (MPE→APE) is characterized by a sharp intensification in winter, which is associated with a weakening of density stratification due to significant winter convection. During this period, areas with a predominance of positive BC values are formed in the Lofoten Basin, while an area of negative values is formed in the area of the NwASC. In winter, increased values of baroclinic instability are observed throughout the Lofoten Basin, and the baroclinic instability is many times higher than the barotropic one. However, in summer, the barotropic instability exceeds the corresponding BC values.

1.6 Influence of topography on the formation of the quasi-permanent Lofoten Vortex

Despite the fact that there are currently a large number of articles devoted to the dynamics and thermohaline properties of LV, the influence of topography on its formation has practically not been considered (Belonenko et al., 2021a). Using numerical experiments with a bowl-shaped basin, Shchepetkin demonstrated that initially the turbulent flow tends to form a cyclonic circulation along the periphery of the basin, while an anticyclonic eddy forms in the center of the basin (Shchepetkin, 1995). Earlier, using experiments with a rotating basin, it was found that if the horizontal scale of the eddies is smaller than the size of the basin, the

topographic beta effect will promote the movement of anticyclones along a cyclonic trajectory downhill to the center of the topographic depression, while cyclones will move up the slope (Carnevale et al., 1991). Thus, the cyclonic propagation of anticyclones into the deepwater part of the Lofoten Basin and their subsequent fusion with each other can be considered as a mechanism responsible for the formation and stability of a quasi-permanent LV and its location in the central part of the basin. This hypothesis was considered in detail and confirmed by numerical experiments with eddy resolution, which also proved the significant effect of eddies on the formation and regeneration of LV (Volkov et al., 2015). Thus, the topographic structure of the Lofoten Basin may contribute to the fact that the anticyclonic LV is located in the central part of the basin and does not leave its limits, only moving inside it along a quasi-cyclonic trajectory (Benilov, 2005; Bloshkina and Ivanov, 2016). The main purpose of this part of our study is to study the role of bottom topography in the formation of LV. In particular, we aim to answer the following questions: (i) Why does a quasi-permanent anticyclonic eddy form in the Lofoten basin, but in the Norwegian one? (ii) Will the characteristics of the anticyclonic eddy in the center of the Lofoten Basin differ for different types of bottom topography? (iii) How does the variability of mesoscale eddy dynamics affect the formation of LV? (iv) How does the bottom topography affect the MLD in the Norwegian Sea? (v) Is there a relationship between the MLD and mesoscale eddy activity?

To answer these questions, we conducted four numerical experiments with a modified seabed topography, but with realistic forcing and conditions at the lateral boundaries (Fig. 1.1).

Results

Mean circulation of the Norwegian Sea

Figure 1.17 shows stream lines based on average velocities for a horizon of 95 m. The graphs clearly show the main structures of large-scale circulation in the TOPO1-4 experiments. As expected, the main currents of the studied area follow the isobaths. It can be noted that the absence of the Voring Plateau in the TOPO2 and

TOPO3 experiments significantly affects the circulation (Fig. 1.17). On the other hand, the absence of a boundary between basins favorably affects the water exchange between them. An anticyclonic eddy is formed in experiments TOPO1 and TOPO2, while the eddy is not detected in experiments TOPO3 and TOPO4. It is worth noting that the size of the eddy in the TOPO2 experiment is slightly larger than the size of the eddy in the TOPO1 experiment. Interestingly, in the TOPO3 experiment, the Lofoten Vortex does not form in the Lofoten Basin, whereas a quasi-permanent anticyclonic eddy forms in the deepwater part of the Norwegian Basin (Figure 1.17). However, it should be remembered that in TOPO3 we smoothed the topography of the seabed of the Norwegian Basin and removed seamounts and ridges. So, in TOPO4 (an experiment with a realistic relief of the Norwegian Basin) The anticyclonic eddy is no longer forming in the Norwegian Basin. Based on the above, it becomes clear that a favorable seabed topography is a necessary condition for the formation of a quasi-permanent eddy in the center of a topographic depression. Thus, the anticyclonic vortex formed in the Norwegian Basin in TOPO3 has similar dimensions and intensity to the LV in the TOPO1 experiment.

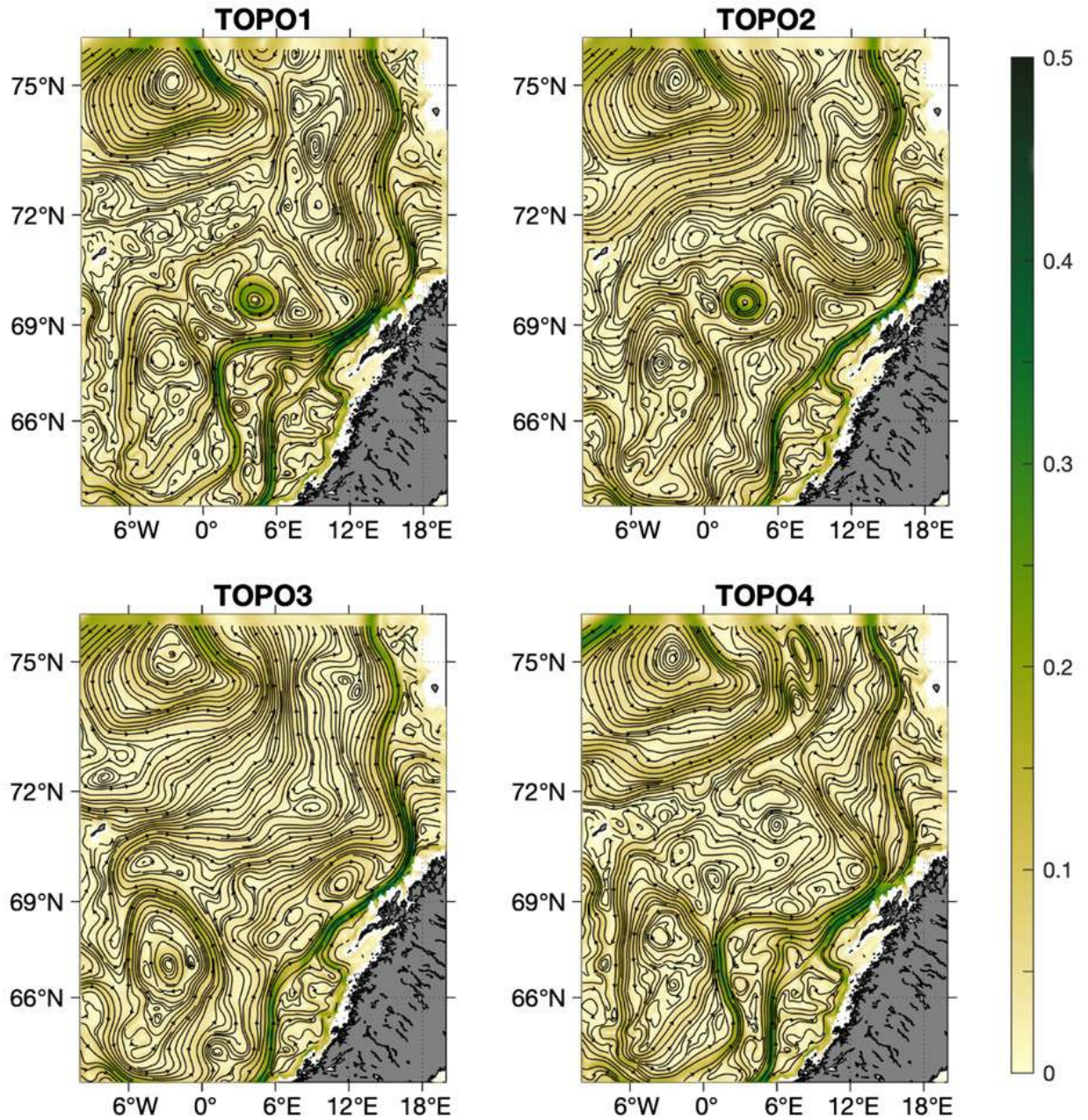


Figure 1.17. Average current velocities (m/s) and streamlines for a 95 m horizon in TOPO 1-4 experiments.

Vertical sections through the Lofoten and Norwegian basins

Since the main focus of this work is on quasi-permanent LV, we have considered two vertical sections. The first incision runs along 69.72° N and intersects the center of the LV in the Lofoten Basin (see experiment TOPO1 in Fig.1.18). The second incision is made through 67.02° N and intersects the center of the quasi-permanent eddy formed in the Norwegian Basin in experiment TOPO3

(see experiment TOPO3 in Fig.1.18). In Figure 1.18, it is noticeable that the maximum velocities in the Lofoten Basin are recorded in the LV region (see experiments TOPO1-2 in Fig.1.18). The significant velocities associated with LV can be traced to the very bottom, while the greatest velocities are concentrated in the core of the eddy in the upper layer from 0 to 1000 m. The TOPO1 experiment also clearly shows a powerful branch of the NwAFC. It is worth noting that significant (more than 15 cm/s) speeds of the NwAFC can be traced to the very bottom (3250 m). This feature is not found in the TOPO2 experiment, in which the NwAFC is weakened (Fig. 1.18). In the TOPO1 experiment, there is also an increase in the NwASC with maximum velocities in the upper 500-meter layer, whereas in TOPO2 this branch of the Norwegian current is less pronounced. In the TOPO3 experiment, the velocities are insignificant; a slight increase is observed only near the coast of Norway at depths up to 500 m. The TOPO4 experiment shows an increase in the branches of the Norwegian current, while the velocities in the center of the Lofoten Basin are insignificant (Fig. 1.18).

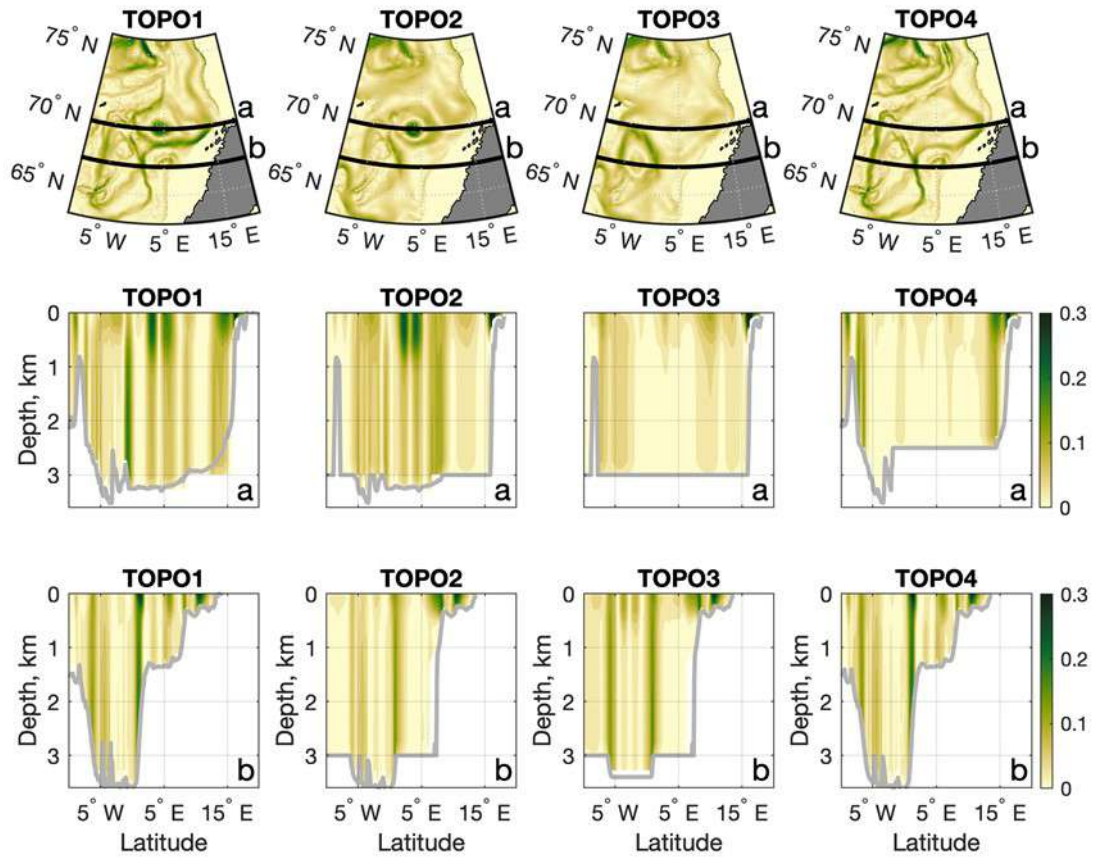


Figure 1.18. Average velocities at a depth of 500 m (from above) and vertical sections through 69.72°N (a) and 67.02°N (b) for TOPO 1-4 experiments.

Figures 1.19 and 1.20 show the average values of water temperature and salinity at the 500 m horizon, as well as along the sections. The transfer of warm and salty waters from the NwASC in a westerly direction is clearly noticeable. In the TOPO1 and TOPO2 experiments, the vertical length of the eddy exceeds 1300 m, whereas the eddy in the Norwegian Basin can be traced by temperature and salinity at shallower depths. In the TOPO3, the eddy in the center of the Norwegian Basin appears at depths up to 1100 m. In the TOPO4 experiment, a quasi-permanent eddy does not form in any of the basins.

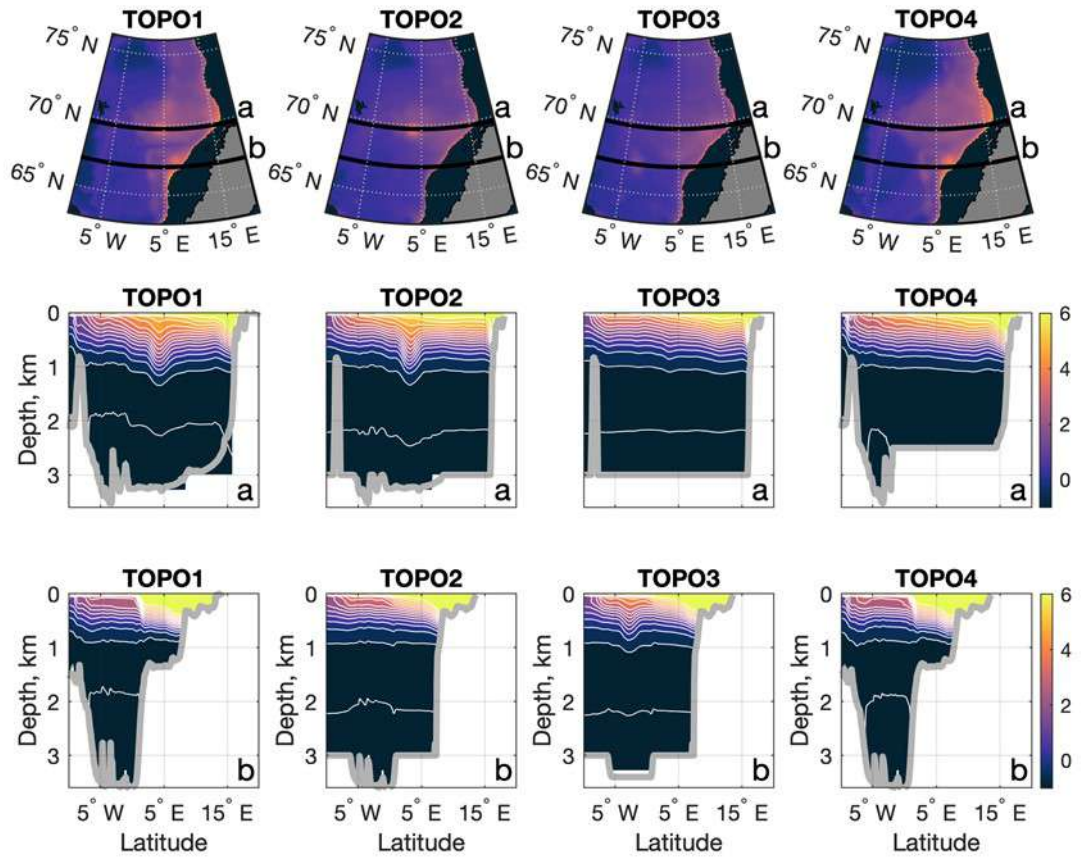


Figure 1.19. Water temperature ($^{\circ}\text{C}$) at a depth of 500 m (from above) and vertical profiles of water temperature through 69.72°N (a) and (b) in experiments TOPO1-

4.

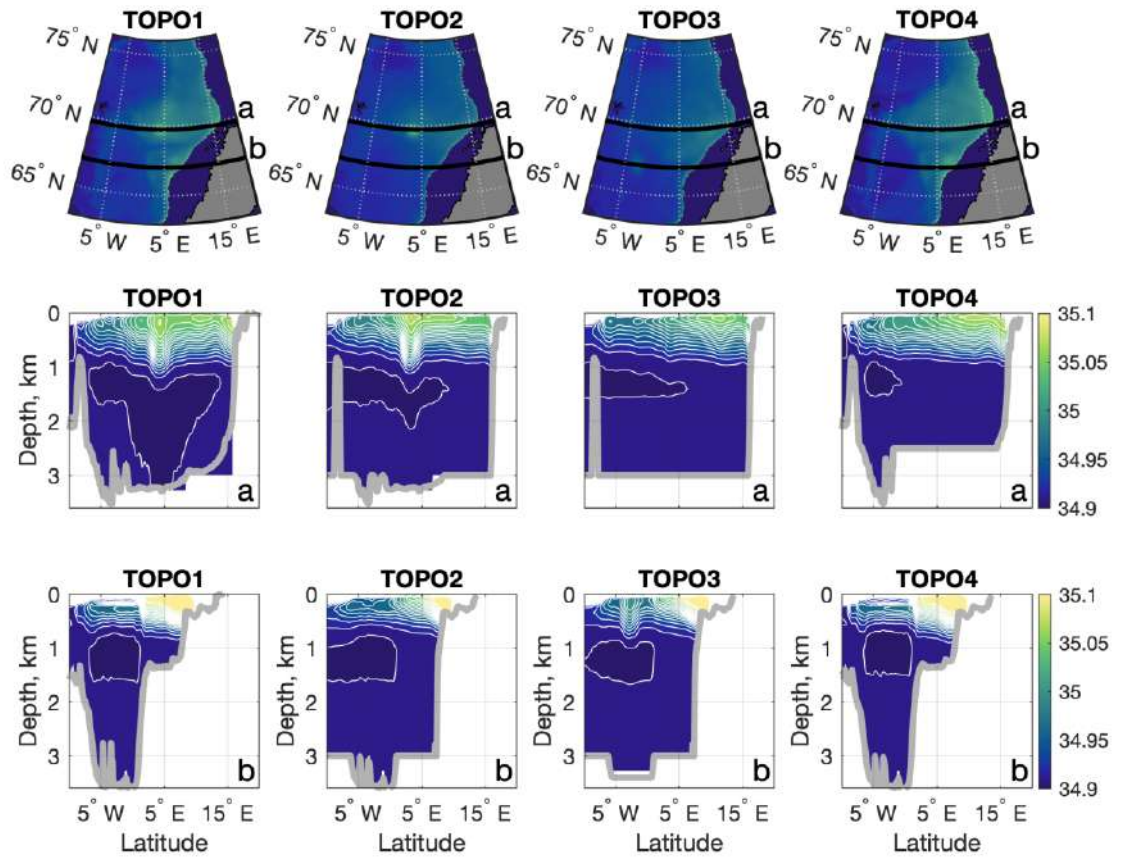


Figure 1.20. Water salinity (psu) at a depth of 500 m (from above) and vertical profiles of water salinity through 69.72°N (a) and (b) in experiments TOPO1-4.

In the TOPO1 experiment, a quasi-permanent anticyclone forms in the center of LV after six months from the launch of the MITgcm model. In July 1992, a large anticyclone was observed in the center of the Lofoten Basin (69.8°N , 5.9°E). This eddy moved slowly inside the basin and existed until the very end of the experiment (Fig. 1.21). It is important to note that in the TOPO1 experiment, the presence of several large anticyclones was noted at each time. In Fig. 1.21 It can be seen that these eddies are concentrated in the areas of the main currents of the studied area, since their origin is associated with barotropic and baroclinic instability. In the TOPO2 experiment, LV formation occurs one month earlier than TOPO1. In TOPO3, mesoscale eddy activity is significant in the Lofoten and Norwegian Basins, while no quasi-permanent eddy formation occurs in the center of the Lofoten Basin. The removal of the topographic barrier between the basins allows the anticyclones

formed in the Lofoten Basin to penetrate into the Norwegian Basin and become involved in cyclonic circulation, following the f/H contours (Fig. 1.22). The TOPO4 experiment shows how important the role of the topography of the seabed and, in particular, the boundary separating the two basins of the Norwegian Sea. Thus, with the disappearance of the Voring Plateau and the Helgeland Range, the Norwegian Sea becomes a single area in which various types of mesoscale activity are active throughout the basin. In contrast to the TOPO3 experiment, the boundary between basins exists in TOPO2 and TOPO4, which leads to increased eddy activity in the Lofoten Basin and its almost complete absence in the Norwegian Basin in these experiments (Figure 1.22). Thus, it is likely that the smooth relief of the seabed without significant sea mountains and ridges is the most important factor to form a quasi-permanent eddy in the Norwegian Basin.

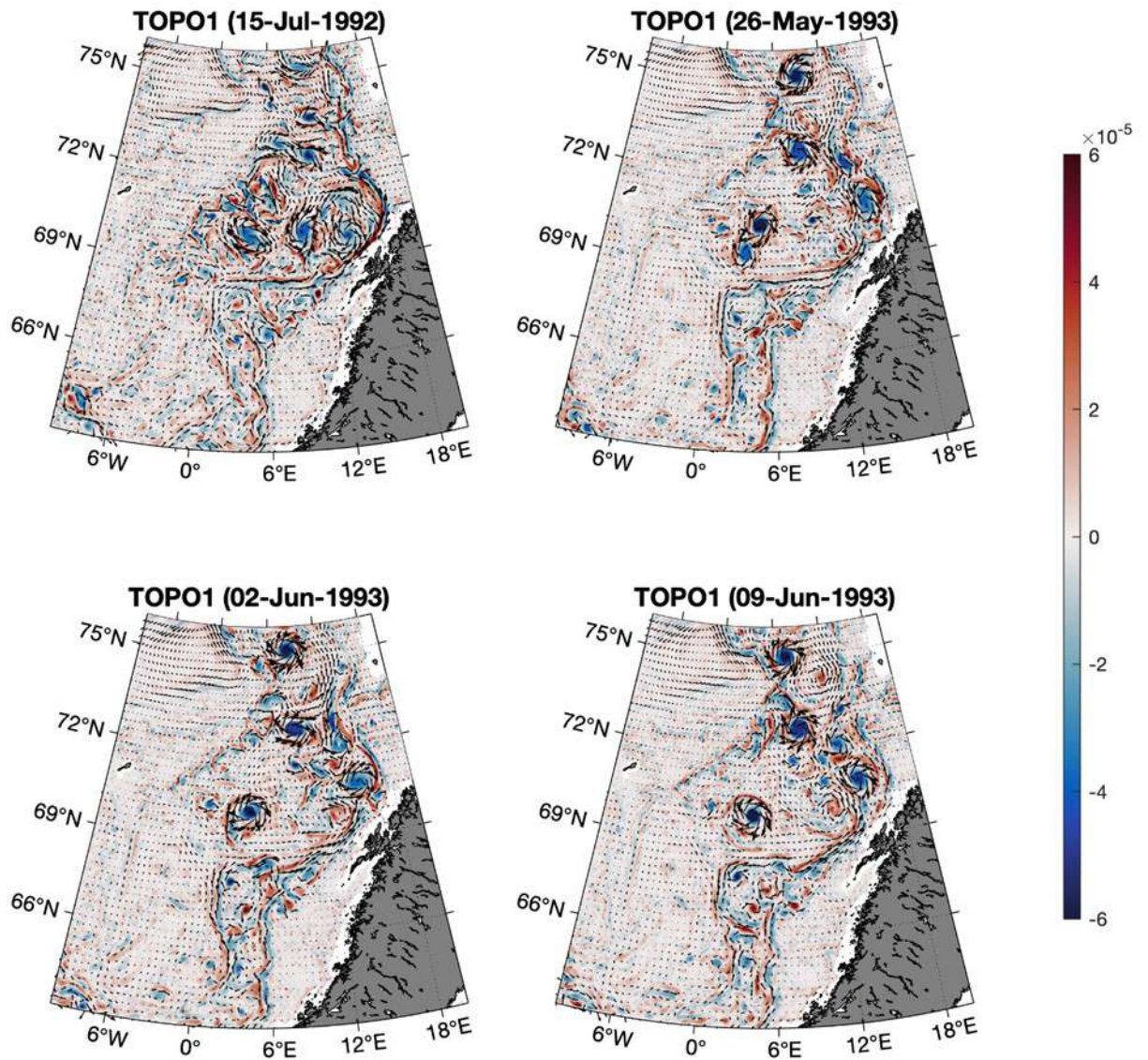


Figure 1.21. Relative vorticity at a depth of 95 m in the TOPO1 experiment. The arrows indicate the current velocities.

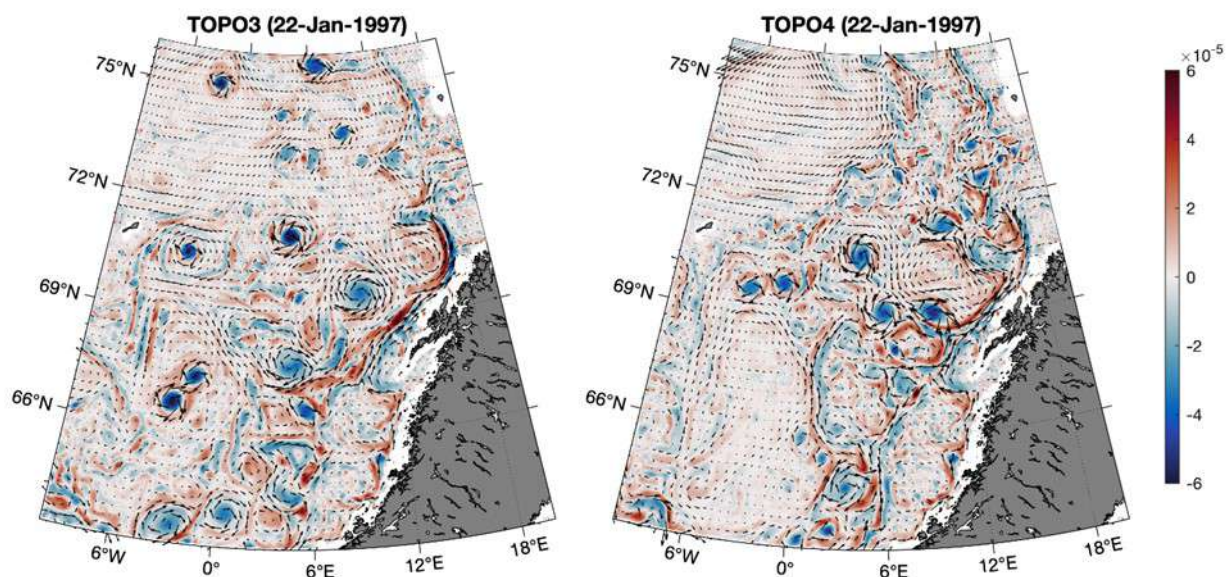


Figure 1.22. Relative vorticity at a depth of 95 m in the TOPO3 and TOPO4 experiments. The arrows indicate the current velocities.

The period of formation of a quasi-permanent anticyclone in the Norwegian Sea is different for the two basins (Table 1.3). It can be noted that it takes 2-3 times longer for an anticyclone to form in the Norwegian Basin than for an anticyclone in the Lofoten Basin.

Table 1.3. Time (months) required for the formation of a quasi-permanent anticyclone in the center of the basin.

Experiment	Lofoten Basin	Norwegian Basin
TOPO1	6,5	not detected
TOPO2	5,5	not detected
TOPO3	not detected	22
TOPO4	not detected	14

Winter convection in the Norwegian Sea in TOPO 1-4 experiments

Figure 1.23 shows the time evolution of the MLD for 1993-1997 for the TOPO experiments. It was found that the MLD in the Lofoten Basin exceeds similar values for the Norwegian basin in TOPO1, TOPO2 and TOPO4, although similar values

are observed in TOPO3 in both basins. This similarity is explained by the absence of a boundary between the basins, as a result of which mesoscale eddies are concentrated in the Norwegian Basin and contribute to the development of deep convection in the winter-spring period. It is the presence of a quasi-stationary eddy that contributes to turbulent mixing and an increase in the MLD in this area.

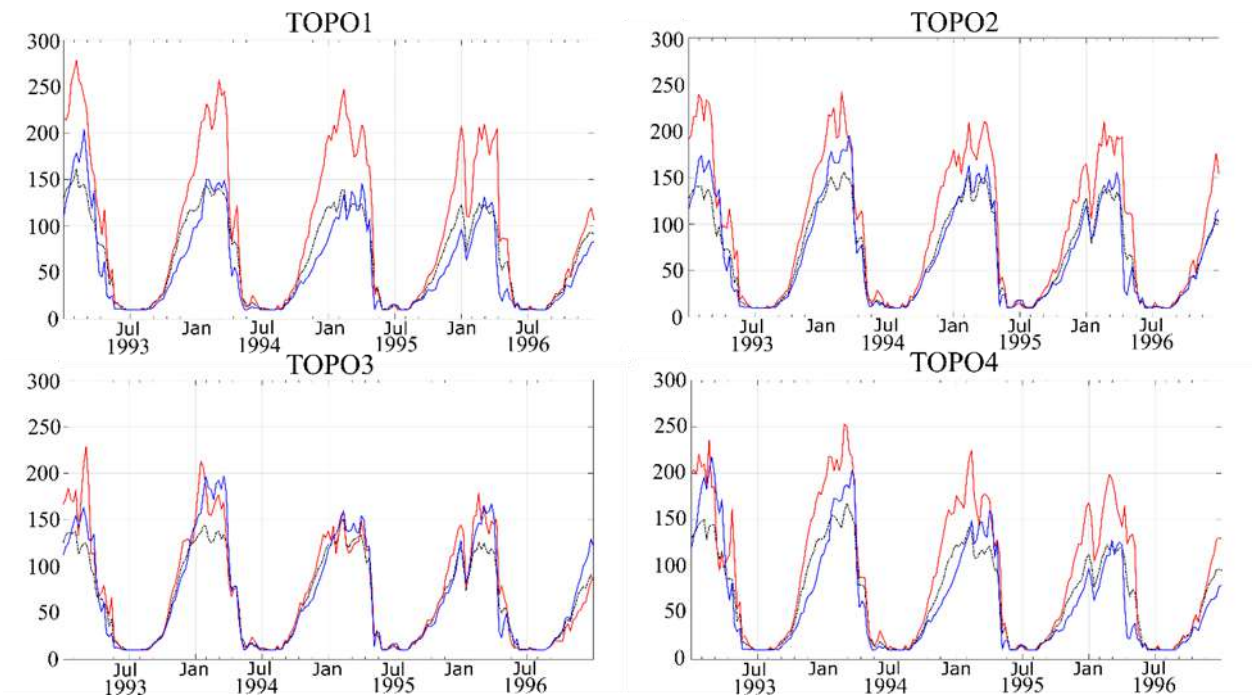


Figure 1.23. The time evolution of the MLD for 1993-1997, averaged for the Lofoten Basin (red), the Norwegian Basin (blue), as well as for the entire Norwegian Sea (black) in the TOPO1-4 experiments.

In December and January, the average values of the MLD in the TOPO experiments do not exceed 125 m, whereas in February they increase and reach a maximum (Figure 1.24). Then in March, the MLD decreases slightly, while in April the MLD is lower than in December, indicating an almost complete cessation of mixing. The highest values of the MLD were found in the TOPO2 experiment, while the highest values were found in the TOPO3 experiment.

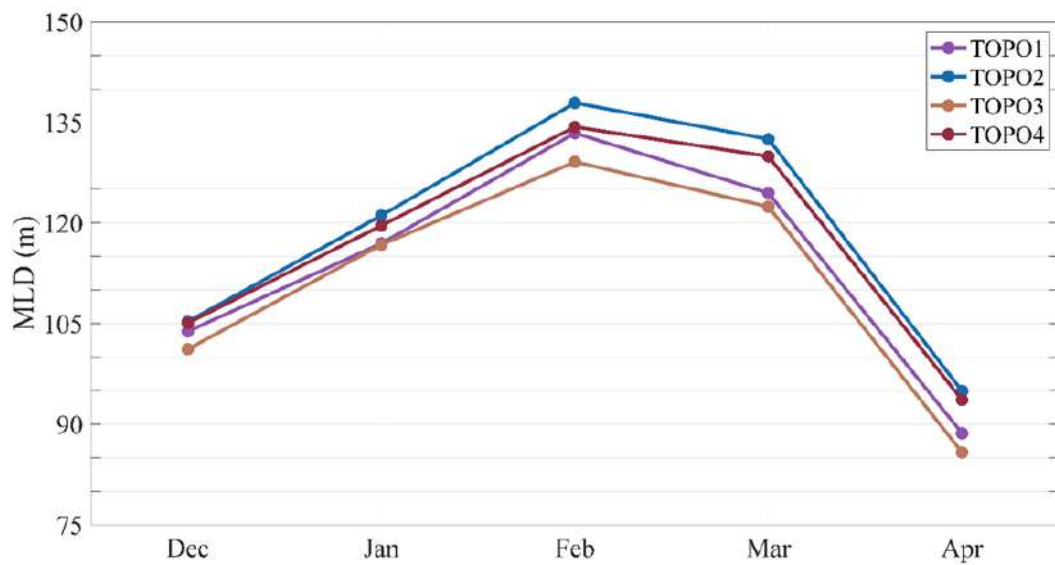


Figure 1.24. Temporal variability of the average values of the MLD for 1993-1997 in the TOPO1-4 experiments.

It is known that annual deep convection is the main reason for the regeneration of quasi-permanent LV and its stability (Ivanov and Korablev, 1995a). The spatial distribution of the MLD in the TOPO experiments demonstrates that the maxima are characteristic of areas where quasi-permanent eddies are located (Figure 1.25). This feature was also found in other works devoted to estimating the MLD using satellite, field, and model data (Nilsen and Falck, 2006; Fedorov et al., 2019). Figure 1.25 shows that the MLD in the Lofoten Basin exceeds 400 m in the area of the LV location. In the TOPO3 experiment, the maximum values of the MLD were found in the Norwegian Basin, which is associated with the presence of a quasi-permanent anticyclone in this area. In the TOPO4 experiment, the highest values of the MLD were recorded in the Lofoten Basin and near the Voring Plateau. It is worth noting that the Voring Plateau exists only in the TOPO1 and TOPO4 experiments, and in both experiments a significant MLD is noted in this area (Fig. 1.25).

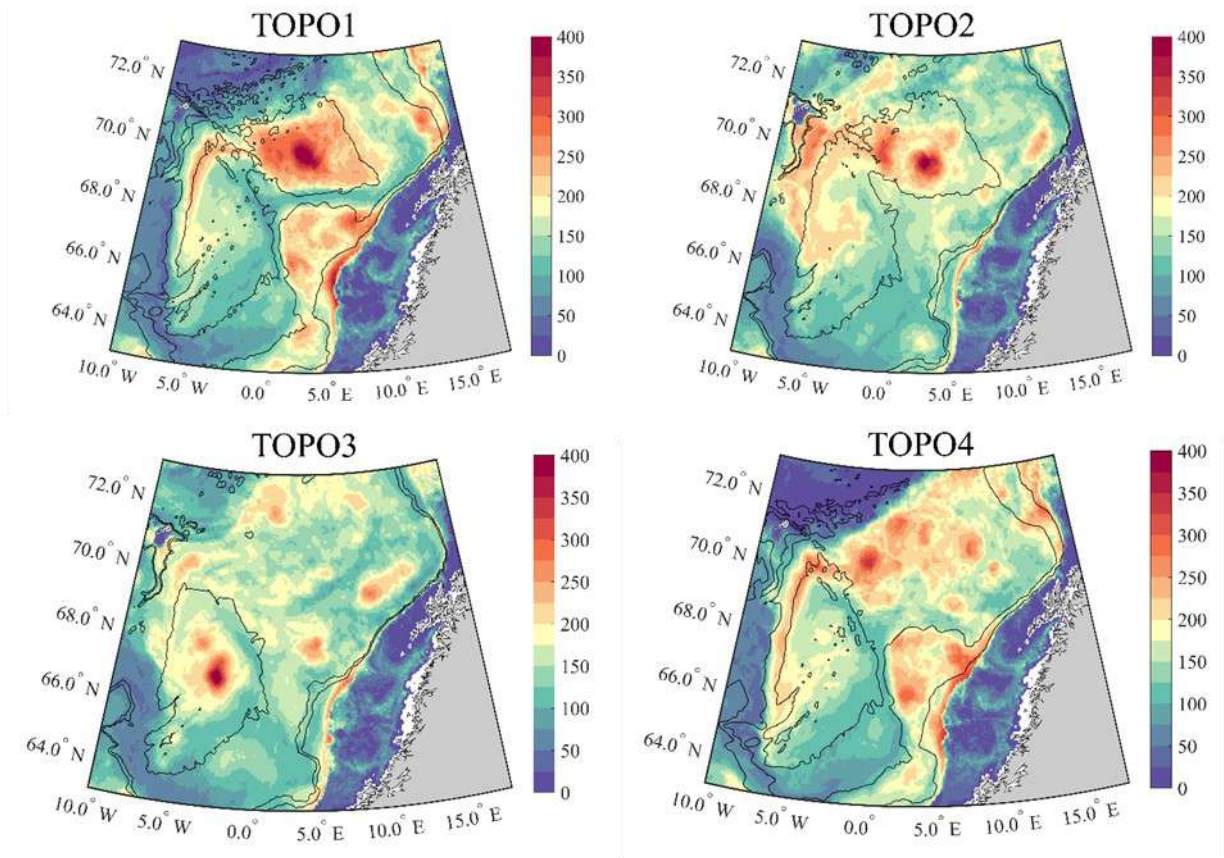


Figure 1.25. Spatial distribution of the MLD (m) in February, averaged over 1993-1997 in experiments TOPO1-4.

Eddy kinetic energy in TOPO experiments.

In the TOPO1 experiment, the maximum EKE (more than $400 \text{ cm}^2\text{c}^{-2}$) was recorded in the central part of the Lofoten Basin and near the Norwegian continental slope (Figure 1.26). Significant EKE values are observed above the Voring Plateau, whereas in the Norwegian Basin EKE is insignificant and does not exceed $50 \text{ cm}^2\text{c}^{-2}$. The TOPO2 experiment shows an increase in eddy activity over the Norwegian continental slope, especially in the eastern and southern parts of the Norwegian Sea (Figure 1.26). A slight increase in EKE is also observed on the periphery of the Norwegian Basin and in the western part of both basins. In the TOPO3 experiment, the EKE maximum is observed in the center of the Norwegian Basin, in the eastern part of the Lofoten Basin, and along the Norwegian continental slope. It is noticeable that the eddy activity in the central part of the Lofoten Basin is significantly lower compared to similar values in the TOPO1 and TOPO2 experiments. In TOPO4,

values above $300 \text{ cm}^2\text{s}^{-2}$ are recorded only in the eastern part of the Lofoten Basin. Based on the results of numerical experiments, we can state that the presence of a topographic depression in the center of the Lofoten Basin, as well as a barrier between the basins, contributes to an increase in EKE in the Lofoten Basin and a decrease in EKE in the Norwegian Basin. On the other hand, in the absence of a boundary between basins, vortices can freely spread into the Norwegian Basin and form a quasi-permanent anticyclone there, which stands out as a region of maximum values in the EKE field. However, the presence of a boundary in the form of the Voring Plateau and the Helgeland ridge (TOPO4 experiment) helps to reduce the EKE values in the center of the Norwegian Basin and prevents the formation of an eddy in it. Thus, the TOPO1-4 experiments indicate the key importance of bottom topography for the eddy mesoscale dynamics of the Norwegian Sea.

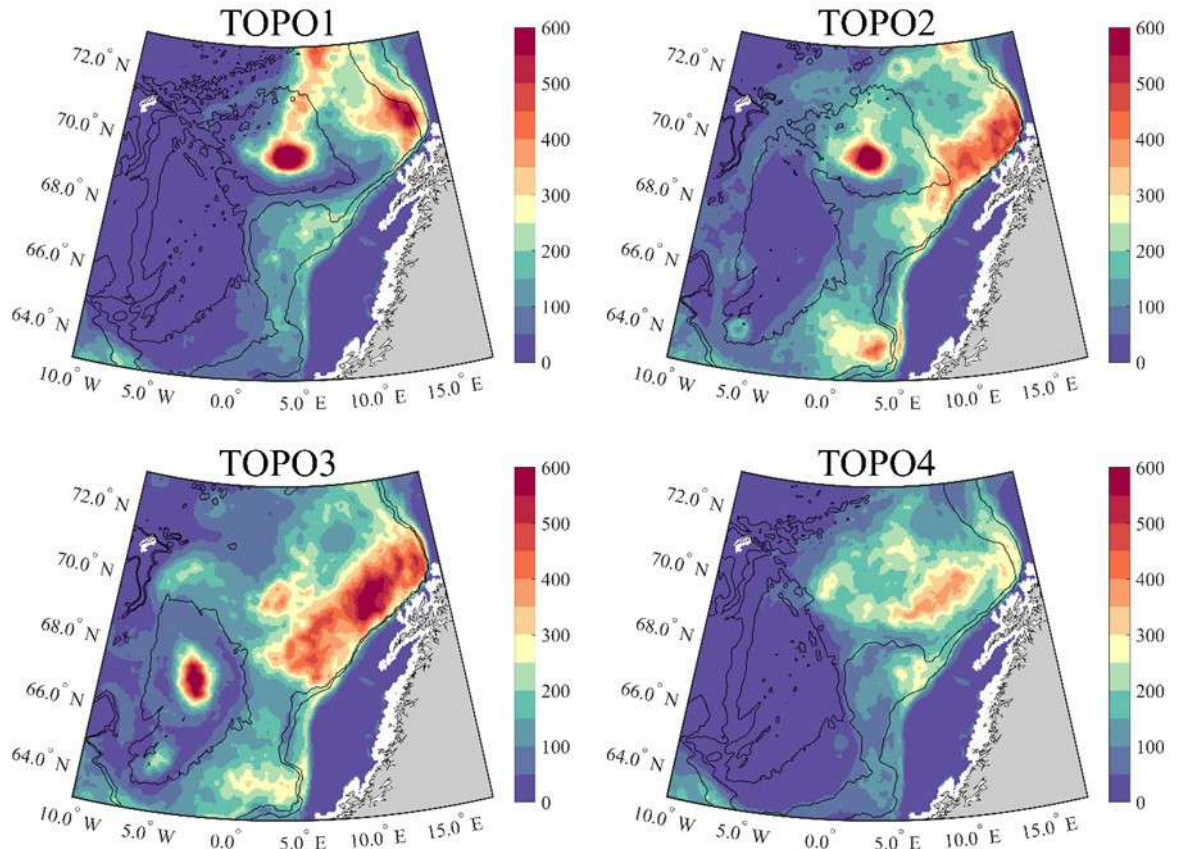


Figure 1.26. Spatial distribution of EKE (cm^2s^{-2}) in February, averaged over 1993-1997 in experiments TOPO1-4.

The relationship between vortex activity and convection

A comparison of Figures 1.25 and 1.26 shows that the regions with the greatest MLD mostly coincide with the areas of maximum EKE values. The fact is that active vertical mixing in eddies has a significant effect on convective processes, therefore, the greatest MLD in the Norwegian Sea are localized in eddies characterized by increased values of eddy kinetic energy. In TOPO1, a depth of more than 400 m was recorded in the LV area, where the maximum EKE is also located (about $600 \text{ cm}^2\text{s}^{-2}$). The northeastern part of the Lofoten Basin and the Voring Plateau are also distinguished by both the MLD and the EKE (Figures 1.25 and 1.26). On the other hand, an increase in the MLD to 300 m in the area of the Mona Ridge and along the western part of the periphery of the Norwegian Basin does not manifest itself in the

EKE field. This contradiction can be explained by the fact that there are other types of vertical mixing that are not related to mesoscale eddies. One of these types is slope convection, which can also occur together with convection in eddies (Kämpf et al., 1999). All this leads to the fact that the areas with increased values of the MLD have a larger area compared to the areas of significant EKE values (Figures 1.25 and 1.26). In the TOPO2 experiment, the spatial distribution of the MLD and EKE maxima is similar. They are localized in the LV area, as well as in the eastern part of the Lofoten Basin along isobaths 1000 and 2000 m. On the other hand, an increase in the depth of the MLD in the Norwegian Basin and in the western part of the Lofoten Basin does not manifest itself in any way in an increase in EKE. In TOPO3, the maximum of EKE and MLD is typical for the central part of the Norwegian Basin, while minima of both parameters are observed in the southern and eastern parts. It is worth noting that a significant increase in eddy activity in the eastern part of the Lofoten Basin near the Norwegian continental slope does not lead to an increase in the MLD. In the TOPO3 and TOPO2 experiments, the MLD values are lower compared to the TOPO1 experiment, which used the real topography of the seabed. This may be due to slope convection, favorable conditions for which are created when the topography changes smoothly, rather than abruptly, as in TOPO2 and TOPO3. The change in the topography of the continental slope contributes to the growth of EKE in the southern part of the Norwegian continental slope, but it does not affect the depth of the EKE in any way.

The main conclusions

Using the results of the MITgcm model, we analyzed a series of topographic experiments, each of which set a different topography of the Norwegian Sea. The following conclusions were obtained: (1) a flat abyssal plain with a depression in the central part is a necessary condition for the formation of a quasi-permanent Lofoten Vortex in the Norwegian Sea; (2) The existence of a boundary between the Norwegian and Lofoten Basins (the Voring Plateau and the Helgeland ridge) plays an important role in the formation of the LV and its permanent presence in the

Lofoten Basin. In the absence of a boundary, the formation of a quasi-permanent anticyclone occurs in the Norwegian Basin. As shown in Shchepetkin's numerical experiments, the existence of cyclonic circulation on the periphery of the idealized basin, as well as the formation of an anticyclonic eddy in its central part, is associated with the nature of the seabed topography (Shchepetkin, 1995). Our experiments also confirm these conclusions. A quasi-permanent anticyclonic LV is formed only when the basin is limited from all sides. Moreover, Benilov theoretically confirmed using a two-layer quasi-geostrophic model that the topography of the seabed determines the stability of the anticyclone formed in the TOPO1 and TOPO2 experiments (Benilov, 2005). In the absence of a boundary between the two basins of the Norwegian Sea, a quasi-permanent eddy is formed not in the Lofoten Basin, but in the Norwegian Sea. Mesoscale eddies are generated mainly due to the dynamic instability of the NwASC (Isachsen, 2011; 2015; Volkov et al., 2015), move westward through the Lofoten Basin and reach the Norwegian Basin, where an anticyclone forms due to the bowl-shaped shape of the basin (TOPO3 experiment). At the same time, the eddy formed in the Norwegian Basin in the TOPO3 experiment is weaker than the LV formed in TOPO1 and TOPO2.

Another possible mechanism influencing the intensity and stability of a quasi-permanent anticyclone is deep winter convection (Alexeev et al., 2016; Travkin and Belonenko, 2020; Fedorov et al., 2019). The stability of the eddy is associated with a periodic increase in horizontal gradients of potential vorticity along its boundaries (Bloschkina and Ivanov, 2016; Bashmachnikov et al., 2017b). Thus, the topography of the Lofoten and Norwegian basins has a positive effect on the development of convection in the winter and spring period. The unevenness of the seabed of the Norwegian Basin negatively affects the intensity of convection (TOPO4 experiment), while the flat seabed of the Lofoten Basin has a positive effect on increasing the depth of the ice. It was found that the MLD in the Norwegian Basin is much lower on average, compared with similar estimates for the Lofoten Basin. In addition, convection reaches its maximum development in February and then weakens slightly in March.

The spatial distribution of the MLD demonstrates the presence of maximum intensity in the LV region (experiments TOPO1 and TOPO2). When the topography of the Lofoten Basin changes, the areas of greatest convection development shift to the western part of the basin, to the area of the Voring Plateau and the continental slope (TOPO4) or to the central part of the Norwegian Basin (TOPO3). The significant MLD in the area of the Voring Plateau decreases significantly with its removal (experiments TOPO2 and TOPO3). A similar increase in the MLD in the area of the Voring Plateau is analyzed in (Nilsen and Falck, 2006), where the authors associate the increase in the thickness of the MLD with an increase in the residence time of Atlantic waters in this area due to the divergence of the branches of the Norwegian current.

The topographic isolation of the Lofoten Basin and the deepening in its central part leads to the formation of an area of increased eddy activity in the center of the basin and its almost complete absence in the Norwegian Basin (TOPO1 and TOPO2). Winter convection is accompanied by intense horizontal eddy mixing in a wide range of scales. The results of our work confirm the idea that winter convection with a spatial scale of about 1 km is closely related to mesoscale eddies with sizes from 5 to 50 km (Killworth, 1983).

CHAPTER 2. NORTHWESTERN AND SOUTH PACIFIC

2.1. Data

GLORYS12V1 and ETOPO1

As in the previous chapter, data from the global ETOPO1 relief model are used for this study area, as well as daily and monthly average data on temperature, salinity, sea surface height, and u and v components of current velocities from the global ocean reanalysis GLORYS12V1 for the period 1993-2021.

Mesoscale Eddy Trajectory Atlas META3.2 DT

Mesoscale Eddy Trajectory Atlas META3.2 DT available at (<https://www.aviso.altimetry.fr/en/data/products/value-added-products/global-mesoscale-eddy-trajectory-product/meta3-2-dt.html>). It is an improved and updated version of the Mesoscale Eddy Trajectory Atlas used in the previous chapter. So, in the new version, altimetric information is received from all time-available satellites, which allows you to get more accurate information about the height of the sea surface. In addition, the authors have improved the algorithms for filtering fields of absolute dynamic topography, as well as detecting eddies (Pegliasco et al., 2022). In the new version, mesoscale cyclones and anticyclones are divided into long-lived (life span of more than 10 days) and short-lived (life span of less than 10 days) vortices. The time period considered in our work covers 29 years: from January 1, 1993 to December 31, 2021.

2.2 Methods

Dispersion equation for barotropic topographic waves

Rossby waves belong to the class of gradient eddy waves, and their propagation obeys the law of conservation of potential vorticity.:

$$\frac{d_h}{dt} \left(\frac{\zeta+f}{H} \right) = 0,$$

where $\frac{d_h}{dt} = \frac{\partial}{\partial t} + U \frac{\partial}{\partial x} + V \frac{\partial}{\partial y}$; x and y – zonal and meridional variables in a rectangular coordinate system; t – time; U and V – zonal and meridional components of the velocity; f – Coriolis parameter; H – depth; ζ – relative vorticity ($\zeta = \frac{\partial V}{\partial x} - \frac{\partial U}{\partial y}$). In the shelf area, potential vorticity occurs with increasing depth in the direction perpendicular to a large-scale topographic irregularity (LeBlond and Mysak, 1981). Let us apply the theory of estimating terms in the dispersion relation for Rossby waves on a shear flow, taking into account topography, described in detail in (Gnevyshev et al., 2019; 2021; Gnevyshev et al., 2022). Let's introduce an equation for the so-called "efficient" β -эффекта (β^*):

$$\beta^* = \beta \cos \theta - U_{\eta\eta} - \frac{fH_{\eta}}{H} + \frac{U_{\eta}H_{\eta}}{H},$$

where $\beta = \frac{df}{dy}$; A coordinate system with an angle rotation is used for the Kuril-Kamchatka Trench area θ relative to the coordinate system (x, y) ; η – the ordinate axis of the rotated system. Formulas for the transformation of the coordinate system are given in (Gnevyshev et al., 2022). The terms of the equation describe various mechanisms affecting the propagation of mesoscale cyclones and anticyclones. The first term describes the β -effect; the second term is the meridional gradient of the zonal shift in the flow velocity; the third term denotes the topographic factor, and the fourth term is responsible for the combined effect of flow and topography.

2.3 Topographic waves of the Kuril trench.

Figure 2.1 shows the bathymetry of the South Kuril region. It can be noted that the relief of this area is characterized by an area of the shelf, a deep-sea trough, as well as a small topographic elevation above the trough. The shelf area abruptly turns into the continental slope that makes up the inner part of the Kuril Trench. At the same time, the outer slope of the trough has a gentler slope. Further, the features of wave dynamics will be considered for the following zones of the South Kuril region: 1) the shelf, where the depth increases slightly; 2) the continental slope (the inner part of the trough), where the depth increases sharply; 3) the outer (oceanic)

part of the trough, where the depth decreases (the derivative of the depth changes its sign); 4) the area of topographic elevation east of the trough (open ocean), while to the west of the elevation the depth decreases, and from the east side increases (Fig. 2.1). East of the elevation, the depth varies slightly, so we can assume that it is constant.

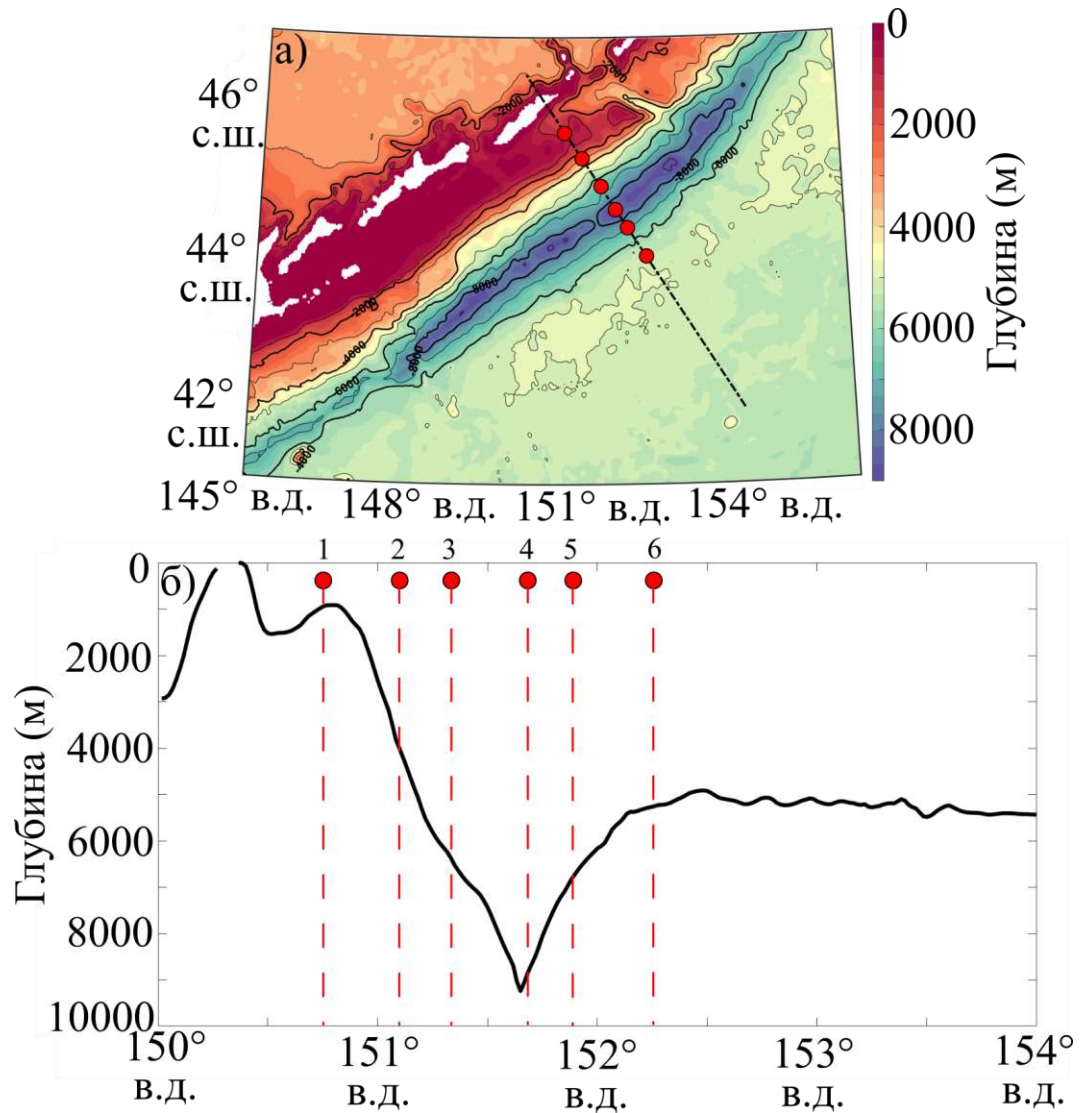


Figure 2.1. Bathymetric map of the Kuril Trench according to ETOPO1 data, the dotted line shows the transverse section (a); the topographic profile along the section (b). The points where the terms of the effective β -effect were calculated are marked in red.

A system of vortices moving on the shelf forms shelf waves, which, when moving, leave the shore on the right (Belonenko et al., 2018b; Sandalyuk et al.,

2020). The work (Gnevyshev et al., 2023b) notes that shelf waves are represented by coherent structures in the form of conical circles, and the maximum speeds of shelf currents are determined only by latitude (dependence on the Coriolis parameter) and do not depend on the steepness of the topography. At the same time, with a positive slope of the relief (decreasing depths to the north), the group and phase velocities increase, while with negative ones they decrease (Gnevyshev et al., 2024). In the trough region, the movement of inhomogeneities in the level field is associated with the propagation of trough waves (LeBlond and Mysak, 1981; Efimov et al., 1985; Gnevyshev et al., 2023a). In the first case, the shelf plays the role of a waveguide of offshore waves, contributing to the transfer of energy with almost no loss, whereas in the second case, the role of the waveguide is performed by the trough.

The study of shelf waves first began with the work of Buchwald and Adams (1968). In turn, the pioneering work of Mysak and colleagues (Mysak et al., 1979) began the study of trench waves. In some works (for example, Efimov et al., 1985), the latter are considered as an analogue of Kelvin double waves, while in the work of Mysak and colleagues (Mysak et al., 1979) Such a term is not used at all, and the monograph (LeBlond and Mysak, 1981) notes that Kelvin double waves have not been detected in marine conditions, although they may exist under certain laboratory experimental conditions. For the first time, the term "Kelvin double waves" was introduced in works (Longuet-Higgins, 1968a, b). These waves represent the limiting case of trough waves with the trough width tending to zero. Following the terminology of the work (Mysak et al., 1979), in our work we will refer to those waves that propagate along the trough as trough waves. Thus, the subject of this part of our study is the low-frequency waves of the Kuril shelf and the Kuril Trench.

Topographic waves in the South Kuril region propagating along the slopes (points 1-4) are influenced by various factors, including shear currents and the β -effect. We show that it is the topographic factor that is the most important and exceeds the contribution of other terms by several orders of magnitude. Figure 2.1 shows the bathymetry of the study area. It can be noted that in the center of the Kuril

trench the depths exceed 9000 m, the greatest depth is 9717 m. The angle between the main axis of the trough and the latitude is $\theta = 49.35^\circ$. In Figure 2.2, it can be seen that the average current velocities in the area of the Kuril trench are 15-20 cm/s, while the current vectors are directed along the isobaths to the northeast. In the southwestern part of the study area, where the quasi-stationary anticyclonic eddy is located, as well as in the northeastern part of the trough, the direction of the vectors demonstrates rotational movements in the vortices (Samko et al., 2007).

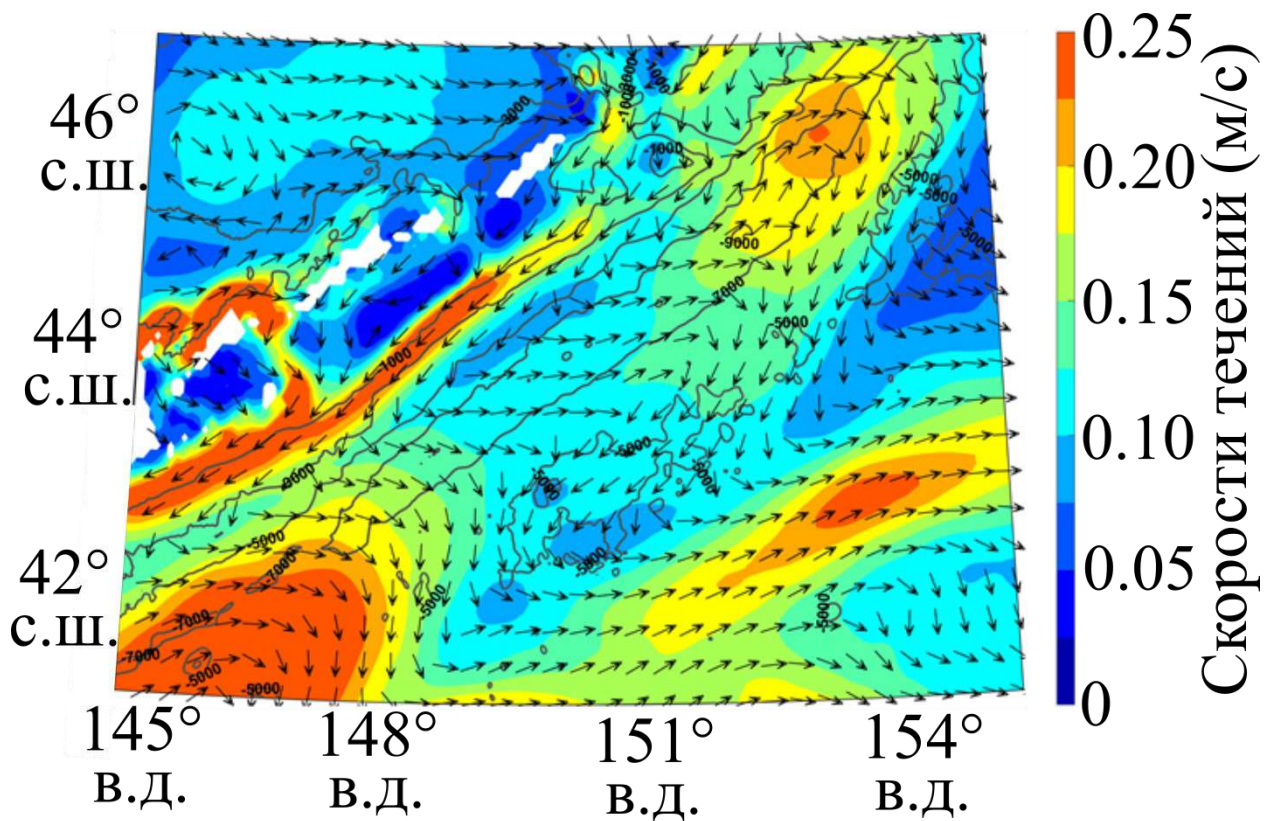


Figure 2.2. Current velocities on the sea surface, averaged over 1993-2019, according to the global ocean reanalysis GLORYS12V1. Black lines show isobaths.

First, using the formula for the effective β -effect, we will give a comparative assessment of the terms of the equation for the Kuril trench. Table 2.1 shows the estimates of the terms of the β^* -effect. It can be noted that in all points the second (topographic) factor significantly dominates, and its contribution exceeds the

contribution of the other factors by several orders of magnitude. This indicates that the analysis of waves in the South Kuril region can be limited only by the influence of topography, neglecting other factors.

Table 2.1. Estimates of terms β^* in points 1–6 (see fig. 2.1). The data is normalized to 10^{-11} .

Point	Depth (m)	$\beta \cdot \cos\theta$	$U_{\eta\eta}$	$\frac{fH_{\eta}}{H}$	$\frac{U_{\eta}H_{\eta}}{H}$
1	948	1,042	19,23	59,72	-0,63
2	3340	1,042	-9,36	-293,37	-5,98
3	6086	1,049	30,45	-111,66	0,44
4	9135	1,055	-1,72	-4,43	0,0042
5	6870	1,062	-3,58	89,73	0,64
6	5297	1,068	-1,24	20,30	-0,35

Figure 2.3 shows the distribution of mesoscale cyclones and anticyclones per 0.1° latitude and 0.2° longitude cell in the study area. It can be noted that the distribution of eddies in the region is uneven: anticyclones are concentrated on the shelf and on the offshore side of the trough, while cyclones are localized on the inner side of the trough, as well as near the topographic uplift south-east of the trough.

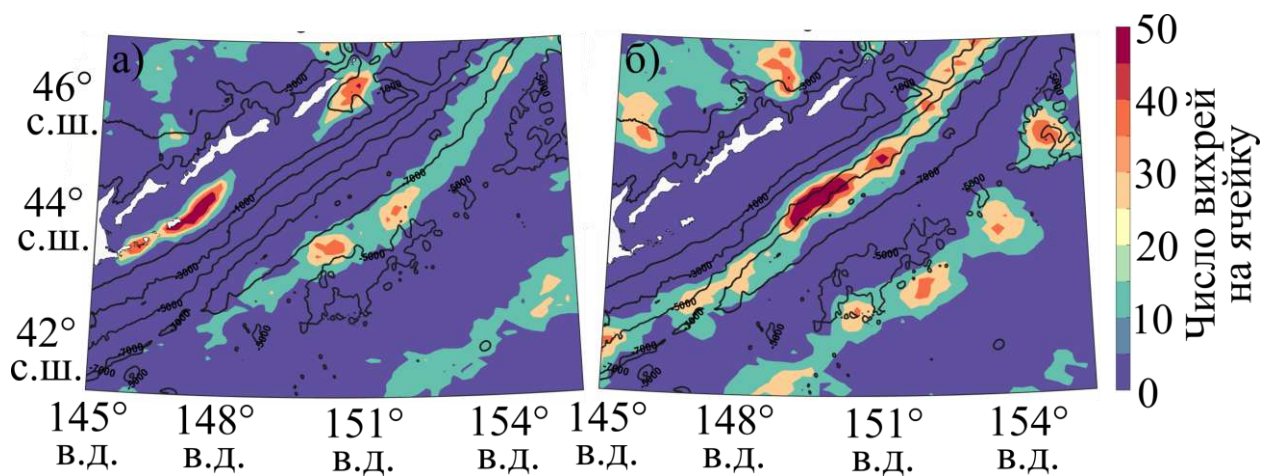


Figure 2.3. The number of mesoscale eddies per cell (0.1° in latitude by 0.2° in longitude) for the period from 01.01.1993 to 02.08.2021: a — anticyclones; b — cyclones. The black lines show isobaths.

Table 2.2 shows the main parameters of both long-lived and short-lived anticyclones and cyclones. It is noticeable that the number of cyclones is more than 2 times the number of anticyclones, while the life expectancy of anticyclones is almost 2 times the life expectancy of cyclones. This feature may be related to the cyclone-anticyclone asymmetry associated with the nonlinear properties of eddies. So, in cyclones, the velocity rotor is parallel to the vector of the vertical component of the Earth's rotation, while in an anticyclone it is antiparallel. This contributes to the fact that in an anticyclone the scalar nonlinearity balances the dispersion, whereas in a cyclone the nonlinearity and dispersion have the same signs, therefore they cannot be mutually compensated (Nezlin, 1986). The radii and areas of cyclones slightly exceed those of anticyclones, while the amplitudes of anticyclones are almost 4 times higher than those of cyclones (Table 2.2). Also, the orbital velocities of long-lived anticyclones are more than 2 times higher than those of cyclones. All this indicates that in the studied area, anticyclones are more intense and have greater relative and potential vorticity compared to cyclones. The average velocities of cyclones and anticyclones are close to 4-7 cm/s, while cyclones have high speeds.

Table 2.2. Average estimates of anticyclone (AC) and cyclone (C) parameters in the Kuril region.

	AC		C	
	t<10 days	t>10 days	t<10 days	t>10 days
Amount	66	209	131	422
Life span (days)	4	107	4	54
Amplitude (cm)	1,98	17,07	1,74	4,40

Radius (km)	33,63	47,43	34,96	48,79
Area (km ²)	2874	6805	3170	7052
Orbital velocity (cm/s)	9,62	31,84	9,88	14,56
Velocity of eddy (cm/s)	5,33	4,13	6,26	7,69

Figure 2.4 shows the trajectories of long-lived anticyclones and cyclones in the South Kuril region according to the META 3.2 DT. It can be noted that the trajectories of cyclones and anticyclones follow different and almost non-intersecting parallel paths. In Figure 2.5, the color shows the direction of movement of cyclones and anticyclones: blue – if the vortices are moving north, red – when the vortices are moving south. In addition to the fact that cyclones and anticyclones move along different "paths", their directions of movement also differ. So, the anticyclones on the shelf (1) are moving southwest, and the anticyclones on the offshore side of the Kuril Trench (3) are moving in a southwesterly direction. On the other hand, cyclones are moving along the slopes (2 and 4) in a southwesterly direction (Fig. 2.5). In other words, cyclones and anticyclones form 4 parallel "paths", while shallow water (shore) always remains to the right of the direction of movement. In the works of Gnevyshev and co-authors (Gnevyshev et al., 2019; 2021; Gnevyshev et al., 2022), it was found that the phase velocity of propagating topographic waves is proportional to $\alpha = H_\eta/H$:

$$c = \frac{\omega}{k} = \frac{f\alpha}{k^2 + l^2}$$

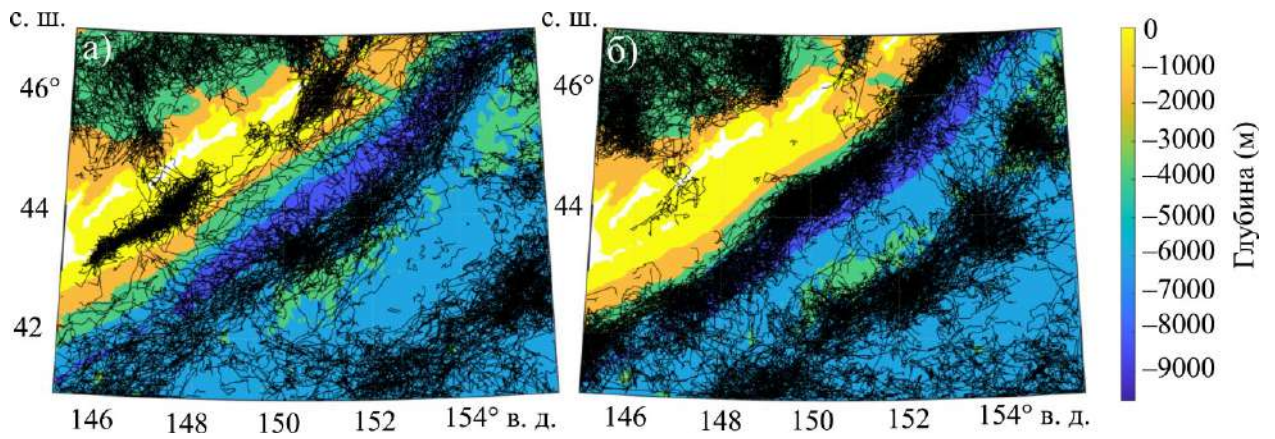


Figure 2.4. Trajectories of long—lived eddies in the Kuril region according to META3.2 DT for the period from 01.01.1993 to 02.08.2021: a — anticyclones; b — cyclones.

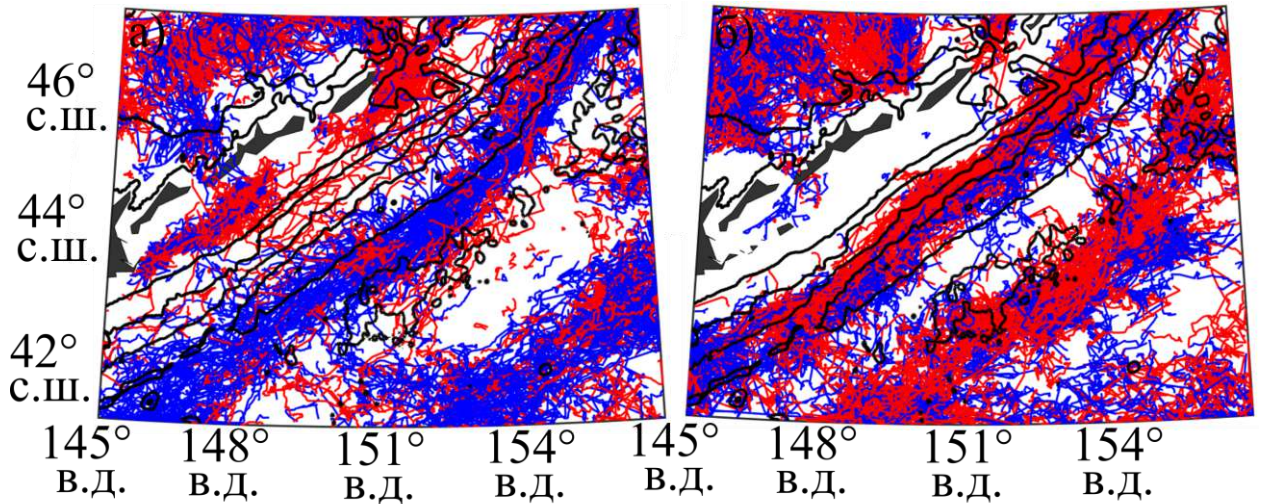


Figure 2.5. Trajectories of long—lived vortices in the Kuril region according to META3.2 DT for the period from 01.01.1993 to 08.22.2021: a — anticyclones; b — cyclones.

Thus, in the South Kuril region, mesoscale cyclones and anticyclones are divided into four groups, each of which is dominated by a specific direction: either northeast or southwest. At the same time, each group is mainly represented by either cyclones or anticyclones. This fact has never been mentioned before. Figure 2.6 shows the tracks for one representative from each group for greater clarity.

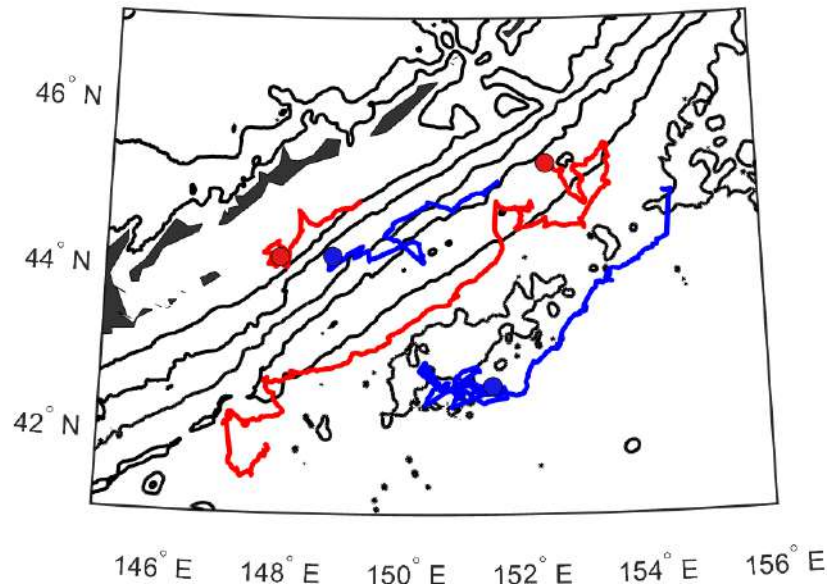


Figure 2.6. Separate tracks of cyclones (blue) and anticyclones (red). The dots show the places of eddy dissipation, and the black lines show isobaths.

Vertical structure and velocity of trench waves

It is worth noting that moving cyclones and anticyclones "feel" the change in topography at great depths, i.e. they have a pronounced barotropic component. For example, Figure 2.7 shows an anticyclone on the offshore side of the Kuril Trench moving to the northeast. It can be seen that the center of this anticyclone is confined to an isobath of 7000 m, while the depth difference on the slope lies in the range from 5000 to 9000 m. It can be seen that the core of the anticyclone is located in a layer up to 1000 m (Fig. 2.7 b). In this case, the dynamic signal of the eddy can be traced all the way to the bottom, because the eddy moves along the isobath. Despite the fact that the anticyclone is localized in the offshore part of the Kuril trench to a depth of 1000 m, and seemingly independent of the changing topography at depths of more than 5000 m, the eddy "feels" the topographic slope, thereby moving along the isobath. This suggests that the eddy is a manifestation of a larger-scale phenomenon, in this case, a group of trough waves characterized by a barotropic component. Such chains of cyclones and anticyclones have an organized structure and move along isobaths in strictly defined directions, although large-scale topography changes occur at depths of more than 5,000 m. All of the above indicates

that we are dealing not just with mesoscale cyclones and anticyclones, but also with the manifestation of topographic waves. In Figures 2.4-2.7, one can see the movement of shelf and trough waves represented by anticyclones, as well as topographic waves on the inner slope of the Kuril trench and along the topographic uplift behind the trench.

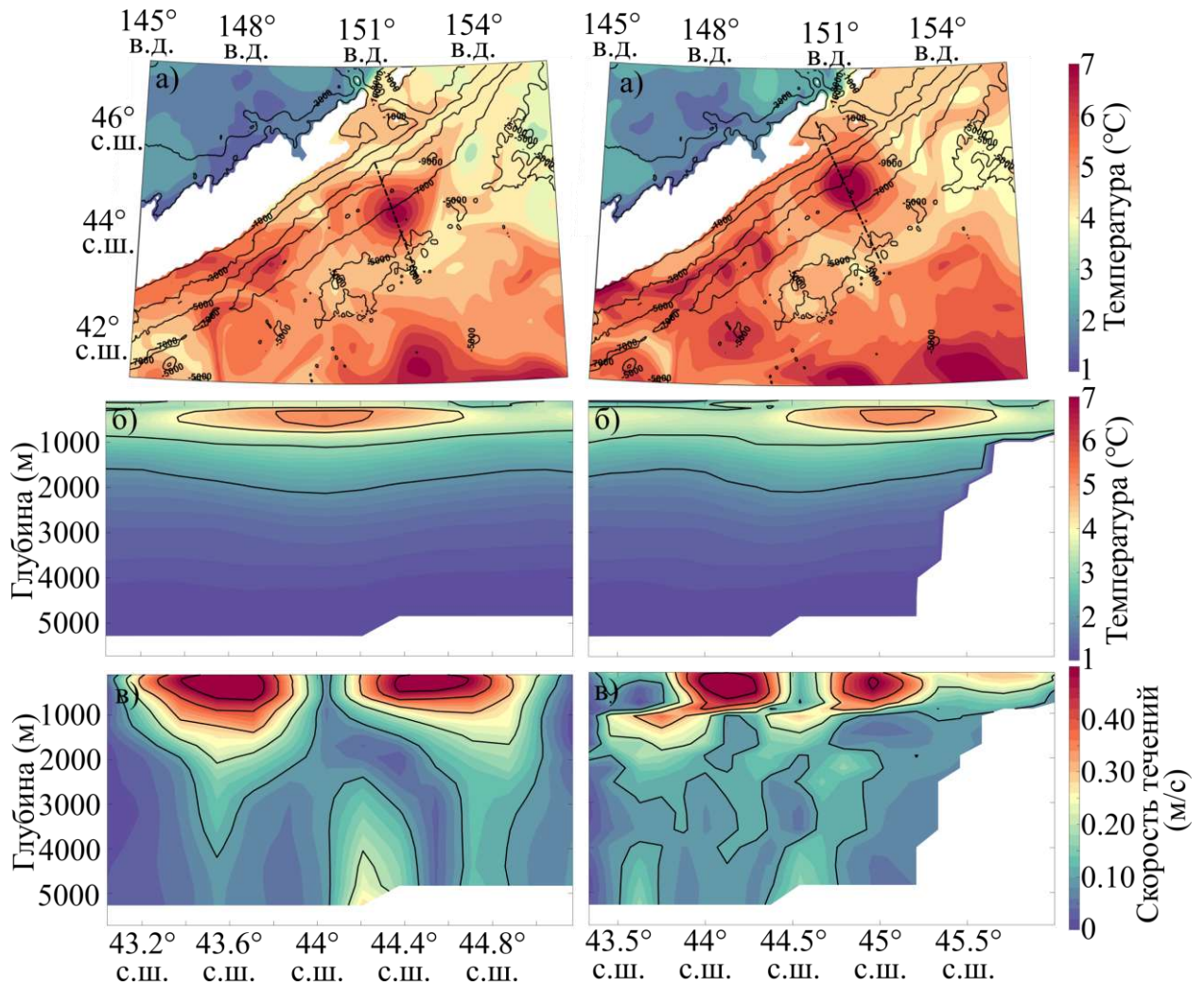


Figure 2.7. Anticyclonic eddy in the Kuril Trench in the temperature (a), vertical temperature sections through the center of the eddy (b) and orbital velocity (c) for June 1 (left) and July 1 (right) 2019.

Figure 2.8 shows two-dimensional spectra of trench waves. Their calculation was carried out using the 2D-FFT procedure in the MatLab environment. It is noticeable that the waves have lengths of more than 500 km and periods exceeding

one year. The speed of the waves varies in a wide range from a few centimeters per second to several tens of centimeters per second.

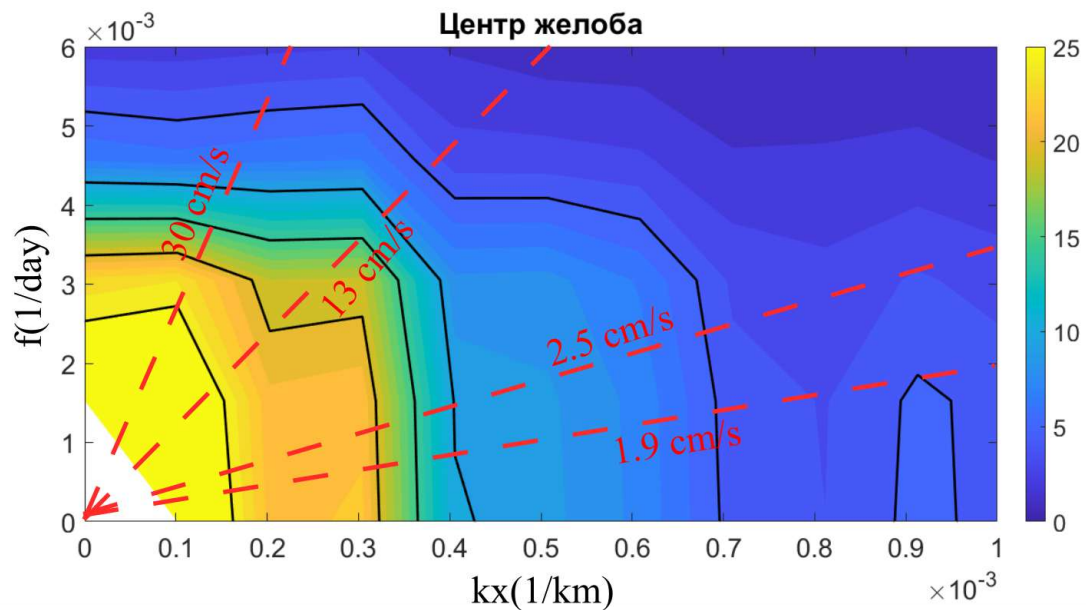


Figure 2.8. 2D-FFT spectra of low-frequency waves in the Kuril region. The dotted line shows the phase velocities of the waves.

Conclusions

Probably, due to the fact that anticyclones are characterized by large amplitudes and orbital velocities, compared with cyclones, in earlier works only anticyclones are associated with topographic waves in the South Kuril region. Thus, the movement of anticyclones on the shelf (1) is associated with offshore waves (Efimov et al., 1985; Belonenko, 2012), and the movement of anticyclones on the offshore side of the trough with trough waves (Efimov et al., 1985). However, as can be seen in Figures 2.3-2.6, trough and shelf waves do not exhaust the entire spectrum of topographic waves in the South Kuril region. In earlier sources, the movement of cyclones along the inner side of the Kuril trench (2) and the seaward topographic uplift beyond the trench (4) was not mentioned at all. Cyclones, whose number is more than twice the number of anticyclones, were not given any attention at all, although they also make a significant contribution to the mesoscale dynamics of the South Kuril region (Table 2.2).

Cyclones may have been excluded from view due to the fact that their amplitudes and orbital velocities are much lower than anticyclones, as a result of which the latter are better visible on satellite images. Thus, observations from meteorological satellites record chains of only anticyclones, whereas cyclones are practically invisible on them (Bulatov and Lobanov, 1983). In his work, S. V. Prants also considers only anticyclones as Kuril eddies (Prants, 2021). In our study, we want to draw attention to the fact that when studying topographic waves, both anticyclones and cyclones should be taken into account, as well as all types of large-scale topographic irregularities in the South Kuril region, which are waveguides.

It has been established that in the South Kuril region there are four systems of topographic waves moving along isobaths. These waves manifest themselves as chains of cyclones and anticyclones. Thus, anticyclones move along the shelf in the form of shelf waves in a southwesterly direction, and along the outer part of the trough in a northeasterly direction. Cyclones move along the inner part of the trough and along the topographic elevation to the southwest. In all cases, cyclones and anticyclones leave the coast on the right.

An analysis of the contribution of various components to the β^* – effective β -effect showed that the contribution of topography to the propagation of these waves exceeds the contribution of other components by several orders of magnitude. A similar trend is observed in other areas of the northwestern Pacific, for example, in the area of the Aleutian Trench (Khudyakova et al., 2023). It was found that cyclones dominate among long-lived eddies with a lifespan of more than 10 days, since their number is more than twice as high as that for anticyclones. On the other hand, anticyclones are more stable structures and, on average, have a larger amplitude, orbital velocity, and twice the lifespan of cyclones.

Despite the fact that the eddy cores are localized in the upper layer up to 1000 m, the topographic waves of the South Kuril region "feel" the topographic slope located at depths of more than 5000 m, and propagate following isobaths. This feature indicates a pronounced barotropic component characteristic of the wave nature of the phenomenon under study. The lengths of these waves can exceed 500

km, and the periods are one year; the speed of the waves varies from several cm/s to several tens of cm/s.

2.4. Variability of mesoscale eddies of the South Pacific

The purpose of this part of the dissertation research is to describe the propagation features and identify the parameters of mesoscale cyclones and anticyclones based on altimetric data. The area of our study is the water area adjacent to the coast of South America: 20-50° S, 70-120° W.

Based on the META 3.2 DT, 35127 long-lived (life span of more than 10 days) anticyclones and 39739 cyclones were detected in the study area in 1993-2020. Figure 2.9 shows the number of mesoscale eddies in this region per $1 \times 1^\circ$ cell in latitude and longitude for 1993-2020. It can be noted that the largest number of eddies of both types is generated in the shelf area, as well as on the slopes of the Peruvian and Chilean trenches. Obviously, this feature is associated not only with the instability of the currents, but also with the influence of topography and upwelling. In the area near the coast of South America, the number of anticyclones is maximum (more than 120 per cell) in the entire coastal region, while cyclones are concentrated mainly in the area of 38-48° S. It is noticeable that significantly fewer eddies form in the band of 30-40° S, compared with the area of 40-50° S. This difference can be explained by the lower impact in the first region of the subtropical anticyclonic cycle (Fig. 2.9). This difference is also due to the influence of the ACC, the most powerful current in the Global Ocean, which, according to some sources, has a flow rate of 144 Sv ($1 \text{ Sv} = 10^6 \text{ m}^3 \cdot \text{s}^{-1}$) (Cunningham et al., 2003). The northern boundary of the ACC in the South Pacific runs approximately parallel to 40° S, so the increase in the number of cyclones and anticyclones south of this latitude can be explained by the influence of the ACC (Belonenko et al., 2020a). In the work (Gnevyshev et al., 2019), the process of eddy formation in an ACC jet is interpreted in terms of the interaction of Rossby waves with the ACC. It is known that Rossby waves can manifest themselves as vortices that tend to move in a westerly direction (Nezlin, 1986). However, when interacting with the ACC, the direction of their

movement sometimes changes to the opposite due to the fact that the contribution of the term associated with the meridional shift of the zonal component of the flow exceeds the influence of the beta effect. This causes the eddies recorded in META3.2 DT to move eastward or at least slow down their movement westward (Travkin et al., 2024a). This explains the increase in the number of eddies in the area of the ACC in Fig. 2.9. It is worth noting that in the region of 40-50 S, the number of cyclones significantly exceeds the number of anticyclones. This trend is related to the peculiarities of the ACC meandering.

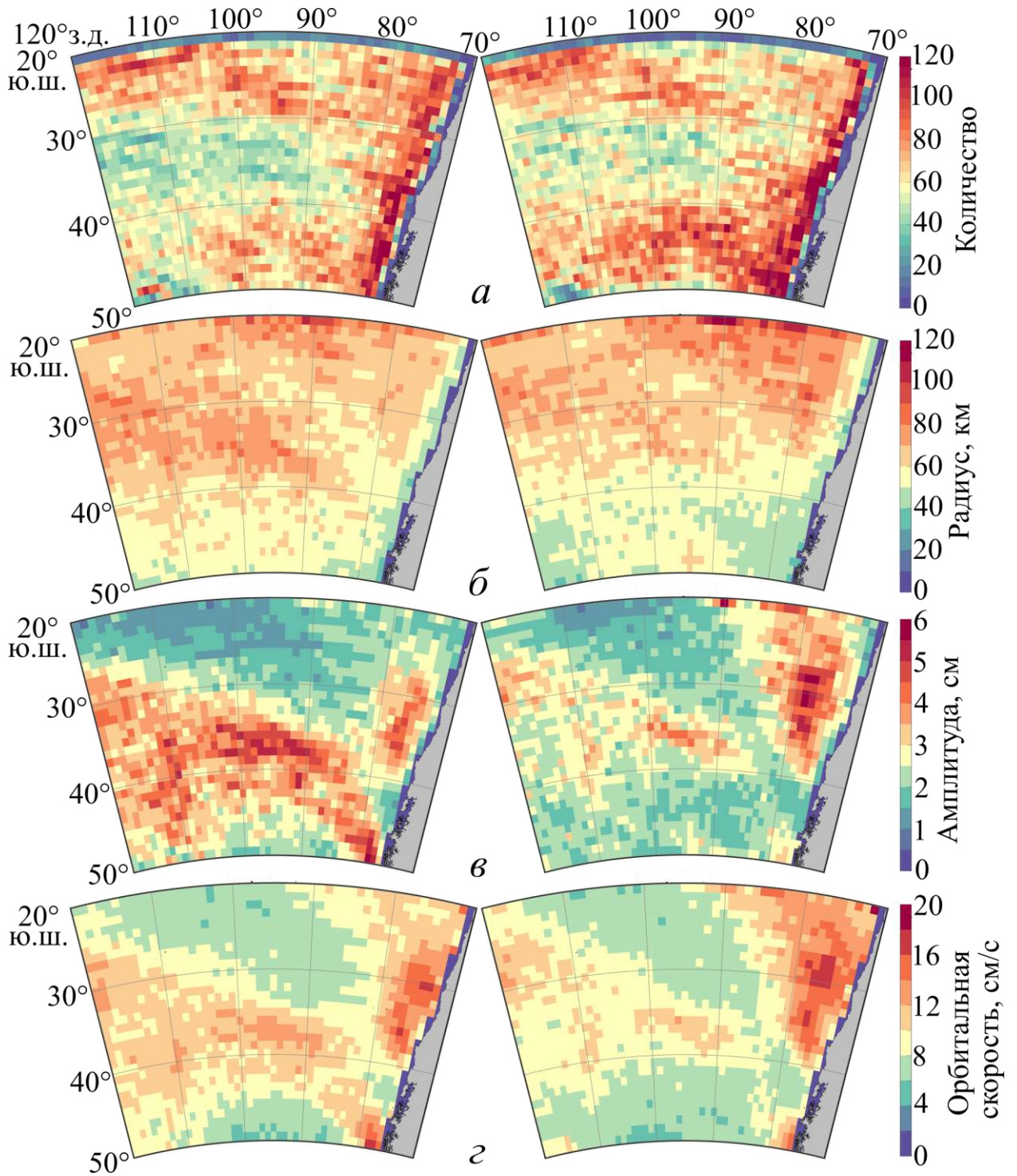


Figure 2.9. Number (a), radius (b), amplitude (c), orbital velocity (d) of anticyclones (left) and cyclones (right) per $1 \times 1^\circ$ latitude and longitude cell for 1993-2020.

Despite the fact that the minimum number of eddies is recorded in the 30-40 °S, the eddy energy in this area is maximum and can reach $120 \text{ cm}^2\text{s}^{-2}$ per grid cell (Fig. 2.10). This is explained by the fact that the eddies located in this region are

characterized by their maximum amplitude, radius, and orbital velocity (Fig. 2.9). On the other hand, the average kinetic energy of MKE is much lower than EKE. This feature indicates that in the time scale range under consideration, it is the eddy component that makes the greatest contribution to variability. The vertical profiles clearly show a significant dominance of EKE over MKE in the layer from 0 to 550 m, as well as a sharp decrease in EKE and MKE with increasing depth (Fig. 2.10). The maximum values of EKE and MKE are fixed on the sea surface, while the greatest difference between EKE and MKE is typical for the horizon of 30 m. At a depth of about 500 m, the MKE values become close to zero, while the EKE value decreases by more than two times compared to the values at the surface (Fig. 2.10).

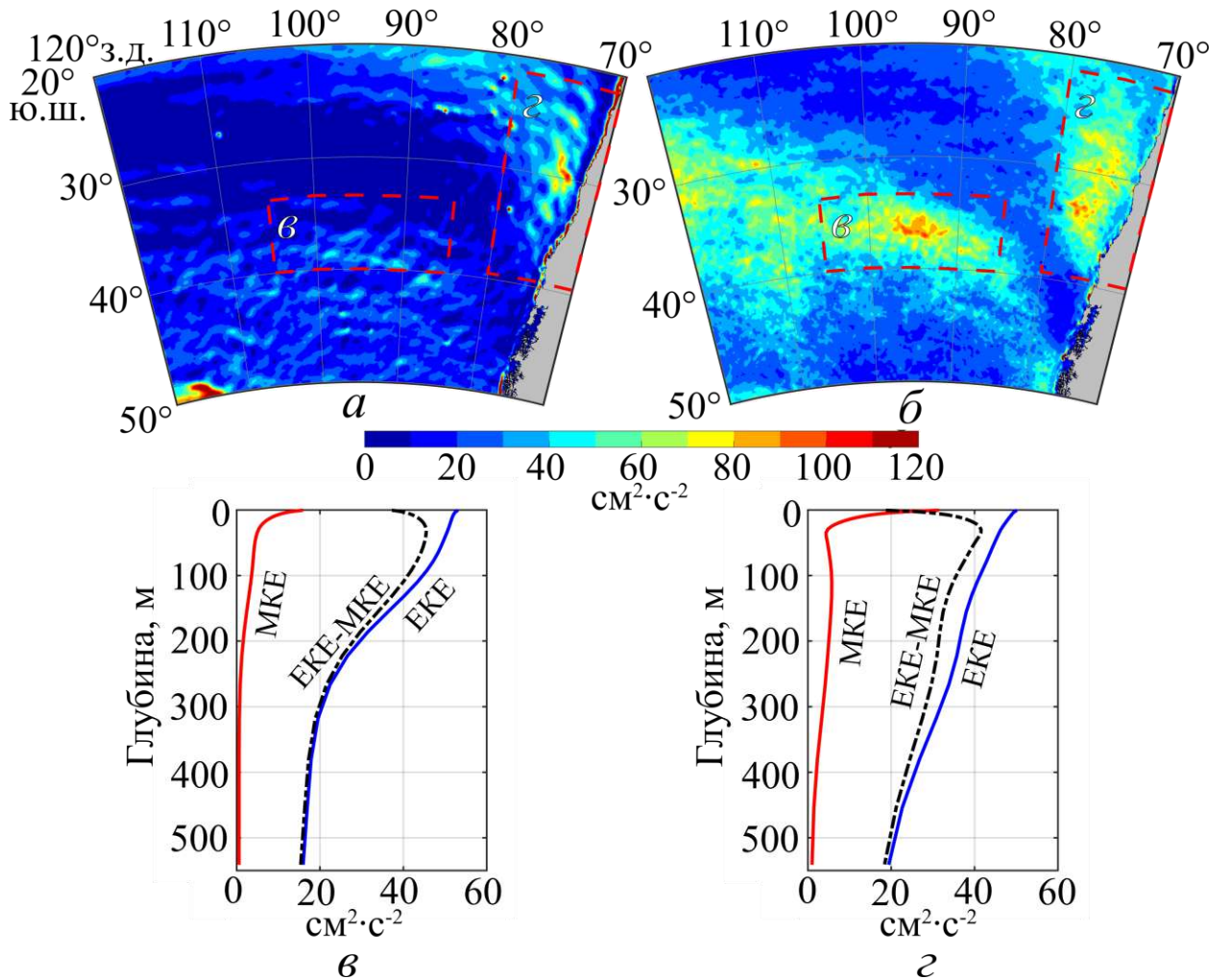


Figure 2.10. Average values of average kinetic energy (MKE) (a) and vortex kinetic energy (EKE) (b) on the surface for 2010-2020; Vertical profiles MKE, EKE and EKE-MKE (c and d) averaged over selected areas (red dotted line) according to GLORYS12V1 ($\text{cm}^2 \cdot \text{s}^{-2}$).

In Fig. 2.9 and Fig. 2.10, it can be seen that the distribution of the mapped parameters differs significantly from the zonal one, so that the areas of increased values are elongated towards the equator. Moreover, this trend is more pronounced for anticyclones. Obviously, this fact is closely related to the meridional displacement of eddies. Such a displacement of mesoscale eddies is noted in many works, both theoretical and in works whose results are based on the use of satellite data. At the same time, it was found that the trajectories of cyclones tend to shift towards the pole, and anticyclones – towards the equator. Despite the fact that the possible physical mechanisms of such a meridional displacement are given in the

publications of other authors, a single mechanism has not yet been discovered. A detailed review of research on this topic is provided in (Gnevyshev et al., 2021a), where the authors consider possible mechanisms using the example of mesoscale eddies in the South Atlantic and propose a version that is consistent with the narrow-angle angular emission of long Rossby waves by non-zonal currents.

According to the data in Table 2.3, it can be found that the number of cyclones with a life span of 10-90 days is much higher than the number of anticyclones of similar duration, while among eddies with a life span of more than 180 days the situation is the opposite. The maximum amplitude, orbital velocity, and radius are typical for mesoscale eddies with a lifetime of more than 180 days. Such vortices travel significant distances, passing on average over 400 km in their lifetime.

Table 2.3. Average estimates of anticyclone (AC) and cyclone (C) parameters in the Southeastern Pacific.

Parameters	AC			C		
	[10-90)	[90-180)	180+	[10-90)	[90-180)	180+
Amount	28779	4176	2172	33828	4246	1665
Amplitude, cm	1,63±1,01	3,09±1,56	4,27±1,72	1,63±0,90	2,81±1,24	3,67±1,44
Orbital velocity, cm/s	7,58±2,66	9,83±2,95	11,28±2,82	7,55±2,70	9,37±2,88	10,75±3,21
Radius, km	47,61±13,77	65,43±16,38	73,68±15,53	46,98±12,66	64,47±15,45	74,65±16,77
Movement, km	60,32±52,42	200,24±126,41	442,07±324,85	58,46±50,23	201,65±130,35	490,99±354,52
Movement, km/day	4,96±2,19	4,91±1,83	4,38±1,45	4,97±2,11	5,12±1,62	5,03±1,34

Figure 2.11 shows diagrams of the distribution of the recurrence of the main parameters of cyclones and anticyclones. It is noticeable that most eddies have a radius of 25-75 km, an amplitude of less than 5 cm, an orbital velocity of 5-15 cm/s, and a lifetime of no more than 50 days. The average monthly number of cyclones and anticyclones, their radius, amplitude and orbital velocity demonstrate the presence of pronounced seasonal variability (Fig. 2.12). Thus, the maximum number of eddies was recorded in the period July-November, while the minimum number was detected in February-March. From February to July, there is a decrease in the average radius and amplitude of anticyclones, and from January to July, cyclones. The highest values of the orbital velocity are observed from October to December (Fig. 2.12).

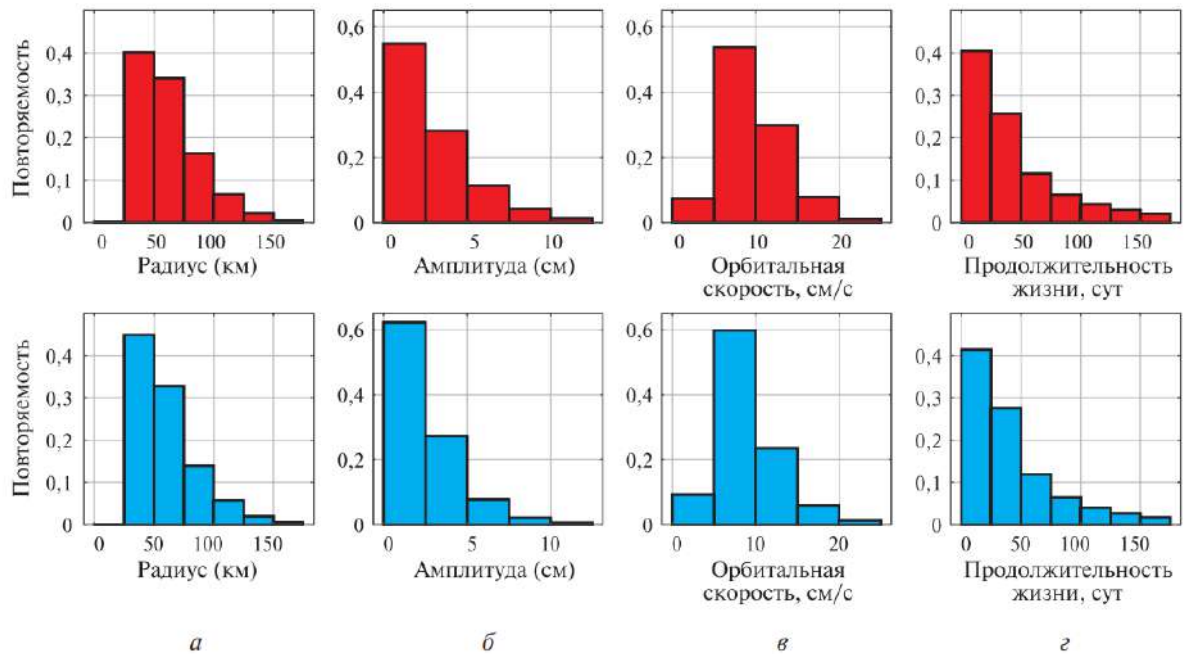


Figure 2.11. Probability of radius (a), amplitude (b), orbital velocity (c), lifetime (d) of anticyclones (above) and cyclones (below) for 1993-2020 according to META3.2 DT data.

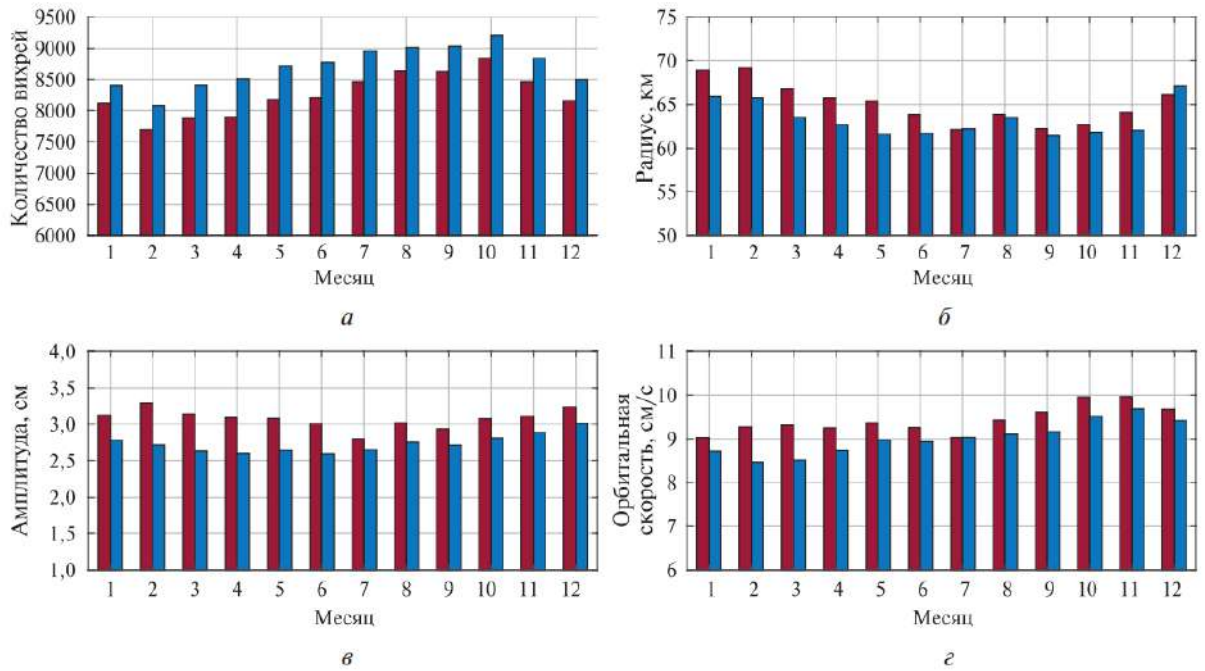


Figure 2.12. Average monthly characteristics of mesoscale eddies for 1993-2020 according to META 3.2 DT data: number of eddies per month (a), radius (b), amplitude (c), orbital velocity (d) for anticyclones (red) and cyclones (blue).

Among the many eddies, we are most interested in long-lived eddies. Figure 2.13 shows the trajectories and parameters of cyclones and anticyclones with a lifespan of more than 180 and 550 days. It can be noted that the vast majority of both anticyclones and cyclones are moving in a westerly and northwesterly direction, while only a few eddies are moving in the opposite direction. It can also be noted that the number of the longest-lived anticyclones exceeds the same value for cyclones. This difference is due to the fact that anticyclones are more stable formations. This fact is considered in more detail in the work of M.V. Nezlin (1986) in terms of cyclone-anticyclone asymmetry. Thus, the observed cyclone-anticyclone asymmetry is a direct consequence of scalar nonlinearity and a very fundamental dispersion-nonlinear property of Rossby eddies. The longest life expectancy among anticyclones is 1696 days, and 749 days among cyclones. During this time period, the anticyclone overcame 4555 km, while the cyclone covered 4163 km, while the movement of the eddies amounted to 1439 and 1366 km, respectively.

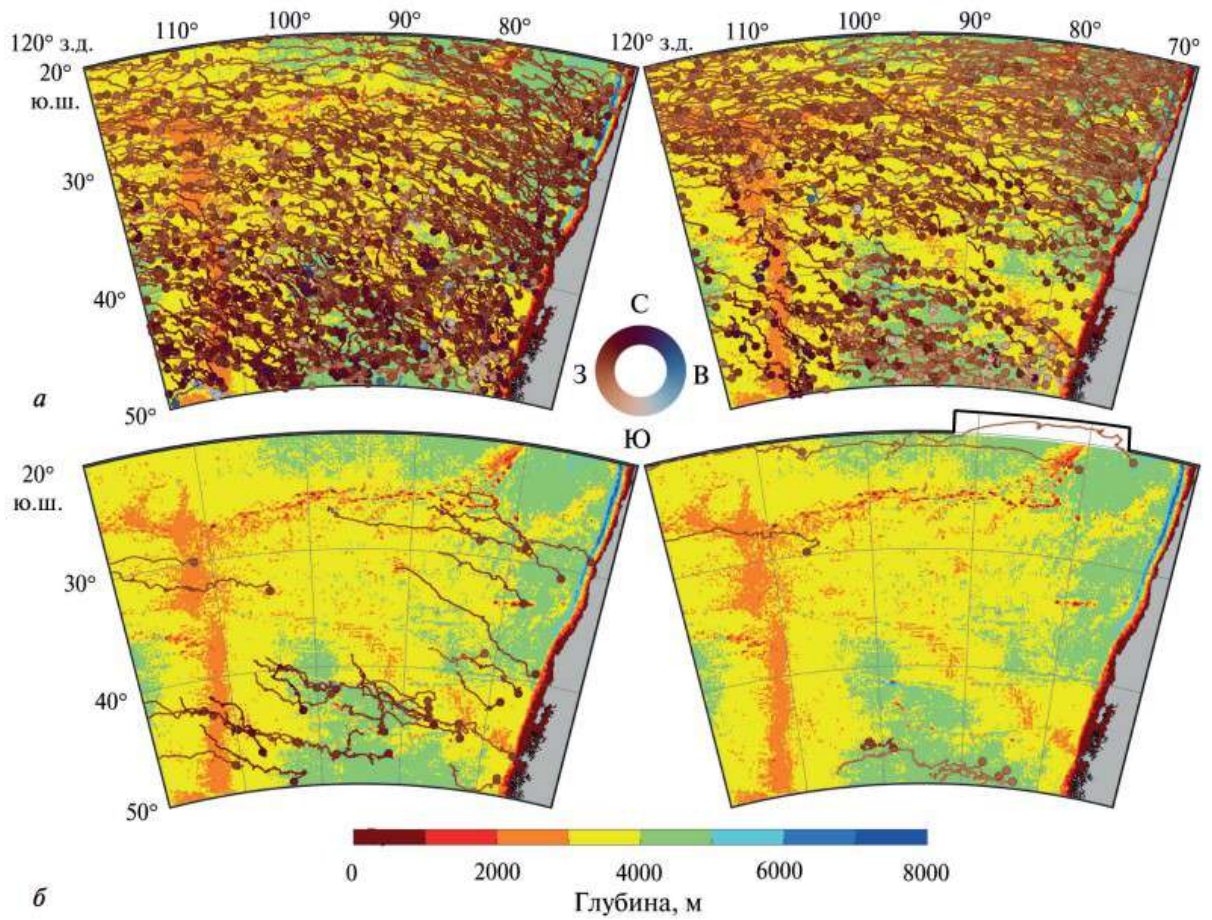


Figure 2.13. Trajectories of anticyclones (left) and cyclones (right) with a lifespan of more than 180 days (a) and 550 days (b) for 2010-2020 according to META3.2 DT.

Comparison of the parameters of long-lived mesoscale eddies of the South Pacific with the characteristics of mesoscale eddies of the South Atlantic

In the work (Gnevyshev et al., 2021b), the authors considered the trajectories of long-lived eddies of Agulhas (South Atlantic) with a lifespan of more than two years. In turn, in our work we analyze the tracks of long-lived eddies. In both cases, data from the META, created on the basis of altimetric information, is used. A comparison of the characteristics of mesoscale cyclones and anticyclones demonstrates the following results. It has been established that only anticyclones are long-lived among the eddies of Agulhas. They move in an almost straight line to the northwest, traveling thousands of kilometers and crossing the South Atlantic

(Gnevyshev et al., 2021b, table 1). In turn, this is characterized by the presence of long-lived cyclones, although their total number is significantly less than the number of long-lived anticyclones. It can be noted that in most of the parameters under consideration, such as lifetime, amplitude, radius, orbital velocity and displacement, long-lived eddies are much inferior to those of the South Atlantic. This difference is due to differences in the mechanisms of generating these eddies. The fact is that long-lived Agulhas eddies are formed due to the destruction of the Agulhas rings, which contributes to the formation of powerful and stable anticyclones moving in a westerly direction and capable of crossing the Atlantic Ocean. There is no similar mechanism in this region, since mesoscale eddies are formed mainly due to barotropic and baroclinic instability of currents. The movement of eddies occurs mainly under the influence of currents, topography, and the beta effect. A comparative analysis of these factors is given in the works (Gnevyshev et al., 2019, 2021; Gnevyshev et al., 2022). In the South Atlantic, the eddies move almost in a straight line. Under the influence of topography, in particular, at the intersection of the Whale and South Atlantic ridges, the trajectories change direction of movement, after which they spread out in a straight line again. Eddies do not change the azimuth of propagation when crossing the East Pacific Uplift. It is worth noting that in the 40-50° S, some anticyclone trajectories move along the isobaths (Fig. 2.13).

Discussion and main conclusions

It has been found that the largest number of mesoscale eddies in the South Pacific is formed in the coastal shelf area, as well as on the slopes of the Peruvian and Chilean trenches. The number of anticyclones per cell is maximum (more than 120 units) in the coastal region in the band 38-48° S, whereas for cyclones similar values are typical along the entire coastal region. In the central part of the study area (20-30° S), the number of anticyclones and cyclones can exceed 80 or more vortices per cell. In the 30-40° S the number of eddies is significantly reduced: on the order of 30-40 per cell, the eddy kinetic energy in this region is maximum and reaches 120 cm²/s⁻². This is due to the fact that the eddies here have a maximum amplitude,

radius, and orbital velocity. On the other hand, the MKE is low, since in the time scale range under consideration, the eddy component makes the greatest contribution to variability. The maximum values of MKE and EKE are fixed in the surface layer, decreasing with depth. In the 40-50° S, the number of eddies (especially cyclones) increases dramatically due to the influence of the ACC. Areas with increased values of eddy parameters (amplitude, radius, and orbital velocity) are elongated towards the equator, and this is most pronounced for anticyclones.

Diagrams of the average values of anticyclone and cyclone parameters show that most eddies have a radius of 25-75 km, an amplitude of more than 5 cm, an orbital velocity of 5-15 cm/s, and a lifetime of no more than 50 days. The maximum number of eddies was recorded from July to November, the lowest in February and March. From October to December, the highest values of the orbital velocity of the eddies are observed. For mesoscale eddies moving westward, the presence of a meridional displacement is noted. Thus, the trajectories of cyclones shift to the pole, and anticyclones to the equator. Among the long-lived cyclones and anticyclones, an anticyclone with a lifespan of more than 1600 days and a distance traveled of more than 4500 km stands out. The amplitude of this eddy reached 14 cm, and the radius exceeded 130 km. A comparison of the main parameters of the mesoscale eddies of the South Atlantic and the South Pacific indicates that the eddies of the South Pacific are inferior to the eddies of the South Atlantic in most characteristics, with the exception of one: long-lived cyclones have been recorded in the South Pacific, while no such eddies have been detected in the South Atlantic. The practical significance of the results obtained lies in the fact that the developed original methods and approaches for studying mesoscale eddy dynamics in the South Pacific can be applied to other areas of the Global Ocean, including for solving fishing problems.

CHAPTER 3. BALTIC SEA

3.1. Data

The work uses data from 1993 to 2020 from the reanalysis of the hydrophysical fields of the Baltic Sea BALTICSEA_REANALYSIS_PHY_003_011, available on the Copernicus Marine Service portal (https://data.marine.copernicus.eu/product/BALTICSEA_REANALYSIS_PHY_003_011/). The NEMO-Nordic model, based on the NEMO-3.6 model. The reanalysis uses the WAM wave model (version 4.6.2), adapted to the conditions of the Baltic Sea. Atmospheric forcing from 1993 to 2011 was determined using Euro4M atmospheric reanalysis (spatial resolution – 22 km), and from 2012 to 2018 using UERRA reanalysis (spatial resolution – 11 km). The density calculation in the initial model was carried out using the thermodynamic equation of seawater TEOS-10. Some of the parameters (sea surface height, concentration, and thickness of sea ice) are available with hourly time resolution, while salinity, temperature, horizontal components of currents, and MLD are available with daily and monthly averages. The spatial resolution in latitude and longitude is 2' and 3'20" (0.03333° and 0.05556°, respectively). Vertically, the massif contains 57 horizons from the surface to a depth of 711 m (in the Skagerrak Strait). The distance between horizons varies from 1 m (on the surface) to 25 m for the last horizons. In the Baltic Sea, the last horizon according to the reanalysis data is the 361 m horizon in the Landsort depression.

3.2. Methods

To automatically identify mesoscale cyclones and anticyclones in the Baltic Sea, we used the method of automatic eddy identification described in detail in (Faghmous et al., 2015) and available at (<https://github.com/jfaghm/OceanEddies>). In our dissertation research, this algorithm has already been described in detail (see section 1.2). To detect mesoscale eddies, we use daily data on the SSH from

reanalysis of the hydrophysical fields of the Baltic Sea. Closed areas with positive (negative) sea surface height anomalies are defined as anticyclones (cyclones). The amplitude of each eddy structure is considered to be the difference between the magnitude of the extremum in the level field and the value of the level at the eddy boundary (Faghmous et al., 2015).

3.3. Seasonal and interannual variability of mesoscale eddies of the Baltic Sea

The purpose of this part of the dissertation research is to study the main characteristics (amplitude, radius, life span, and amount), as well as the spatial and temporal variability of mesoscale eddies of the Baltic Sea in 1993-2020. To achieve this goal, data from the reanalysis of the hydrophysical fields of the Baltic Sea, as well as the method of automatic identification of eddy structures, are used. Using the eddy identification algorithm in the Baltic Sea for 1993-2020, 119840 vortices were detected, of which 54246 (45.3% of the total) are anticyclones and 65594 (54.7% of the total) are cyclones, respectively. The number of long-lived (life span ≥ 7 days) anticyclones and cyclones is 1728 and 1940 vortices (1.4% and 1.6% of the total number of eddies, respectively). Such estimates indicate that the number of cyclones in the Baltic exceeds by 12% the number of anticyclones for long-lived eddies and by 21% for all types of eddies. Figure 3.1 shows the probability of the amplitude, radius, and lifetime of cyclones and anticyclones. It can be noted that the greatest probability of amplitude varies in the range 0.05-0.20 m (46% of anticyclones and 41% of cyclones, respectively) and further the recurrence gradually decreases. There is also a slight asymmetry – anticyclones with an amplitude of less than 0.20 m are smaller than cyclones, while the difference can reach 2.5%. A radius of less than 10 km has 59% of anticyclones and 64% of cyclones, 29% of anticyclones and 27% of cyclones have a radius of 10-15 km, and 9% of anticyclones and 7% of cyclones have radii of 15-20 km (Figure 3.1). Thus, the most frequent mesoscale eddies in the Baltic Sea are eddies with a radius of 5-10 km, with the number of cyclones prevailing over the number of anticyclones. Eddies with a radius of more than 20 km account for only 3% and 2% of the total number of anticyclones

and cyclones, respectively. It has been established that some eddies may have a radius of more than 30 km, however, their number is small. Analyzing the life span of eddies, it can be seen that the majority (about 60%) of both cyclones and anticyclones exist for 2-3 days, and 21% for 3-4 days. Thus, only 1/5 of the total number of eddies has a lifespan of more than 4 days, while a certain number of eddies can exist for more than 10 days.

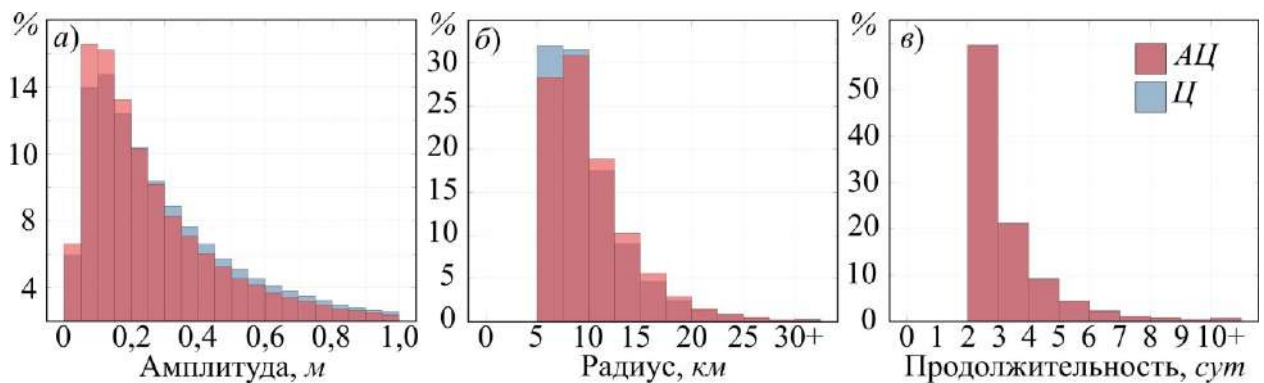


Figure 3.1. Probability (%) of amplitude (m), radius (km), and lifetime (day) for anticyclones (AC, red) and cyclones (C, blue).

According to Table 3.1, it can be established that the average amplitude of cyclonic eddies is 12% higher than the same characteristic for anticyclones. On the other hand, the area of anticyclones exceeds the area of cyclones by 6%, and is also characterized by greater variability. It is noticeable that cyclones are characterized by high movement speeds and their variability, compared with anticyclones. On average, cyclones and anticyclones travel 3.7-4.0 km per day, which corresponds to speeds of about 4.4-4.6 cm/s. A certain number of eddies are capable of traveling 10-24 km per day, which corresponds to speeds of 11.6-27.8 cm/s. Anticyclones are characterized by a slightly longer life span than cyclonic structures (Table 3.1). In the work (Vortmeyer-Kley et al., 2019), the authors indicate that the eddies forming in the deep-water parts of the Baltic Sea have the greatest displacement. This feature may be associated with a decrease in bottom friction and weak interaction with the underlying boundary layer.

Table 3.1. Main characteristics of mesoscale eddies.

	AC	C	AC and C
Amount	54246	65594	119840
Amplitude (m)	0.25±0.07	0.28±0.07	0.27±0.07
Area (km ²)	380±98	356±91	368±94
Radius (km)	11.00±5.59	10.65±5.38	10.82±5.47
Geostrophic velocity (cm/s)	6.7±2.1	6.4±2.0	6.5±2.0
Movement per day (km)	3.79±0.84	4.01±0.94	3.91±0.90
Movement speed (cm/s)	4.39±0.98	4.64±1.08	4.52±1.04
Life span (days)	2.83±1.49	2.82±1.44	2.83±1.47

Figures 3.2a and 3.2b show the total number of eddies in the Baltic Sea per cell of the reanalysis grid for 1993-2020. It is noticeable that the zones with more than 50 eddies per grid cell are: Kattegat Strait, Kiel and Mecklenburg Bays, as well as the southern tip of Bornholm Island. A significant number of anticyclones were detected near the northeastern tip of the Gotland, as well as in the Gdansk and Riga Bays. Also, a significant number of anticyclones can be traced in the Gulf of Finland and the Gulf of Bothnia. Cyclones tend to be concentrated in the Kattegat Strait, at the northern extremities of Bornholm and Gotland, as well as in the Gulf of Riga. A significant number of cyclones were recorded in the Gulf of Finland and the Gulf of Bothnia and near the Aland Islands.

The average direction of motion of mesoscale cyclones and anticyclones is shown in Figures 3.2 and 3.2. It is noticeable that in the southern part of the Baltic, eddies of both types have a northeasterly direction of motion, while in the Gdansk and Curonian Lagoons eddies are characterized by an easterly direction of motion. East of Gotland most of the cyclones are moving in a southerly direction, changing the direction of their movement to the west at the southern tip. In the Gulf of Riga, anticyclones and cyclones form closed circulations with the appropriate direction. In the Gulf of Finland, anticyclones are moving in a northerly direction, cyclones in a

northeasterly direction. The eddies flow from the central part of the Baltic Sea into the Gulf of Bothnia, and further move in a northerly direction.

Figures 3.2d and 3.2e show the trajectories of long-lived anticyclones and cyclones. In the southern and central parts of the Baltic Sea, chains of eddies structures are noticeable, and the trajectories and direction of long-lived vortices practically coincide with the general circulation of the Baltic Sea. In the southern part of the Baltic Sea, as well as north of the Gotland most long-lived anticyclones and cyclones have an easterly direction. On the other hand, a significant number of westward-moving anticyclones have been recorded in the Gulf of Finland and the Gulf of Gdansk. Such results indicate significant zonal and meridional transfer of heat and salt by long-lived cyclones and anticyclones, which helps to reduce the contrast of thermohaline characteristics between the salty North Sea waters entering the Baltic and the fresh waters of the river runoff. It is worth noting that in the southern part of the Baltic Sea, eddies of both types follow an easterly direction through an underwater trench, further dividing into two branches – one branch follows the isobath to the northeast, while the other branch moves towards the Gulf of Gdansk.

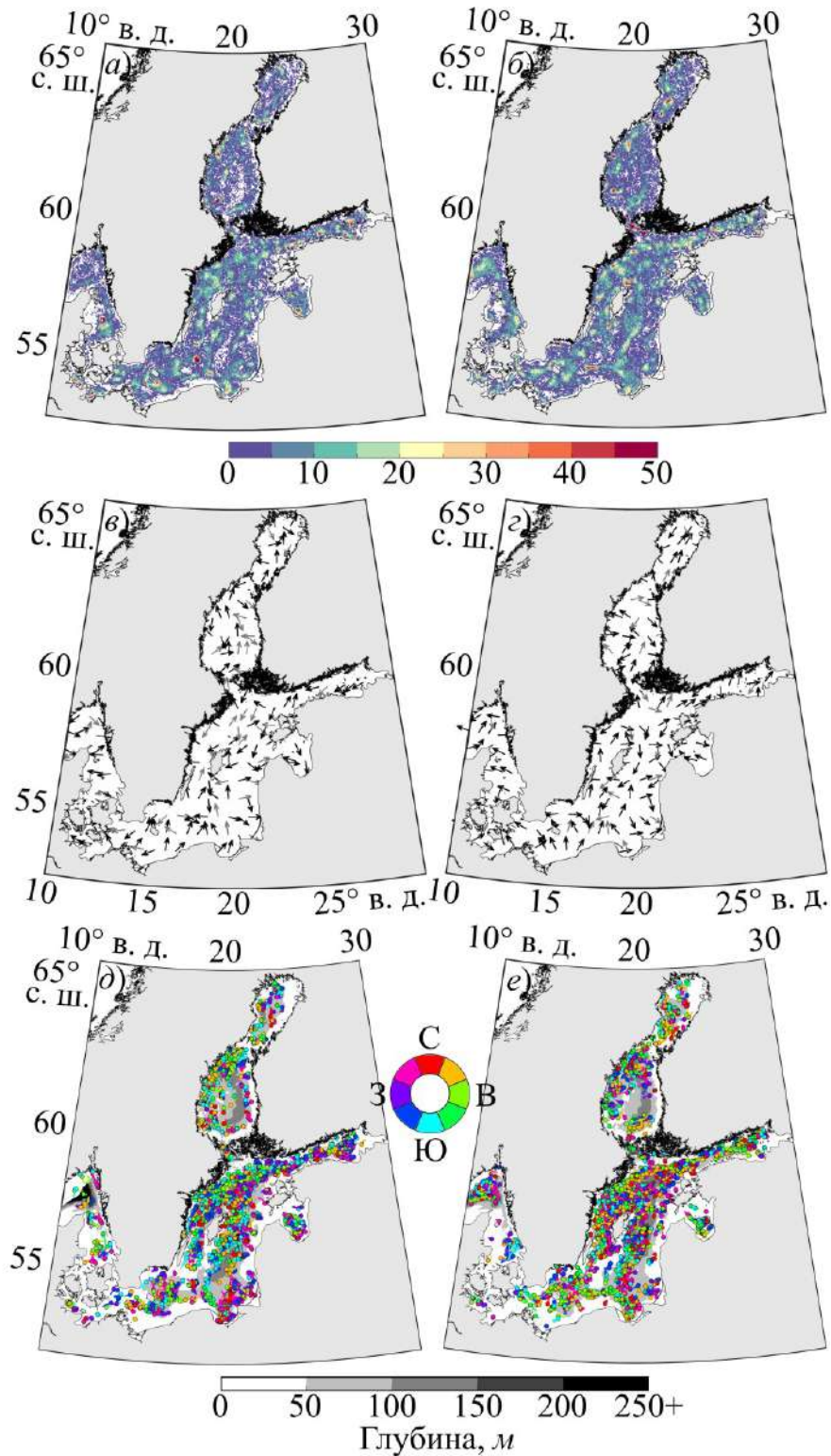


Figure 3.2. Total number of mesoscale anticyclones (a) and cyclones (b) per reanalysis grid cell for 1993-2020; general circulation of mesoscale anticyclones (c) and cyclones (d) for 1993-2020, the most intense eddy velocities are shown in black; trajectories of long-lived (>7 days) mesoscale anticyclones (e) and cyclones (e), the color shows the bathymetry (m).

According to Figure 3.3, it can be seen that the ratio of the major and minor semimajor axes of the Baltic Sea eddies is close to 1.58. This value indicates that most of the eddies in the Baltic are ellipsoidal, and the shape, size, and direction of motion of anticyclones and cyclones are quite close. The distribution of the magnitudes of the large and small semi-axes of the eddies is shown in Figures 3.3a and 3.3b. For small sizes, the ratio of axes for anticyclones and cyclones is also close to 1.58. With an increase in the length of the greater semi-axis to 30 km, cyclones noticeably shift the ratio of the axes to one, which is most clearly seen at a length of about 40 km. Such estimates demonstrate that the shape of most cyclones with a radius of more than 30 km is close to a circle, while for anticyclones of similar size it remains ellipsoidal. It is known that highly elongated mesoscale eddies are extremely unstable (Zhmur, 2010). The ratio of the semi-axes of the Baltic eddies obtained by us (~ 1.58) indicates a significant influence of background currents on the mesoscale eddy dynamics, as a result of which the vortices tend to elongate. At the same time, this result is much lower than the critical value for ellipsoidal eddies (the ratio of semi-axes is 3:1), which indicates a fairly high stability of the Baltic eddies.

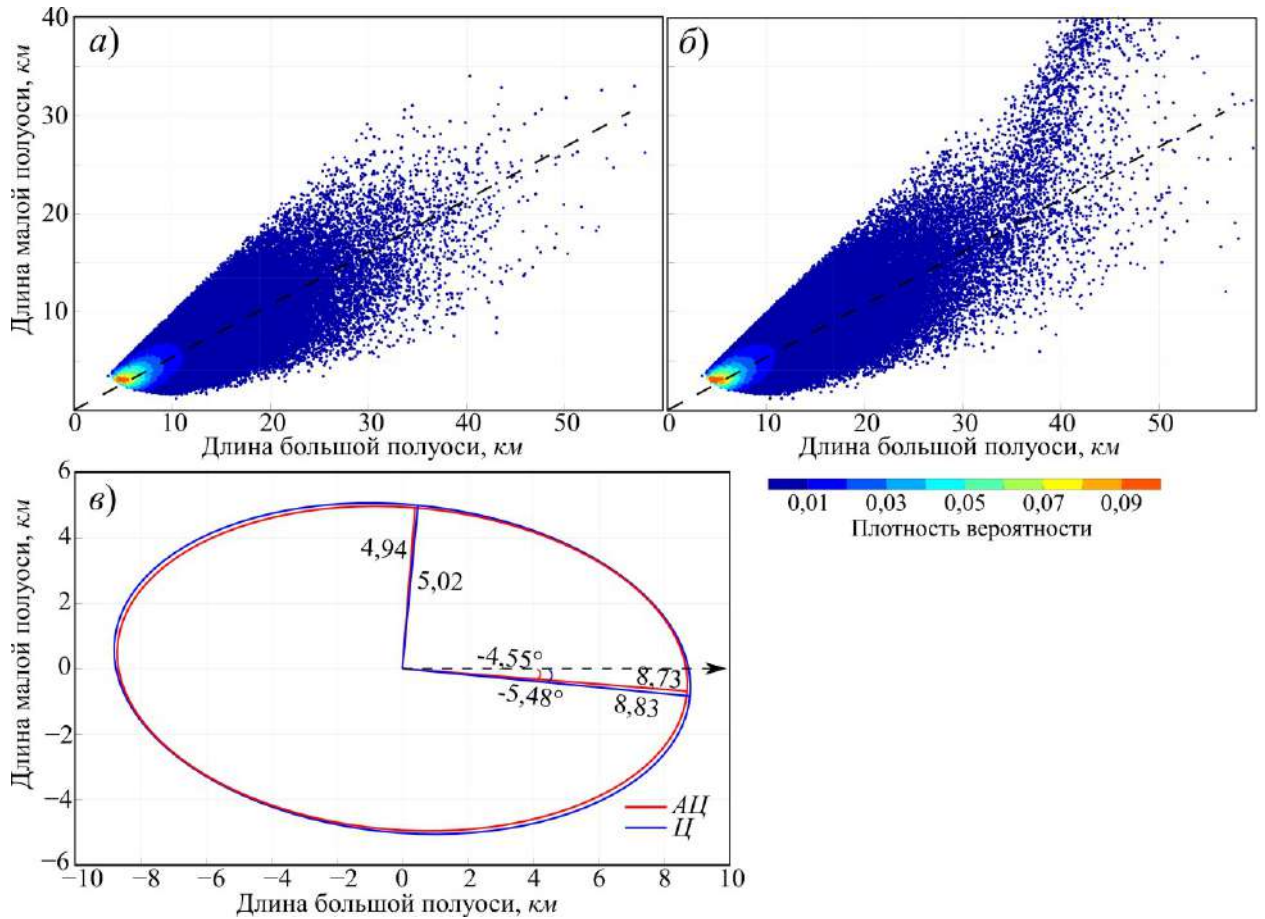


Figure 3.3. Distribution and probability density of the lengths of the major and minor semi-axes (km): a – anticyclones, b – cyclones. The black line shows the average ratio of the semi-axes; c is the average length and slope of the major and minor semi-axes: cyclones (C, blue) and anticyclones (AC, red).

The mesoscale eddies of the Baltic Sea are characterized by positive values of significant linear trends in the amplitude and number of cyclones and anticyclones (Figs. 3.4a and 3.4b). So, for anticyclones and cyclones, the corresponding amplitude trends are 0.6 cm/10 years and 0.5 cm/10 years. At the same time, the number of anticyclones and cyclones is growing by 16.4 and 16.0 eddies per year. The range of the average annual amplitude values of anticyclones and cyclones exceeds 3.5 and 3.0 cm, respectively. The range of the number of anticyclones and cyclones is 524 and 680 eddies, respectively. It can be noted that the amplitude and number of cyclones in all years exceed the similar parameters of anticyclones. The interannual variability of the amplitudes and the number of eddies can be clearly

traced between neighboring years. Thus, the average annual amplitude values can vary by 2 cm between two adjacent years (0.24 m and 0.26 m for anticyclones in 2009 and 2010, respectively). The average number of cyclones and anticyclones for neighboring years can vary by more than 200-300 eddies (for example, 2159 cyclones in 2011 and 2493 cyclones in 2012, respectively), with variability increasing significantly in recent years.

The average monthly values of cyclone and anticyclone amplitudes are characterized by a sharp increase in the autumn-winter period, while the lowest values are observed from late spring to mid-summer (Fig. 3.4c). In the period from July to December, a significant increase in the amplitudes of both types of vortices was recorded – from 0.24 to 0.27 m for anticyclones and from 0.25 to 0.31 m for cyclones. In the future, from January to May, the average amplitudes of cyclones and anticyclones decrease. It is worth noting that the amplitudes of cyclones throughout the year exceed similar values for anticyclones.

In contrast to the amplitude, the minimum number of eddies was recorded in the autumn-winter period – less than 3.5 and 4.5 thousand anticyclones and cyclones in February (Fig. 3.4d). In the future, until May-August, the number of vortices of both types is growing, the number of cyclones is maximum in May (6.5 thousand), anticyclones in August (more than 5 thousand). Starting in September, the average monthly number of eddies of both types begins to decrease linearly. In all months, the number of cyclones exceeds the number of anticyclones.

The average annual radii of cyclones and anticyclones are characterized by pronounced variability, as well as small significant negative trends (Fig. 3.4e). The angular coefficient of the linear trend in cyclones has large values in modulus, compared with the same parameter for anticyclones. Only in 2011, the average size of cyclones significantly exceeded the size of anticyclones. Figure 3.4e shows the average area simultaneously occupied by cyclones and anticyclones in the Baltic Sea. Despite the fact that anticyclones are larger in size than cyclones, due to their significant number, the latter occupy a larger area than anticyclones. Eddies of both types are characterized by pronounced interannual variability, so the area occupied

by eddies can vary from year to year by 25-33%. In general, there is a significant positive linear trend for the area of cyclones and anticyclones, while the angular trend coefficient of anticyclones is higher than that of cyclones.

The radii and areas of cyclones and anticyclones are characterized by significant seasonal variability (Figures 3.4g and 3.4h). So, from January to July, there is a sharp increase in the values of eddy radii from 10 to 11.5-11.8 km. Starting in August, the radius of the eddies decreases linearly to a minimum in December. The area of cyclones and anticyclones is changing in a similar way. Thus, the minimum values were recorded in December, and then, until August, the area grows, with anticyclones beginning to occupy the same part of the Baltic Sea area as cyclones (Fig. 3.4h). In summer, cyclones and anticyclones occupy more than 8000 km² at a time, compared to 4000 km² in December. Thus, in winter, mesoscale eddies simultaneously occupy ~ 2% of the Baltic Sea area, while in summer this indicator increases to 4%.

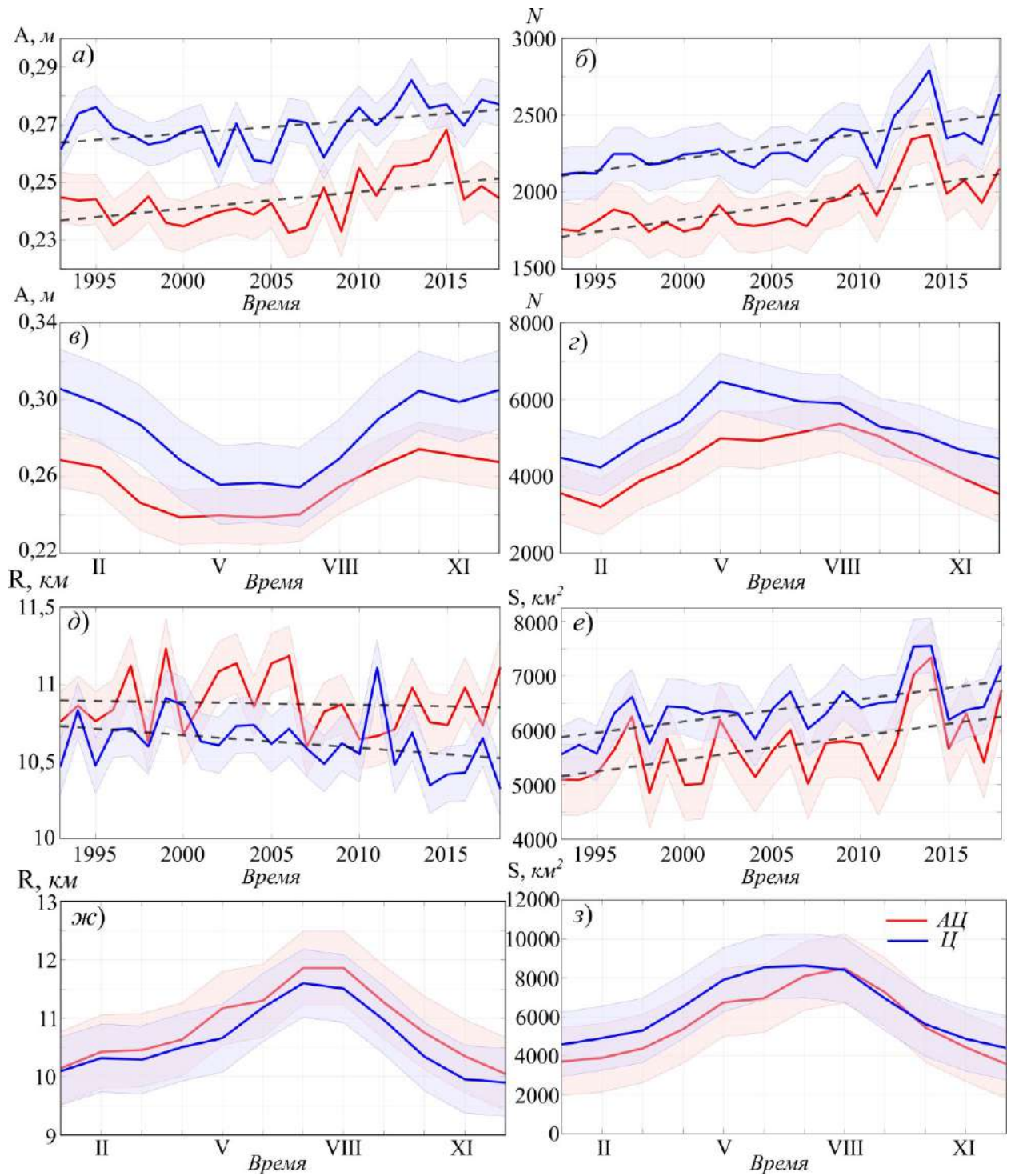


Figure 3.4. Average annual values for 1993-2018: amplitudes (a), numbers (b), radii (e), and areas (e) of cyclones (blue) and anticyclones (red); monthly averages for 1993-2018: amplitudes (c), numbers (d), radii (w) and the area (s) of cyclones (blue) and anticyclones (red).

Main conclusions

Using the method of automatic identification of eddies in the Baltic Sea in 1993-2020, 119840 mesoscale eddies were detected, 54.7% of which are cyclones and 45.3% anticyclones. A similar difference in the number of cyclones and anticyclones is found in other areas of the Global Ocean (Dong et al., 2012). Most of the eddies have an amplitude of 0.05-0.25 m, a radius of 5-10 km, and a lifetime of about 2-3 days. Our results are close to the values given in the paper (Vortmeyer-Kley et al., 2019). Thus, the authors note that most eddies have a radius of less than 9 km and a lifespan of just under 2 days. On average, most of the vortices from work (Vortmeyer-Kley et al., 2019) moved 10 km during their existence, which is quite close to our estimates (11 km). It has been established that a small number of eddies have a radius of more than 30 km and a lifetime of more than 10 days. Some of the eddies can travel 10-24 km per day, which corresponds to speeds of 11.6-27.8 cm/s.

The areas with the largest number of eddies per unit area are the Kattegat Strait, the Gulf of Riga and the Gulf of Gdansk, as well as parts of the Gulf of Finland and the Gulf of Bothnia. A significant number of eddies were detected over some banks and near the bays, near the Aland Islands and the islands of Gotland and Bornholm. In some regions, the number of cyclones may be several times higher than the number of mesoscale anticyclones. A similar feature is mentioned in (Vortmeyer-Kley et al., 2019), and may be related to the interaction of the general circulation and bathymetry, contributing to the generation of cyclones.

In the southern part of the Baltic Sea, the eddies have a predominantly northeasterly direction, in the Gulf of Gdansk, the eddies move from the coast in a northeasterly direction, in the Curonian Lagoon – in an easterly direction, towards the coast. To the south and east of Gotland, the eddies have a southerly direction. This type of eddy circulation is close to the results obtained for the sea surface using the three-dimensional hydrodynamic model M3D (Jedrasik and Kowalewski, 2018). In the future, the vortices move in a northeasterly direction towards the Gulf of Finland and the Gulf of Riga, forming a closed circulation in the latter. In the Gulf of Finland, cyclones tend to have a northeasterly direction, while anticyclones tend

to have a westerly direction. Cyclones and anticyclones penetrate into the Gulf of Bothnia and then move in a northerly direction. It was found that eddies form a cyclonic circulation in the northern part of the Gulf of Bothnia.

Most long-lived eddies move in an easterly direction. At the same time, long-lived cyclones circle Bornholm Island from the north, while anticyclones from the south. This feature is explained in the monograph (Zyryanov, 1995) by the nature of the current and bottom topography, as well as the influence of wind action. According to Figure 3.3, it can be seen that long-lived eddies are mainly confined to areas of topographic irregularities, for example, eddies follow isobaths, and a significant part of them are recorded in the deep-water parts of the Gulf of Bothnia, as well as over depressions. A similar pattern of eddy movement in the Baltic Sea is described in (Vortmeyer-Kley et al., 2019), where it is emphasized that eddies follow along f/H isolines. In the Gulf of Finland, most long-lived anticyclones are spreading westward.

On average, the ratio of the major and minor semimajor axes is 1.58 for the Baltic eddies (Fig. 3.3). This means that most of the Baltic eddies have an ellipsoid shape and can be described by the theory of ellipsoidal eddies (Zhmur, 2010). This value indicates a strong influence of background currents on eddy dynamics, while it is much less than the critical ratio (3:1), which indicates the stability of the Baltic eddies. It was found that for cyclones with a radius of more than 30 km, the ratio of the semi-axes is close to 1, which indicates their shape is close to a circle and the background current has little effect on them (Fig. 3.3).

The amplitude and number of eddies vary significantly both by year and by season. Significant positive linear trends were found for these parameters (Figures 3.4a and 3.4b). The maximum values of the amplitudes were recorded in the autumn-winter period, while the lowest values were recorded from late spring to midsummer (Fig. 3.4c). The number of eddies is maximum in spring and summer and minimum in February (Fig. 3.4d). A similar trend is noted in the work (Vortmeyer-Kley et al., 2019), where the authors indicate that the number of eddies has a significant seasonal course with a maximum in July and a minimum in December-January. The minimum

in winter may be associated with increased wind speed, which destroys long-lived eddies (Vortmeyer-Kley et al., 2019).

For the spatial scales of cyclones, there is a small significant interannual negative trend, which is also weakly expressed in anticyclones (Fig. 3.4e). In summer, the sizes of both types of eddies are maximum, while the lowest values are recorded in January. On average, the area occupied by eddies in the Baltic Sea increases significantly. The area also varies significantly by season, so vortices occupy 2% of the Baltic Sea area in winter and 4% of the area in summer.

The results obtained demonstrate the significant influence of mesoscale eddies on the dynamics of the Baltic Sea waters, and also describe in detail the main characteristics of mesoscale eddies, their seasonal and interannual variability.

CONCLUSION

In this dissertation research, a comprehensive analysis of the eddy mesoscale dynamics of the Norwegian and Baltic Seas, as well as the northwestern and southern parts of the Pacific, was carried out. The paper provides estimates of the main characteristics, as well as statistical analysis of mesoscale eddies of the Norwegian and Baltic Seas, as well as the northwestern and southern parts of the Pacific, and a Lagrangian analysis of the dipole structures of the Lofoten Basin. Estimates of the available potential and kinetic energy of the Lofoten Vortex are given, and the rate of barotropic and baroclinic energy conversion is calculated for the Lofoten Basin. The influence of the seabed topography on the propagation of mesoscale eddy structures, as well as on the intensity of convection, has been studied. Let's move on to the main results:

1. Based on the results of numerical experiments, it has been established that the presence of a flat abyssal plain with a topographic depression in the center is a necessary condition for the formation of a quasi-permanent Lofoten Vortex. The presence of the border between the Norwegian and Lofoten Basins contributes to the permanent presence of land within the Lofoten Basin. The absence of a boundary leads to the formation of a quasi-permanent anticyclone in the Norwegian Basin. The presence of seamounts and ridges negatively affects the development of convection in the winter-spring period in the Norwegian Basin, while the smooth relief of the Lofoten Basin contributes to an increase in the MLD during the convection process. It has been established that the MLD in the Norwegian Sea is significantly lower, compared with similar values for the Lofoten Basin. In the Norwegian Sea, convection reaches its maximum development in February and then weakens slightly in March. The greatest MLD was recorded in the area of the Lofoten Vortex. A change in topography leads to a displacement of areas with an increased thickness of the MLD. The topographic isolation of the Lofoten Basin, as well as the nature of the seabed, lead to the formation of an area with increased

vortex activity in the center of the basin. At the same time, eddy mesoscale dynamics is practically absent in the Norwegian Basin.

2. In the region of the core of the Lofoten Vortex, the highest values of eddy kinetic energy are observed, whereas for the mean kinetic energy, the maximum values are characteristic of the periphery of the eddy. In winter, an increase in both eddy and mean kinetic energy was recorded, with the eddy kinetic energy exceeding the average throughout the entire layer from 0 to 1000 m. The available potential energy of the Lofoten Vortex is an order of magnitude higher than the kinetic energy, and for the first one, there is a significant linear positive trend with a coefficient of $0.23 \cdot 10^{15}$ J/year. The maximum values of available potential energy are observed at the horizon of 700 m, while the greatest contribution to the potential energy of the eddy is made by the layer of 600-900 m. The highest values of the kinetic energy of the Lofoten Vortex are recorded in the layer from 0 to 400 m. Multidirectional flows of barotropic energy conversion are observed in the LV region. In winter, the existence of a dipole structure is noted, whereas in summer it is a tripole structure. The rate of baroclinic energy conversion is characterized by intensification in winter, which is associated with a weakening of density stratification. At the same time, increased values are observed throughout the entire water area of the Lofoten Basin, many times exceeding the barotropic component. On the other hand, the barotropic energy conversion rate is higher in the summer compared to the baroclinic one.
3. In the Lofoten basin area of the Norwegian Sea, 48 mushroom-shaped dipoles with a life span from 19 to 45 days were recorded based on reanalysis data and Lagrangian maps for the period from 2013 to 2016. Due to the small amount of information about the dynamics of dipole structures, we have collected the most informative material on this topic, including descriptions of both theories about the generation and evolution of dipoles, as well as the results of field observations and model experiments. In the eastern part of the Lofoten Basin, a dipole was considered that existed for more than 3 weeks - from October 4 to November 5, 2013. The formation and evolution of the dipole are related to the topographic features of the Lofoten Basin, and this dipole structure is quasi-constant, clearly manifested in the field of

average current velocities. The width of the "cap" of the mushroom dipole is 170 km, its length is 150 km, and the width of the jet is 40-60 km. The analyzed dipole is characterized by high velocities in the jet (more than 0.15 m/s), as well as the presence of two multidirectional vortices with orbital velocities from 0.05 to 0.10 m/s. In the course of evolution, the size of the dipole first increased and then decreased. The vortex radii increased by 18 km for the cyclone and by 9 km for the anticyclone. Vertically, the dipole was clearly traced in the field of temperature anomalies in the layer from 0 to 800 m and to the very bottom in the field of currents.

4. Seasonal variability of parameters and thermohaline characteristics of mesoscale cyclones and anticyclones in the Lofoten Basin is analyzed. Using data from the META and the GLORYS12V1 reanalysis, it was found that during the year the maximum number of mesoscale cyclones and anticyclones was detected in the central and eastern parts of the Lofoten Basin. The number of anticyclones in the winter-spring period is greater than the number of cyclones, whereas in the summer-autumn period the difference is insignificant. The greatest differences in thermohaline characteristics of cyclone and anticyclone cores are manifested in temperature anomalies and significantly less pronounced in salinity and density anomalies. The maximum temperature anomalies were recorded in winter, the lowest in autumn. The upper part of the Lofoten Vortex is characterized by large thermohaline gradients compared to the lower part of the eddy.
5. Using data from reanalysis and the META in the Kuril region, four systems of topographic waves were detected, manifested as chains of cyclones and anticyclones and moving along isobaths. Anticyclones move in a southwesterly direction along the shelf in the form of shelf waves and along the outer part of the Kuril Trench in a northeasterly direction. Cyclones spread southwestward along the interior of the Kuril Trench and the topographic uplift. In all these cases, the eddies leave the shore on the right. It was found that among all the components of the effective beta effect, the contribution of topography to wave propagation was the largest. Among long-lived vortices with a lifespan of more than 10 days, the number of cyclones is twice as high as the number of similar anticyclones. On the other hand, anticyclones are

more stable structures, which are characterized by a large amplitude, orbital velocity and twice the life span compared to cyclones. Despite the fact that the eddy cores are localized in the upper layer up to 1000 m, mesoscale eddies "feel" the topographic slopes of the Kuril trench and changes in topography at depths of more than 5000 m, spreading along the isobaths. The lengths of such waves can exceed 500 km, and the period of one year. Their speed varies from a few cm/s to several tens of cm/s.

6. As a result, the maximum number of mesoscale eddies was recorded in the coastal region, as well as on the slopes of the Peruvian and Chilean trenches. The maximum number of anticyclones per cell (more than 120 eddies) is in the coastal zone of 38-48° S, while for cyclones similar estimates are recorded along the entire coastal part of South America. In the central part of the study area, there is an area from 20-30° S, in which the number of cyclones and anticyclones exceeds 80 vortices per cell. At 30-40° S, the number of eddies is noticeably reduced: about 30-40 per cell. On the other hand, the eddy kinetic energy in this region is maximal and reaches 120 cm²/s². This is due to the fact that local eddies have the highest amplitude, radius, and orbital velocity. Despite this, the mean kinetic energy is low, so it is the eddy mesoscale component that makes the greatest contribution. The EKE and MKE maxima are observed in the surface layer, gradually decreasing with increasing depth. In the 40-50° S, the number of eddies increases sharply, which is associated with the influence of the ACC. Most eddies have a radius of 25-75 km, an amplitude of more than 5 cm, an orbital velocity of 5-15 cm/s, and a lifetime of no more than 50 days. The largest number of eddies is observed from July to November, with maximum orbital velocities recorded from October to December. The westward-moving eddies are characterized by a meridional displacement. So, cyclones are shifting towards the pole, and anticyclones are moving towards the equator. An anticyclone with a lifetime of more than 1600 days and a distance of more than 4500 km was recorded. Unlike the South Atlantic, it has long-lived cyclones.

Based on the method of automatic identification of eddy structures in the Baltic Sea in 1993-2020, about 120 thousand mesoscale eddies were detected, 54.7% of which

are cyclones and 45.3% anticyclones. Most eddies have an amplitude of 0.05-0.25 m, a radius of 5-10 km, and a lifespan of 2-3 days. A small number of eddies have a radius of more than 30 km and a lifetime of more than 10 days. Some of the eddies are capable of moving 10-24 km per day, which corresponds to speeds of 11.6-27.8 cm/s. The largest number of eddies per grid cell is observed in the Kattegat, the Gulf of Riga and the Gulf of Gdansk, as well as in parts of the Gulf of Bothnia and the Gulf of Finland. Also, a significant number of eddies were detected over some banks and near the Aland Islands, Gotland and Bornholm. For some areas, the number of cyclones may be many times higher than the number of anticyclones. In the central part of the Baltic, the eddies are moving in a northeasterly direction, penetrating into the Gulf of Finland and the Gulf of Bothnia. In the Gulf of Riga and in the northern part of the Gulf of Bothnia, eddies form a cyclonic circulation. The long-lived eddies of the Baltic Sea are characterized by their proximity to topographic irregularities and movement along isobaths. The average ratio of the major and minor semi-axes of cyclones and anticyclones is 1.58, which makes it possible to describe most Baltic eddies using the theory of ellipsoidal eddies. This ratio also indicates both the stability of the Baltic eddies and the significant influence of the background current on their dynamics. For cyclones with a radius of more than 30 km, the axis ratio is close to 1. The maximum amplitudes of the eddies are recorded in the autumn-winter period, while the number of vortices is maximum in the spring-summer period. Significant positive linear trends are noted for the interannual values of the amplitude and number of eddies. In summer, the spatial dimensions of the eddies are maximum. A significant negative linear trend has been recorded for the interannual values of the eddy sizes. The area of the Baltic Sea occupied by mesoscale eddies has been increasing over the years. There is also a pronounced seasonal variability – in summer, vortices occupy 4% of the water area at one time, while in winter only 2%.

REFERENCES

1. Aguiar E. et al. Strong long-lived anticyclonic mesoscale eddies in the Balearic Sea: Formation, intensification, and thermal impact // *Journal of Geophysical Research: Oceans*. 2022. V. 127. e2021JC017589. <https://doi.org/10.1029/2021JC017589>
2. Akhtyamova A.F., Travkin V.S. Investigation of Frontal Zones in the Norwegian Sea // *Physical Oceanography*, 2022. 30(1), P. 62–77. doi:10.29039/1573-160X-2023-1-62-77
3. Alexeev V.A., Ivanov V.V., Repina I.A., Lavrova O.Y., Stanichny S.V. Convective structures in the Lofoten Basin based on satellite and Argo data // *Izvestiya, Atmospheric and Oceanic Physics*. 2016. Vol. 52. N. 9. P. 1064–1077. doi: 10.1134/S0001433816090036
4. Anikeyev V.G., Gerber E.M. Current state of horse mackerel *Trachurus murphyi* fishery in the South Pacific // *Trudy AtlantNIRO*. 2018. Vol 2, № 2. Kaliningrad: AtlantNIRO. P. 84–101. (in Russian).
5. Bashmachnikov I. L., Belonenko T. V., Kuibin P. A. Application of the theory of columnar Q-vortices with helical structure for the Lofoten vortex in the Norwegian Sea. *Vestnik SPbSU. Earth Sciences*, 2017a, V. 62, I 3, P. 221–236. <https://doi.org/10.21638/11701/spbu07.2017.301> (in Russian).
6. Bashmachnikov I.L. et al. On the vertical structure and stability of the Lofoten vortex in the Norwegian Sea // *Deep Sea Res I*. 2017b. V. 128. P. 1–27. <https://doi.org/10.1016/j.dsr.2017.08.001>
7. Bashmachnikov I. et al. Pattern of vertical velocity in the Lofoten vortex (the Norwegian Sea) // *Ocean Dynamics*. 2018. Vol. 68. P. 1711-1725. <https://doi.org/10.1007/s10236-018-1213-1>.
8. Belonenko T.V. Rossby waves observation in the Northwestern Pacific // *Sovremennye problemy distantsionnogo zondirovaniya Zemli iz kosmosa*. 2012. Vol. 9. № 3. P. 209–215. (in Russian).

9. Belonenko T.V., Volkov D.L., Norden Y.E., Ozhigin V.K. Water circulation in the Lofoten Basin of the Norwegian Sea // *Vestnik SPbSU. Earth Sciences*. 2014. V. 7. I. 2. P. 108–121. (in Russian).
10. Belonenko T.V., Bashmachnikov I.L., Koldunov A.V., Kuibin P.A. On Vertical Helical Structure of the Vortex: the Lofoten Vortex of the Norwegian Sea // *Izvestiya, Atmospheric and Oceanic Physics*. 2017. V. 53. P. 641–649. <https://doi.org/10.1134/S0001433817060032>
11. Belonenko T.V., Sandalyuk N.V. Temporal variability of mesoscale eddies characteristics in the Australian–Antarctic basin (based on satellite data) // *Sovremennye problemy distantsionnogo zondirovaniya Zemli iz kosmosa*. 2018. V. 15. №4. P. 189–199. DOI: 10.21046/2070-7401-2018-15-4-189-199 (in Russian).
12. Belonenko T.V., Volkov D.L., Koldunov A.V. Shelf Waves in the Beaufort Sea Based on Hydrodynamic Model MITgcm // *Oceanology*. 2018a, 58. P. 778–785. <https://doi.org/10.1134/S0001437018060024>
13. Belonenko T.V., Koldunov A.V., Sentyabov E.V., Karsakov A.L. Thermohaline structure of the Lofoten vortex in the Norwegian sea based on field research and hydrodynamic modeling. *Vestn S. Petersbur. Un-ta, Earth sciences*. 2018b. 63 (4). P. 502-519. <https://doi.org/10.21638/spbu07.2018.406> (in Russian).
14. Belonenko T., Frolova A., Gnevyshev V. Detection of waveguide for Rossby waves using satellite altimetry in the Antarctic Circumpolar Current // *Intern. J. Remote Sensing*. 2020a. V. 41. Iss. 16. P. 6232–6247. DOI: 10.1080/01431161.2020.1752955.
15. Belonenko T. et al. Evaluation of heat and salt transports by mesoscale eddies in the Lofoten Basin // *Russ. J. Earth. Sci.* 2020b. V. 20. ES6011. DOI:10.2205/2020ES000720.
16. Belonenko T. et al. Topographic experiments over dynamical processes in the Norwegian Sea, *Russ. J. Earth. Sci.* 2021a. V. 21. ES1006. doi:10.2205/2020ES000747.

17. Belonenko T. et al. Interaction of the Lofoten vortex with a satellite cyclone // *Pure and Applied Geophysics*. 2021b. V. 178. P. 287–300. <https://doi.org/10.1007/s00024-020-02647-1>
18. Belonenko T.V., Travkin V. S., Kochnev A.V. Review of studies on the distribution of Antarctic krill accumulations in the Scotia Sea and analysis of mesoscale dynamics of its habitat // *Vestnik of Saint Petersburg University. Earth Sciences*. 2024, 69(1), P. 108–127. <https://doi.org/10.21638/spbu07.2024.106> (in Russian).
19. Benilov E.S. Stability of a Two-Layer Quasigeostrophic Vortex over Axisymmetric Localized Topography // *J. Phys. Oceanogr.* 2005. V. 35. No. 1. P. 123–130. <https://doi.org/10.1175/JPO-2660.1>
20. Bloshkina E.V., Ivanov V.V. Convective structures in the Norwegian and Greenland seas according to the high spatial resolution simulations // *Tr. Gidrometeorol. Nauchno. Issled. Tsentra Ross. Fed.* 2016, №. 361, P. 146–168. (in Russian).
21. Borodin E.V., Churin D.A., Chernyshkov P.P. The influence of water dynamics on the biomass and distribution of biological resources of the pelagic zone of the southern parts of the Atlantic and Pacific Oceans // *IKBFU's Vestnik. Series: Natural Sciences*. 2014. V. 7. P. 142–154. (in Russian).
22. Bosse A. et al. Dynamical controls on the longevity of a non-linear vortex: the case of the Lofoten Basin Eddy // *Scientific Reports*. 2019. V. 9. 13448. <https://doi.org/10.1038/s41598-019-49599-8>
23. Buchwald V.T., Adams J.K. The Propagation of Continental Shelf Waves // *Proc. Royal Society of London. Ser. A. Mathematical and Physical Sciences*. 1968. V. 305. No. 1481. P. 235–250. DOI: 10.1098/rspa.1968.0115.
24. Budyansky M.V., Lebedeva M.A., Belonenko T.V. et al. Analysis of oceanographic conditions for Japanese mackerel fishery based on satellite and modelling data in the South Kuril Straitin 2020–2022 // *Sovremennye problemy distantsionnogo zondirovaniya Zemli iz kosmosa*. 2024. V. 21. № 2. P. 286–299. DOI: 10.21046/2070-7401-2024-21-2-286-299 (in Russian).

25. Bulatov N.V., Lobanov V.B. Investigation of mesoscale eddies to the east of the Kuril Islands on the base of meteorological satellites data // *Issledovanie Zemli iz Kosmosa*. 1983. № 3. P. 40–47. (in Russian).
26. Carnevale G.F., Kloosterziel R.C., van Heijst G.J.F. Propagation of barotropic vortices over topography in a rotating tank // *J. Fluid Mech.* 1991. V. 233. P. 119–125. <https://doi.org/10.1017/S0022112091000411>
27. Carton X.J. The merger of homostrophic shielded vortices // *EPL (Europhysics Letters)*. 1992. V. 18. No. 8. P. 697–703. DOI 10.1209/0295-5075/18/8/006
28. Carton X. Hydrodynamical modeling of oceanic vortices // *Surveys in Geophysics*. 2001. V. 22. P. 179-263. <https://doi.org/10.1023/A:1013779219578>
29. Chelton D.B. et al. Global observations of large oceanic eddies // *Geophysical Research Letters*. 2007. V. 34. №. 15. P. 1-5. doi:10.1029/2007GL030812
30. Chelton D.B., Schlax M.G., Samelson R.M. Global observations of nonlinear mesoscale eddies // *Progress in Oceanography*. 2011a. V. 91. P. 167-216. doi:10.1016/j.pocean.2011.01.002
31. Chelton D.B., Gaube P., Schlax M.G., Early J.J., Samelson R.M. The influence of nonlinear mesoscale eddies on near-surface oceanic chlorophyll // *Science*. 2011b. V. 334. I. 6054. P. 328–332. doi:10.1126/science.1208897
32. Cunningham S.A. Circulation and volume flux of the North Atlantic using synoptic hydrographic data in a Bernoulli inverse // *J. Marine Res.* 2000. V. 58. P. 1–35. <https://doi.org/10.1357/002224000321511188>
33. Cunningham S.A. et al. Transport and Variability of the Antarctic Circumpolar Current in Drake Passage // *J. Geophysical Research*. 2003. V. 108. I. C5. 8084. DOI: 10.1029/2001JC001147.
34. Cushman-Roisin B. *Introduction to Geophysical Fluid Dynamics*. Prentice Hall. 1994. 320 pp.
35. D’Asaro E.A. Observations of small eddies in the Beaufort Sea // *Journal of Geophysical Research: Oceans*. 1988. V. 93, I. C6. P. 6669–6684. <https://doi.org/10.1029/JC093iC06p06669>

36. Deser C., Alexander M.A., Timlin M.S. Evidence for a Wind-Driven Intensification of the Kuroshio Current Extension from the 1970s to the 1980s // *J. Climate*. 1999. V. 12. P. 1697–1706. [https://doi.org/10.1175/1520-0442\(1999\)012<1697:EFAWDI>2.0.CO;2](https://doi.org/10.1175/1520-0442(1999)012<1697:EFAWDI>2.0.CO;2).
37. Dong C. et al. Three-dimensional oceanic eddy analysis in the Southern California Bight from a numerical product // *J. Geophys. Res.* 2012. V. 117. C00H14. DOI: 10.1029/2011JC007354.
38. Drange H. et al. (Eds.). *The Nordic Seas: An Integrated Perspective* // American Geophysical Union. 2005. V. 158. P. 366. <https://doi.org/10.1029/158GM03>.
39. Dubishchuk M.M., Features of fishing and biological condition of the Peruvian horse mackerel *Trachurus murphyi* in the open waters of the central subregion of the Southeast Pacific Ocean in August-October 2020, *Trudy AtlantNIRO*, 2021, Vol. 5, No. 1(11), pp. 122–135 (in Russian).
40. Eden C., Böning C. Sources of Eddy Kinetic Energy in the Labrador Sea // *Journal of Physical Oceanography*. 2002. V. 32, I. 12. P. 3346–3363. doi:10.1175/1520-0485(2002)032<3346:SOEKEI>2.0.CO;2
41. Efimov V.V., Kulikov E.A., Rabinovich A.B., Fine I.V. *Waves in the ocean boundary regions*, Leningrad, 1985, 250 p. (in Russian).
42. Elkin D.N., Zatsepin A.G. Laboratory Investigation of the Mechanism of the Periodic Eddy Formation Behind Capes in a Coastal Sea // *Oceanology*. 2013. V. 53. No. 1. P. 24–35. DOI: 10.1134/S0001437012050062
43. Faghmous J. et al. A daily global mesoscale ocean eddy dataset from satellite altimetry // *Sci Data*. 2015. V. 2. 150028. <https://doi.org/10.1038/sdata.2015.28>
44. FAO. 2022. *The state of global fisheries and aquaculture – 2022. On the way to the “blue” transformation*. Rome, FAO. <https://doi.org/10.4060/cc0461ru> (In Russian).
45. Fedorov K.N. 1983. *The Physical Nature and Structure of Oceanic Fronts*. Leningrad: Gidrometeoizdat, 296 p. (in Russian).

46. Fedorov A.M., Bashmachnikov I.L., Belonenko T.V. Winter Convection in the Lofoten Basin according to ARGO Buoys and Hydrodynamic Modeling // Vestnik of St Petersburg University. Earth Sciences. 2019, 64(3), P. 491–511. doi:10.21638/spbu07.2019.308 (in Russian).
47. Fedorov A.M., Belonenko T.V. Interaction of mesoscale vortices in the Lofoten Basin based on the GLORYS database // Russ. J. Earth. Sci. 2020. V. 20. ES2002. doi:10.2205/2020ES000694.
48. Fer I. et al. The Dissipation of Kinetic Energy in the Lofoten Basin Eddy // Journal of Physical Oceanography. 2018. V. 48. P. 1299–1316. DOI: 10.1175/JPO-D-17-0244.1
49. Fernández-Castro B. et al. Breaking of internal waves and turbulent dissipation in an anticyclonic mode water eddy // Journal of Physical Oceanography. 2020. V. 50, I. 7. P. 1893–1914. doi:10.1175/JPO-D-19-0168.1
50. Flor J.B., van Heijst G.J.F., Deflos R. Decay of dipolar vortex structures in a stratified fluid // Physics of Fluids. 1995. V. 7. I. 2. P. 374–379.
51. Gaube P., McGillicuddy Jr. D.J., Moulin A.J. Mesoscale eddies modulate mixed layer depth globally // Geophysical Research Letters. 2019. V. 46. P. 1505–1512. DOI: 10.1029/2018GL080006.
52. Gill A.E., Green J.S.A., Simmons A.J. Energy partition in the large-scale ocean circulation and the production of mid-ocean eddies // Deep Sea Research and Oceanographic Abstracts. 1974. V. 21. I. 7. P. 499–528. [https://doi.org/10.1016/0011-7471\(74\)90010-2](https://doi.org/10.1016/0011-7471(74)90010-2)
53. Ginzburg A.I., Fedorov K.N. The evolution of currents in the ocean // Dokl. USSR Academy of Sciences. 1984a. V. 276. I. 2. P. 481–484. (in Russian).
54. Ginzburg A.I., Fedorov K.N. Mushrooms currents in the ocean (satellite derived data). Earth Observations and Remote Sensing. 1984b, V. 3, P. 18–26. (in Russian).
55. Glubokov A.I., Popova N.R., Glubokovskiy M.K. Commercial fish of the South East Pacific: international management measures and stocks status // Trudy VNIRO. 2018, V. 174, P. 21–29. (in Russian).

56. Gnevyshev V.G., Frolova A.V., Kubryakov A.A. et al. Interaction between Rossby Waves and a Jet Flow: Basic Equations and Verification for the Antarctic Circumpolar Current // *Izv. Atmos. Ocean. Phys.* 2019, V. 55, P. 412–422. <https://doi.org/10.1134/S0001433819050074>
57. Gnevyshev V.G., Frolova A.V., Koldunov A.V., Belonenko T.V. Topographic Effect for Rossby Waves on a Zonal Shear Flow. *Fundamental and Applied Hydrophysics*. 2021a, 14(1), P. 4–14. <https://doi.org/10.7868/S2073667321010019>
58. Gnevyshev V.G. et al. On Agulhas Eddies and Rossby Waves Travelling by Forcing Effects // *Russian J. Earth Sciences*. 2021b. V. 21. No. 5. ES5003. DOI: 10.2205/2021ES000773.
59. Gnevyshev V.V., Frolova A.V., Belonenko T.V. Topographic Effect for Rossby Waves on Non-Zonal Shear Flow // *Water Resources*. 2022. V. 49. No. 2. P. 240–248. DOI: 10.7868/S2073667321010019.
60. Gnevyshev V.G., Travkin V.S., Belonenko T.V. Topographic Factor and Limit Transitions in the Equations for Subinertial Waves // *Fundamental and Applied Hydrophysics*. 2023a, 16(1), P. 8–23. <https://doi.org/10.59887/fpg/92rg-6t7h-m4a2>
61. Gnevyshev V.G., Travkin V.S., Belonenko T.V. Group Velocity and Dispersion of Buchwald and Adams Shelf Waves. A New Analytical Approach // *Fundamental and Applied Hydrophysics*. 2023b, V. 16, I. 2, P. 8–20. Doi:10.59887/2073–6673.2023.16(2)-1
62. Gnevyshev V.V., Travkin V.S., Belonenko T.V. Mixed Topographic-Planetary Waves in a Stratified Ocean on a Background Flow // *Pure Appl. Geophys.* 2024. V. 181. P. 2359–2371. <https://doi.org/10.1007/s00024-024-03527-8>
63. Gordeeva S.M., Zharova A.D. Operational assessment of fisheries in the Southeast Pacific // *Uchenye zapiski RGGMU*, 2016, No. 44, P. 96–103 (in Russian).

64. Gordeeva S. et al. Statistical analysis of long-lived mesoscale eddies in the Lofoten Basin from satellite altimetry // *Advances in Space Research*. 2021. V. 68. 2. P. 364–377. DOI:10.1016/j.asr.2020.05.043.
65. Gurova E. S., Ivanov A.Yu. Appearance of Sea Surface Signatures and Current Features in the South-East Baltic Sea on the MODIS and SAR images // *Issledovanie Zemli iz kosmosa*, 2011, No. 4, P. 41–54. (in Russian).
66. Hebert D. The available potential energy of an isolated feature // *Journal of Geophysical Research: Oceans*. 1988. V. 93. I. C1. P. 556–564. <https://doi.org/10.1029/JC093iC01p00556>
67. Hughes C.W., Miller P.I. Rapid water transport by long-lasting modon eddy pairs in the southern midlatitude oceans // *Geophysical Research Letters*. 2017. V. 44. P. 1-10. <https://doi.org/10.1002/2017GL075198>
68. Ivanov V.V., Korablev A.A. Formation and regeneration of the pycnocline lens in the Norwegian Sea // *Meteorol. and Hydrol.* 1995a. V. 9, P. 102–110. (in Russian).
69. Ivanov V.V., Korablev A.A. Dynamics of pycnocline lens in the Norwegian sea // *Meteorol. and Hydrol.* 1995b, V. 10, P. 55–62. (in Russian).
70. Isachsen P.E. Baroclinic instability and eddy tracer transport across sloping bottom topography: How well does a modified Eady model do in primitive equation simulations? // *Ocean Modell.* 2011. V. 39. P. 183–199. <https://doi.org/10.1016/j.ocemod.2010.09.007>
71. Isachsen P.E. Baroclinic instability and the mesoscale eddy field around the Lofoten Basin // *J. Geophys. Res.* 2015. V. 120. No. 4. P. 2884–2903. <https://doi.org/10.1002/2014JC010448>
72. Koldunov A. V. and Belonenko T. V. Hydrodynamic Modeling of Vertical Velocities in the Lofoten Vortex. *Izvestiya, Atmospheric and Oceanic Physics*, 2020, Vol. 56, No. 5, pp. 502–511. <https://doi.org/10.1134/S0001433820040040>.
73. Lappo S.S. Mesoscale dynamic ocean processes excited by the atmosphere // Moscow: Nauka, 1979. 181 p. (in Russian).

74. Larichev V. D., Reznik G. M. On two-dimensional solitary Rossby waves // *Doklady Akademii Nauk*, 1976, 231(5), P. 1077–1079. (in Russian).
75. LeBlond P. H., Mysak L. A., *Waves in the ocean*, Amsterdam; Oxford; New York: Elsevier Scientific Publ. Company, 1981, 602 p.
76. Lobanov V.B., Rogachev K.A., Bulatov N.V., Lomakin A.F., Tolmachev K.P. Long-term evolution of warm-core ring of Kuroshio // *Proceedings of the USSR Academy of Sciences*. 1991. V. 317. № 4. P. 984–988 (in Russian).
77. Malinin V.N., Gordeeva S.M. *Fishery oceanology of south-east Pacific. Volume 1. Variability of habitat factors*. RGGMU Publishing House, 2009. 278 p. (in Russian).
78. Malysheva A. A., Belonenko T. V., Iakovleva D. A. Characteristics of two eddies of different polarity in the Agulhas Current. *Gidrometeorologiya i Ekologiya*. 2022, V. 68, P. 478–493. (in Russian). doi: 10.33933/2713-3001-2022-68-478-493.
79. Mikaelyan A.S., Zatsepin A.G., Kubryakov A.A. Effect of Mesoscale Eddy Dynamics on Bioproductivity of the Marine Ecosystems (Review) // *Physical Oceanography*, [e-journal], 2020. 27(6), P. 590–618. doi:10.22449/1573-160X-2020-6-590-618
80. Monin A.S., Kamenkovich V.M., Kort V.G. *Variability of the oceans* // Leningrad: Gidrometeoizdat, 1974. 261 p. (in Russian).
81. Nezlin M. V. Rossby solitons (Experimental investigations and laboratory model of natural vortices of the Jovian Great Red Spot type) // *Sov. Phys. Usp.* 1986. V. 29, P. 807–842. DOI: 10.1070/PU1986v029n09ABEH003490
82. Novoselova E.V., Belonenko T.V. Isopycnal Advection in the Lofoten Basin of the Norwegian Sea. *Fundamental and Applied Hydrophysics*. 2020, 13(3), P. 56–67. <https://doi.org/10.7868/S2073667320030041> (in Russian).
83. Novoselova E.V., Travkin V.S., Lebedeva M.A., Udalov A.A., Budyansky M.V., Belonenko T.V. Features of the vortex structures in the fields of Eulerian and Lagrangian hydrological characteristics for the Northwest Pacific // *Vestnik of Saint Petersburg University. Earth Sciences*. 2024, 69 (2). P. 372–388. <https://doi.org/10.21638/spbu07.2024.209> (in Russian).

84. Jakobsen P.K. et al. Near-surface circulation in the northern North Atlantic as inferred from Lagrangian drifters: Variability from the mesoscale to interannual // *J. Geophys. Res.* 2003. V. 108. No. C8. 3251. <https://doi.org/10.1029/2002JC001554>, 2003.
85. Jędrasik J., Kowalewski M. Mean annual and seasonal circulation patterns and long-term variability of currents in the Baltic Sea // *Journal of Marine Systems.* 2018. V. 193. P. 1-26. <https://doi.org/10.1016/j.jmarsys.2018.12.011>
86. Johan H., Fang H. Horizontal vortex ring motion in linearly stratified media // *Physics of Fluids.* 1997. V.9. I. 9. P. 2605–2616.
87. IOC, SCOR and IAPSO. The international thermodynamic equation of seawater - 2010: Calculation and use of thermodynamic properties // Intergovernmental Oceanographic Commission, Manuals and Guides. 2010. No. 56. UNESCO (English). 196 p.
88. Kämpf J., Backhaus J.O., Fohrmann H. Sediment-induced slope convection: Two-dimensional numerical case studies // *Journal of Geophysical Research.* 1999. V. 104. No. C9. P. 20509-20522. <https://doi.org/10.1029/1999JC900157>
89. Kang D., Curchitser E.N. On the evaluation of seasonal variability of the ocean kinetic energy // *Journal of Physical Oceanography.* 2017. V. 47. I. 7. P. 1675–1683. <https://doi.org/10.1175/JPO-D-17-0063.1>
90. Kara A.B., Rochford P.A., Hurlburt H.E. An optimal definition for ocean mixed layer depth // *Journal of Geophysical Research.* 2000. V. 105. I. C7. P. 16803–16821.
91. Kawai H. Hydrography of the Kuroshio Extension. p. 235–352. In *Kuroshio, Its Physical Aspects*, ed. by H. Stommel and K. Yoshida. University of Tokyo Press, 1972. 527 pp.
92. Khvoles R., McWilliams J.C., Kizner Z. Noncoincidence of separatrices in two-layer modons // *Physics of Fluids.* 2007. V. 19. 056602. <https://doi.org/10.1063/1.2731741>
93. Khudyakova S.P., Travkin V.S., Belonenko T.V. Mesoscale eddies of the Aleutian Trench // *Sovremennye problemy distantsionnogo zondirovaniya Zemli iz*

- kosmosa. 2023. V. 20. № 6. P. 211–221. DOI: 10.21046/2070-7401-2023-20-6-211-221
94. Killworth P.D. Deep convection in the World Ocean // *Reviews of Geophysics*. 1983. V. 21. I. 1. P. 1–26. <https://doi.org/10.1029/rg021i001p00001>
95. Kitano K. Some properties of the warm eddies generated in the confluence zone of the Kuroshio and Oyashio Currents // *Journal of Physical Oceanography*. 1975. V. 5. P. 245–352. [https://doi.org/10.1175/1520-0485\(1975\)005<0245:SPOTWE>2.0.CO;2](https://doi.org/10.1175/1520-0485(1975)005<0245:SPOTWE>2.0.CO;2)
96. Köhl A. Generation and Stability of a Quasi-Permanent Vortex in the Lofoten Basin // *Journal of Physical Oceanography*. 2007. V. 37. No. 11. P. 2637–2643.
97. Kurkin A. et al. Comparative analysis of the first baroclinic Rossby radius in the Baltic, Black, Okhotsk, and Mediterranean seas // *Russ. J. Earth. Sci.* 2020. V. 20. ES4008. DOI:10.2205/2020ES000737.
98. Lahaye N., Zeitlin V., Dubos T. Coherent dipoles in a mixed layer with variable buoyancy: theory compared to observations // *Ocean Modelling*. 2020. V. 153. 101673. <https://doi.org/10.1016/j.ocemod.2020.101673>
99. Lass H.U., Mohrholz V. On dynamics and mixing of inflowing saltwater in the Arkona Sea // *J. Geophys. Res.* 2003. V. 108. No. C2. 3042. DOI: 10.1029/2002JC001465.
100. Lehmann A. et al. Salinity dynamics of the Baltic Sea // *Earth Syst. Dynam.* 2022. V. 13. P. 373–392. <https://doi.org/10.5194/esd-13-373-2022>.
101. Longuet-Higgins M.S. On the trapping of waves along a discontinuity of depth in a rotating ocean // *J. Fluid Mechanics*. 1968a. V. 31. P. 417–434. DOI: 10.1017/s0022112068000236.
102. Longuet-Higgins M.S. Double Kelvin waves with continuous depth profiles // *J. Fluid Mechanics*. 1968b. V. 34. P. 49–80. DOI: 10.1017/s002211206800176x.
103. McGillicuddy Jr. D.J. Mechanisms of Physical-Biological-Biogeochemical Interaction at the Oceanic Mesoscale // *Annual Review of Marine Science*. 2016. V. 8. P. 125–159. <https://doi.org/10.1146/annurev-marine-010814-015606>.

104. Manucharyan G.E., Timmermans M.-L. Generation and separation of mesoscale eddies from surface ocean fronts // *Journal of Physical Oceanography*. 2013. V. 43. P. 2545–2556. <https://doi.org/10.1175/JPO-D-13-094.1>
105. Martínez-Moreno J. et al. Kinetic energy of eddy-like features from sea surface altimetry // *Journal of Advances in Modeling Earth Systems*. 2019. V. 11. I. 10. P. 3090–3105. <https://doi.org/10.1029/2019MS001769>
106. Mikaelyan A.S. et al. Case where a mesoscale cyclonic eddy suppresses primary production: A Stratification-Lock hypothesis // *Progress in Oceanography*. 2023. V. 212. 102984. DOI: 10.1016/j.pocean.2023.102984.
107. de Boyer Montégut C. et al. Mixed layer depth over the global ocean: An examination of profile data and a profile-based climatology // *J. Geophys. Res.* 2004. V. 109. C12003. DOI:10.1029/2004JC002378.
108. K.A. Mork, J. Blindheim Variations in the Atlantic inflow to the Nordic Seas, 1955-1996 // *Deep-Sea Research I*. 2000. V. 47. P. 1035-1057.
109. Mysak L.A., LeBlond P.H., Emery W. J. Trench Waves // *J. Physical Oceanography*. 1979. V. 9. P. 1001–1013. DOI: 10.1175/1520-0485(1979)009<1001:TW>2.0.CO;2.
110. Nan F. et al. Weakening of the Kuroshio intrusion into the South China Sea over the past two decades // *Journal of Climate*. 2013. V. 26. P. 8097–8110. <https://doi.org/10.1175/JCLI-D-12-00315.1>
111. Nilsen J.E., Falck E. Variations of mixed layer properties in the Norwegian Sea for the period 1948—1999 // *Progress in Oceanography*. 2006. V. 70. P. 58–89.
112. Nitani H. Beginning of the Kuroshio. P. 129–163. In H. Stommel & K. Yoshida (Eds.), *Kuroshio: Its physical aspects*. University of Tokyo Press, 1972. 527 pp.
113. Pegliasco C. et al. META3.1exp: a new global mesoscale eddy trajectory atlas derived from altimetry // *Earth Syst. Sci. Data*. 2022. V. 14. P. 1087–1107. <https://doi.org/10.5194/essd-14-1087-2022>.

114. Prants S.V. et al. Lagrangian study of transport and mixing in a mesoscale eddy street. *Ocean Modelling*. 2011a. V. 38. P. 114–125. <https://doi.org/10.1016/j.ocemod.2011.02.008>
115. Prants S.V., Uleysky MYu., Budyansky M.V. Numerical simulation of propagation of radioactive pollution in the ocean from the Fukushima-Dai-ichi nuclear plant // *Doklady Earth Sciences*. 2011b. V. 439. P. 1179–1182. <https://doi.org/10.1134/S1028334X11080277>
116. Prants S.V. Chaotic Lagrangian transport and mixing in the ocean // *The European Physical Journal Special Topics*. 2014. V. 223. P. 2723–2743. <https://doi.org/10.1140/epjst/e2014-02288-5>
117. Prants S.V., Budyansky M.V., Uleysky M.Y. Identifying Lagrangian fronts with favorable fishery conditions // *Deep Sea Res. I*. 2014a. V. 90. P. 27–35. <https://doi.org/10.1016/j.dsr.2014.04.012>.
118. Prants S.V., Budyansky M.V., Uleysky MYu. Lagrangian fronts in the ocean // *Izvestiya, Atmospheric and Oceanic Physics*. 2014b. V. 50. P. 284–291. <https://doi.org/10.1134/S0001433814030116>
119. Prants S.V., Uleysky MYu., Budyansky M.V. Lagrangian oceanography: large-scale transport and mixing in the ocean. *Physics of earth and space environments*. Springer-Verlag: Berlin, Germany, 2017. 273 p.
120. Prants S.V., Budyansky M.V., Uleysky M.Y. How eddies gain, retain, and release water: A case study of a Hokkaido anticyclone // *Journal of Geophysical Research: Oceans*. 2018. V. 123. P. 2081–2096. <https://doi.org/10.1002/2017JC013610>
121. Prants S.V. Trench Eddies in the Northwest Pacific: an Overview // *Izv. Atmos. Ocean. Phys.* 2021, 57, P. 341–353. <https://doi.org/10.1134/S0001433821040216>
122. Radtke H. et al. Investigating interdecadal salinity changes in the Baltic Sea in a 1850–2008 hindcast simulation // *Clim. Past*. 2020. V. 16. P. 1617–1642. <https://doi.org/10.5194/cp-16-1617-2020>.

123. Raj R.P. et al. Quantifying mesoscale eddies in the Lofoten Basin // *J. Geophys. Res. Oceans*. 2016. V. 121. P. 4503–4521. DOI:10.1002/2016JC011637.
124. Raj R.P. et al. Interaction between mesoscale eddies and the gyre circulation in the Lofoten Basin // *Journal of Geophysical Research: Oceans*. 2020. V. 125. I. 7. e2020JC016102. <https://doi.org/10.1029/2020JC016102>
125. Reid R.O., Elliott B.A., Olson D.B. Available potential energy: A clarification // *Journal of Physical Oceanography*. 1981. V. 11. I. 1. P. 15–29. [https://doi.org/10.1175/1520-0485\(1981\)011<0015:APEAC>2.0.CO;2](https://doi.org/10.1175/1520-0485(1981)011<0015:APEAC>2.0.CO;2)
126. Reißmann J.H. Integrale Eigenschaften von mesoskaligen Wirbelstrukturen in den tiefen Becken der Ostsee // *Marine Science Reports*. 2002. No. 52. P. 149. DOI: 10.12754/msr-2002-0052.
127. Reißmann J.H. An algorithm to detect isolated anomalies in three-dimensional stratified data fields with an application to density fields from four deep basins of the Baltic Sea // *Journal of Geophysical Research*. 2005. V. 110. C12018. DOI: 10.1029/2005JC002885.
128. Reißmann J.H. et al. Vertical mixing in the Baltic Sea and consequences for eutrophication – A review // *Progress in Oceanography*. 2009. V. 82. P. 47–80. DOI: 10.1016/j.pocean.2007.10.004.
129. Samko E.V., Bulatov N.V., Kapshiter A.V. Characteristics of anticyclonic various vortices and their impact on the fishing of the saury and neon flying squid to the southeast of Hokkaido // *Sovrem. Probl. Distantionnogo Zondirovaniya Zemli Kosmosa*, 2007, V. 1, P. 357–369. (in Russian).
130. Sandalyuk N.V., Bosse A., Belonenko T.V. The 3D structure of Mesoscale Eddies in the Lofoten Basin of the Norwegian Sea: a composite analysis from altimetry and in situ data // *Journal of Geophysical Research: Oceans*. 2020. V. 125. P. 1–6. <https://doi.org/10.1029/2020JC016331>
131. Sandalyuk N.V., Belonenko T.V. Seasonal Variability of the Thermohaline Structure of the Mesoscale Eddies in the Lofoten Basin. *Fundamentalnaya i Prikladnaya Gidrofizika*. 2021, 14, 1, 15–30. doi: 10.7868/S2073667321010020 (in Russian).

132. Sandalyuk N.V., Belonenko, T.V., Koldunov A.V. Shelf Waves in the Great Australian Bight Based on Satellite Altimetry Data // *Izv. Atmos. Ocean. Phys.* 2021, V. 57, P. 1117–1126. <https://doi.org/10.1134/S0001433821090619>
133. Sauskan V. I. The raw material base of fishing in the world Ocean: a textbook for university students. Kaliningrad State Technical University. Kaliningrad: KSTU Publishing House, 2006, 294 p. (in Russian).
134. Seiki A. et al. The oceanic response to the Madden-Julian oscillation and ENSO // *SOLA*. 2009. V. 5. P. 93–96. DOI: 10.2151/sola.2009-024.
135. Shapiro G.I. The synoptic variability of the horizontally nonhomogeneous upper ocean layer // *Okeanologiya*. 1985. V. 25. № 5. P. 733–739.
136. Shchepetkin A.F. Interaction of turbulent barotropic shallow-water flow with topography // *Proceedings of Hawaiian Winter Aha Huliko'a Workshop*, P. Müller and D. Henderson (eds). HI, Honolulu. 1995. P. 225–237.
137. Søiland H., Chafik L., Rossby T. On the long-term stability of the Lofoten Basin Eddy // *J Geophys Res Oceans*. 2016. V. 121. P. 4438–4449. <https://doi.org/10.1002/2016jc011726>
138. Stammer D., Wunsch C. Temporal changes in eddy energy of the oceans // *Deep Sea Res. Part II*. 1999. V. 46. P. 77–108.
139. Stern M.E. Minimal properties of planetary eddies // *Journal of Marine Research*. 1975. V. 33. P. 1–5.
140. Stern M.E., Voropaev S.I. Formation of vorticity fronts in shear flow // *Physics of Fluids*. 1984. V. 27. P. 848–855.
141. Tóth G., Házi G. Merging of shielded Gaussian vortices and formation of a tripole at low Reynolds numbers // *Physics of Fluids*. 2010. V. 22. 053101. <https://doi.org/10.1063/1.3428539>
142. Tikhonova N.A., Zakharchuk E.A., Gusev A.V., Travkin V.S., Pavlovsky A.A. The Influence of Modern Alluvial Areas on Sea Level Changes in The Neva Bay During Storm Surges in The Conditions of Operation of The Saint Petersburg Flood Prevention Faculty Complex // *Fundamental and Applied Hydrophysics*.

2024, 17(2), P. 103–118. [https://doi.org/10.59887/2073-6673.2024.17\(2\)-9](https://doi.org/10.59887/2073-6673.2024.17(2)-9) (In Russian).

143. Travkin V.S., T.V. Belonenko Seasonal variability of mesoscale eddies of the Lofoten Basin using satellite and model data // Russ. J. Earth. Sci. 2019. V. 19. ES5004. doi:10.2205/2019ES000676.

144. Travkin V.S., Belonenko T.V., Mixed layer depth in winter convection in the Lofoten Basin in the Norwegian Sea and assessment methods // Hydrometeorology and Ecology (Proceedings of the Russian State Hydrometeorological University). 2020. V. 59, P. 67–83. (In Russian). doi: 10.33933/2074-2762-2020-59-67-83

145. Travkin V.S., Belonenko T.V. Study of the mechanisms of vortex variability in the Lofoten Basin based on the energy analysis // Physical Oceanography [e-Journal]. 2021. V. 28. P. 294–308. <https://doi.org/10.22449/1573-160X-2021-3-294-308>

146. Travkin V.S., Belonenko T.V., Kochnev A.V. Topographic waves in the Kuril region // Sovremennye problemy distantsionnogo zondirovaniya Zemli iz kosmosa. 2022a. V. 19. №5. P. 222–234. DOI: 10.21046/2070-7401-2022-19-5-222-234 (In Russian).

147. Travkin V.S., Belonenko T.V., Kubryakov A.A. Cold Spot over the Lofoten Vortex. Izv. Atmos. Ocean. Phys. 2022b, V. 58, P. 1458–1469. <https://doi.org/10.1134/S0001433822120246>

148. Travkin V., Belonenko T., Budyansky M., Prants S., Uleysky M., Gnevyshev V., Raj R. Quasi-Permanent Mushroom-like Dipole in the Lofoten Basin, Pure and Applied Geophysics // 2022c. V. 179. I. 6. P. 465–482. DOI: 10.1007/s00024-021-02922-9.

149. Travkin V.S., Zhmur V.V., Belonenko T.V. Contribution of mesoscale eddies to energy of the Lofoten Basin // Russ. J. Earth. Sci. 2022d, V. 22, ES4002, 10.2205/2022ES000802. (In Russian).

150. Travkin V.S., Akhtyamova A. F. Spatial Variability of the Frontal Zones and its Eddies Generated in the Norwegian Sea // Russian Journal of Earth Sciences. 2023. No. 3. P. 1–14. DOI: <https://doi.org/10.2205/2023es000844>.

151. Travkin V.S., Belonenko T.V., Kochnev A.V., Feoktistova V.N. Mesoscale eddies in the South Pacific Ocean // *Sovremennye problemy distantsionnogo zondirovaniya Zemli iz kosmosa*. 2024a. V. 21. № 1, P. 286–298. DOI: 10.21046/2070-7401-2024-21-1-286-298 (in Russian).
152. Travkin V.S., Tikhonova N.A., Zakharchuk E.A. // Mesoscale Eddies of the Baltic Sea according to the Physical Reanalysis. *Russian Meteorology and Hydrology*. 2024b. No. 49. P. 784–794. <https://doi.org/10.3103/S1068373924090048>
153. Travkin V.S., Gnevyshev V.G., Belonenko T.V. Mesoscale eddies on the continental slope of the New Zealand Plateau based on altimetry data // *Sovremennye problemy distantsionnogo zondirovaniya Zemli iz kosmosa*. 2024c. V. 21. №3. P. 221–233, DOI: 10.21046/2070-7401-2024-21-3-221-233 (in Russian).
154. Travkin V.S., Tikhonova N.A., Zakharchuk E.A. // Characteristics of Marine Heatwaves of the Baltic Sea for 1993-2022 and Their Driving Factors. *Pure and Applied Geophysics*. 2024d. V. 181. P. 2373–2387. <https://doi.org/10.1007/s00024-024-03504-1>
155. Trodahl M., Isachsen P.E. Topographic influence on baroclinic instability and the mesoscale eddy field in the Northern North Atlantic Ocean and the Nordic Seas // *Journal of Physical Oceanography*. 2018. V. 48, I. 11. P. 2593–2607. doi:10.1175/JPO-D-17-0220.1
156. Väli G. et al. Submesoscale structures related to upwelling events in the Gulf of Finland, Baltic Sea (numerical experiments) // *Journal of Marine Systems*. 2017. V. 171. P. 31–42. DOI: 10.1016/j.jmarsys.2016.06.010.
157. Volkov D.L., Belonenko T.V., Foux V.R. Puzzling over the dynamics of the Lofoten Basin - a sub-Arctic hot spot of ocean variability // *Geophys. Res. Lett.* 2013. V. 40. P. 738–743. doi:10.1002/grl.50126.
158. Volkov D.L., Kubryakov A.A., Lumpkin R. Formation and variability of the Lofoten Basin vortex in a high-resolution ocean model // *Deep Sea Research Part I:*

- Oceanographic Research Papers. 2015. V. 105. P. 142–157.
<https://doi.org/10.1016/j.dsr.2015.09.001>
159. Voropaev S.I., Afanasyev Y.D., Filippov I.A. Horizontal jets and vortex dipoles in a stratified fluid // *Journal of Fluid Mechanics*. 1991. V. 227. P. 543–566.
160. Voropaev S.I., Afanasyev Y.D. Vortex structures in a stratified Fluid. Chapman and Hall. 1994a. 230 pp.
161. Voropaev S.I., Afanasyev Y.D. Symmetric interaction of developing horizontal jet in a stratified fluid with a vertical cylinder // *Physics of Fluids*. 1994b. V. 6. P. 2032–2037.
162. Vortmeyer-Kley R. et al. Comparing Eulerian and Lagrangian eddy census for a tide-less, semi-enclosed basin, the Baltic Sea // *Ocean Dynamics*. 2019, V. 69. P. 701–717. <https://doi.org/10.1007/s10236-019-01269-z>.
163. Xu A. et al. Characteristics of subsurface mesoscale eddies in the northwestern tropical Pacific Ocean from an eddy-resolving model // *Journal of Oceanology and Limnology*. 2020. V. 38. No. 5. P. 1421–1434. <https://doi.org/10.1007/s00343-020-9313-4>
164. Wang B. Theory. P. 335–399. In Lau W.K., Waliser D.E. *Intraseasonal Variability in the Atmosphere-Ocean Climate System* // Berlin; Heidelberg: Springer. 2005. 437 pp. https://doi.org/10.1007/3-540-27250-X_10.
165. Wang R. et al. Impingement of subsurface anticyclonic eddies on the Kuroshio mainstream east of Taiwan // *Journal of Geophysical Research: Oceans*. 2022. V. 127. e2022JC018950. <https://doi.org/10.1029/2022JC018950>
166. White M.A., Heywood K.J. Seasonal and interannual changes in the North Atlantic subpolar gyre from Geosat and TOPEX/POSEIDON altimetry // *Journal of Geophysical Research: Oceans*. 1995. V. 100. I. C12. P. 24931–24941. doi:10.1029/95JC02123
167. Wu C.-R., Hsin Y.-C. The forcing mechanism leading to the Kuroshio intrusion into the South China Sea // *Journal of Geophysical Research*. 2012. V. 117. No. C7. C07015. <https://doi.org/10.1029/2012JC007968>

168. Yasuda I. Hydrographic Structure and Variability in the Kuroshio Oyashio Transition Area // *Journal of Oceanography*. 2003. V. 59. P. 389-402.
169. Yasuda I., Okuda K., Hirai M. Evolution of a Kuroshio warm-core ring—variability of the hydrographic structure // *Deep-Sea Res.* 1992. V. 39. S131–S161.
170. Yu J.-Y. et al. Subsurface ocean temperature indices for Central-Pacific and Eastern-Pacific types of El Niño and La Niña events // *Theoretical Applied Climatology*. 2011. V. 103. P. 337–344. <https://doi.org/10.1007/s00704-010-0307-6>.
171. Yu L.-S. et al. The Lofoten Basin eddy: Three years of evolution as observed by Seagliders // *J. Geophys. Res. Oceans*. 2017. V. 122. P. 6814–6834. DOI: 10.1002/2017JC012982.
172. Zalogin B.S., Kosarev A.N. *Seas* //M.: Mysl', 1999. 400 p. (in Russian).
173. Zhan P. et al. The eddy kinetic energy budget in the Red Sea // *Journal of Geophysical Research: Oceans*. 2016. V. 121. I. 7. P. 4732–4747. doi:10.1002/2015JC011589
174. Zhurbas V. et al. Hindcast of the mesoscale eddy field in the Southeastern Baltic Sea: Model output vs satellite imagery // *Russ. J. Earth. Sci.* 2019. V. 19. ES4006. DOI: 10.2205/2019ES000672.
175. Zhmur V.V. *Mesoscale eddies in the ocean*, Moscow: GEOS, 2010, 290 p. (in Russian).
176. Zhmur V.V., Travkin V.S., Belonenko T.V., Arutyunyan D.A. Transformation of Kinetic and Potential Energy during Elongation of a Mesoscale Vortex // *Physical Oceanography*. 2022, 29(5), P. 449–462. doi:10.22449/1573-160X-2022-5-449-462
177. Zhmur V.V. et al. Changes in the Available Potential and Kinetic Energy of Mesoscale Vortices When They Are Stretched into Filaments // *J. Mar. Sci. Eng.* 2023. V. 11. 1131. <https://doi.org/10.3390/jmse11061131>.
178. Zinchenko V.A., Gordeeva S.M., Sobko Yu.V., Belonenko T.V. Analysis of Mesoscale eddies in the Lofoten Basin based on satellite altimetry // *Fundamental*

and Applied Hydrophysics. 2019, 12(3). P. 46–54.
<https://doi.org/10.7868/S2073667319030067>

179. Zyryanov V.N. Topographic Vortices in the Dynamics of Sea Currents // Moscow: Inst. Vod. Probl. Ross. Akad. Nauk, 1995. 240 p. (in Russian).